Planar Photonic Crystal Nanocavities with Active Quantum Nanostructures

Thesis by

Tomoyuki Yoshie

In Partial Fulfillment of the Requirements

for the Degree of

Doctor of Philosophy

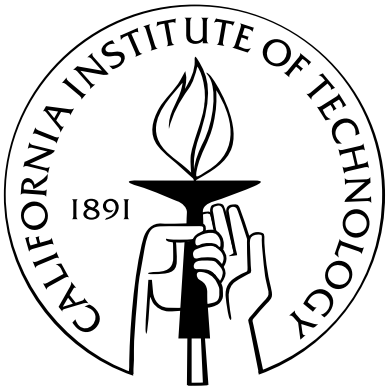

California Institute of Technology

Pasadena, California

2004

(Submitted May 26, 2004)

to Yuka, Akiha, Shigeru, Hiroko

and those who give me freedom to enjoy science.

Acknowledgements

I am very much delighted to have this chance that I can express my gratitude to those who supported and helped me. When I came to Caltech as a visiting associate, it was impossible to imagine that I would come back here again as a graduate student with the support of Professor Axel Scherer. At first, I would like to thank Axel for his help and support. Axel constantly gave me many scientific opportunities with his generous mind. His continuous support enabled me to come back to academic community and finish my Ph.D. I appreciate his efforts of producing unconstrained work environments very much.

I also would like to thank Professor Shigeo Fujita, Kyoto University, for his encouragements. It is sorrowful that I cannot show him this thesis before ending of his life. He was a scientist who taught me, for the first time, how exciting and joyful science is. He helped me to build a foundation stone of my scientific interests. With sincerest sympathy wishing him strength in the days ahead.

It was Sanyo Electric Co. Ltd. and Professor Kenichi Iga, Tokyo Institute of Technology, that gave me a chance to come to Caltech as a visiting associate. I would like to thank Professor Iga, Dr. Akira Ibaraki and Dr. Keiichi Yodoshi for bridging my career between industry and academia. I owe them a debt of gratitude for their generosity and support.

I would like to acknowledge discussions, collaborations and help from Professors Dennis G. Deppe, Hyatt M. Gibbs, H. Jeff Kimble, Hideo Mabuchi, Oskar J. Painter, Demetri Psaltis, Yu-Chong Tai, and Amnon Yariv and Dr.Yueming Qiu. I also appreciate what I have obtained from the photonic crystal community, especially, to Professor Toshihiko Baba, Yokohama National University, and Professor Susumu Noda, Kyoto University.

Dr. Chuan-Cheng Cheng gave me hands-on training on electron beam lithography, dry etching, sputtering and many other machines. The experiences that I had with him are still vivid. He built many types of equipments that I have used for my thesis research. I appreciate his patient teaching and I owe him a debt of gratitude for his contributions to

building equipments.

Professor Jelena Vučković and Dr. Marko Lončar are friends and colleagues through my graduate study at Caltech. I would like to thank them for encouraging me and sharing time. I could find joyous time with them during tough graduate student life.

I am thankful to Kate Finigan, Michelle Vine and Linda Dozsa for organizing administrative work for us and giving us joyful work environments. I also would like to thank all the other members of the Caltech Nanofabrication Group for sharing many things with me, and especially to Dr. Mark Adams, Dr. David Barsic, Dr. Hou-Pu Chou, Dr. Guy DeRose, Raynold Johnson, Terrell Neal, Isamu Niki, Dr. Koichi Okamoto, Dr. Joerg Schilling, Jeremy Witzens, Dr. Joyce Wong, and Zhaoyu Zhang. In addition, I appreciate discussions with group members of Professors Mabuchi, Vahala, and Yariv, and especially John Au, William Green, Tobias Kippenberg, Professor Shayan Mookherjea, and George Paloczi.

Finally, I would like to thank Shigeru Yoshie and Hiroko Yoshie, my parents, and Yuka Yoshie, my wife, for continuous support and unconditional love that they have given to me. In my childhood, my parents encouraged me to enjoy many things. I could develop my mind of unlimited interests to things including science. I couldn't finish this thesis without my wife's support. Yuka always gives me joyful home environments and expands my interests that I had not experienced. I would like to dedicate this thesis to them.

Abstract

Extreme photon localization is applicable to constructing building blocks in photonic systems and quantum information systems. A finding fact that photon localization in small space modifies the radiation process was reported in 1944 by Purcell, and advances in fabrication technology enable such structures to be constructed at optical frequencies. Many demands of building compact photonic systems and quantum information systems have enhanced activities in this field. The photonic crystal cavity has potential in providing a cavity that supports only the fundamental mode $\sim (\lambda/2n)^3$ together with good confinement of light within a resonator. This thesis addresses experimental and theoretical aspects of building such photon localization blocks embedding active quantum nanostructures in a planar photonic crystal platform. Examples given in this thesis are (1) quantum dot photonic crystal nanolasers, (2) high-speed photonic crystal nanolasers, and (3) light-matter coupling in a single quantum dot photonic crystal cavity system.

(1) A combination of quantum dots and photonic crystal nanocavities provides chirpless high-speed nanolasers. Room temperature low-threshold lasing action was demonstrated from a coupled cavity design ($0.7 \sim 1.2(\lambda/n)^3$) embedding InAs/GaAs self-assembled quantum dots. The nanolasers showed small (absorbed) pumping power threshold as sub-20 μW and high spontaneous coupling factors$\sim$0.1. Single quantum dot lasing is likely to occur both by proper alignment of the single quantum dot relative to geometries of photonic crystals and by a narrow QD emission line in the high-Q localized mode.

(2) Enhancement of radiation process in a small cavity was used to demonstrate high frequency relaxation oscillation up to 130 GHz. Built-in quantum well saturable absorbers enable us to probe the relaxation oscillation of such small lasers.

(3) Onset of intermediate light-matter coupling was demonstrated in a single quantum dot photonic crystal cavity system. A tripling in Q/V (quality factor divided by mode volume) is found to enable photons to start a strong interaction with a single quantum dot.

Contents

List of Figures

List of Tables

Chapter 1

Fundamentals of Photon Localization

Light is understood in both forms of electromagnetic waves and photon particles as Bosons. This important view of duality was introduced as a hypothesis by Einstein after Planck explained experimental spectra data of black body radiation by quantization of harmonic oscillator energy. Quantum theory of light or quantum electrodynamics theory [8, 16] has been developed as one of the main topics of quantum mechanics. Quantum treatment of light helped us understand the nature of light and create novel devices such as transistors and lasers (light amplification by stimulated emission of radiation). Laser light [75] is considered as being at a boundary of classical and quantum world in a sense that laser light has fluctuations given by

$$\sqrt{\langle \Delta x^2 \rangle}\sqrt{\langle \Delta p^2 \rangle} = \frac{\hbar}{2} \tag{1.1}$$

Pushing this limit or examining each photon gives us a glimpse of the unusual world described by quantum mechanics. This extreme manipulation of photons has been realized with the help of advanced fabrication technology. The invention of lasers opened up possibilities of using light as reliable signal source. The coherent light, which can use time and frequency spaces efficiently, is essential for modern communication systems.

1.1 Overview of This Thesis

This section is written to give readers simple description of each chapter of this thesis. A goal of this thesis is to show extreme photon localization as functional devices, and to find out fundamental limits of photon localization. More specifically, feasibilities of high-speed and low-threshold nanolasers and possibilities of strong photon-light matter coupling in a

quantum dot photonic crystal cavity system are shown. Each chapter describes important characters of photonic crystal nanocavity.

Chapter 1: Fundamentals of Photon Localization This chapter overviews fundamental topics of photon localization such as photonic crystals, microcavities, and light-matter coupling.

Chapter 2: Localized Modes in a Photonic Crystal Cavity In this chapter, designs, fabrication processes, and characterization of simple photonic crystal cavity systems are described. The topics are intermixing of TE and TM modes, improvements of cavity designs, and light-matter coupling.

Chapter 3: Quantum Dot Photonic Crystal Nanolasers Using designs of photonic crystal nanocavities and advanced fabrication techniques, lasing action from quantum dot photonic crystal nanocavities, and possibilities of single quantum dot lasers are shown.

Chapter 4: High-Speed Photonic Crystal Nanolasers Large modification of radiation rate has been demonstrated in our quantum well photonic crystal nanocavities by probing high frequency relaxation oscillation.

1.2 Photonic Crystals

Photonic crystals (PC) [96, 36] are structures, which have periodic permittivity (ϵ) and/or permeability (μ) in an order of electromagnetic wavelength. The periodicity is described with a primitive vector $\overrightarrow{G}$ as

$$\epsilon(\overrightarrow{r}) = \epsilon(\overrightarrow{r} + \overrightarrow{G}) \tag{1.2}$$

$$\mu(\overrightarrow{r}) = \mu(\overrightarrow{r} + \overrightarrow{G}) \tag{1.3}$$

When having only permittivity periodicity for simplicity, photonic crystals satisfy wave equations [73] given by

$$\frac{1}{\epsilon(\overrightarrow{r})}\nabla\times\{\nabla\times\overrightarrow{E}(\overrightarrow{r},t)\} = -\frac{1}{c^2}\frac{\partial^2}{\partial t^2}E(\overrightarrow{r},t) \quad (1.4)$$

$$\nabla\times\{\frac{1}{\epsilon(\overrightarrow{r})}\nabla\times\overrightarrow{H}(\overrightarrow{r},t)\} = -\frac{1}{c^2}\frac{\partial^2}{\partial t^2}\overrightarrow{H}(\overrightarrow{r},t) \quad (1.5)$$

Using monochromatic waves ($E(\overrightarrow{r},t) = E(\overrightarrow{r})e^{-i\omega t}$, $H(\overrightarrow{r},t) = H(\overrightarrow{r})e^{-i\omega t}$) as the solutions [64],

$$\frac{1}{\epsilon(\overrightarrow{r})}\nabla\times\{\nabla\times\overrightarrow{E}(t)\} = -\frac{\omega^2}{c^2}E(t) \quad (1.6)$$

$$\nabla\times\{\frac{1}{\epsilon(\overrightarrow{r})}\nabla\times\overrightarrow{H}(t)\} = -\frac{\omega^2}{c^2}\overrightarrow{H}(t) \quad (1.7)$$

are obtained. Next, we apply Bloch's theorem to the above equations and Fourier-transform periodic functions $u(\overrightarrow{r})$, and one obtains

$$E(\overrightarrow{r}) = E_{\overrightarrow{k}\,n}(\overrightarrow{r}) = u_{\overrightarrow{k}\,n}(\overrightarrow{r})e^{i\overrightarrow{k}\cdot\overrightarrow{r}} = \sum_{\overrightarrow{G}} E_{\overrightarrow{k}\,n}(\overrightarrow{G})e^{i(\overrightarrow{k}+\overrightarrow{G})\cdot\overrightarrow{r}} \quad (1.8)$$

$$H(\overrightarrow{r}) = H_{\overrightarrow{k}\,n}(\overrightarrow{r}) = u_{\overrightarrow{k}\,n}(\overrightarrow{r})e^{i\overrightarrow{k}\cdot\overrightarrow{r}} = \sum_{\overrightarrow{G}} H_{\overrightarrow{k}\,n}(\overrightarrow{G})e^{i(\overrightarrow{k}+\overrightarrow{G})\cdot\overrightarrow{r}} \quad (1.9)$$

Putting the Fourier-transformed electric and magnetic fields in the wave equations, one obtains

$$-\sum_{\overrightarrow{G}'}\kappa(\overrightarrow{G}-\overrightarrow{G}')(\overrightarrow{k}+\overrightarrow{G}')\times[(\overrightarrow{k}+\overrightarrow{G}')\times\overrightarrow{E}_{\overrightarrow{k}\,n}(\overrightarrow{G}')] = \frac{\omega^2_{\overrightarrow{k}\,n}}{c^2}\overrightarrow{E}_{\overrightarrow{k}\,n}(\overrightarrow{G}) \quad (1.10)$$

$$-\sum_{\overrightarrow{G}'}\kappa(\overrightarrow{G}-\overrightarrow{G}')(\overrightarrow{k}+\overrightarrow{G})\times[(\overrightarrow{k}+\overrightarrow{G}')\times\overrightarrow{H}_{\overrightarrow{k}\,n}(\overrightarrow{G}')] = \frac{\omega^2_{\overrightarrow{k}\,n}}{c^2}\overrightarrow{H}_{\overrightarrow{k}\,n}(\overrightarrow{G}) \quad (1.11)$$

where

$$\frac{1}{\epsilon(\overrightarrow{r})} = \sum_{\overrightarrow{G}}\kappa(\overrightarrow{G})e^{i\overrightarrow{G}\cdot\overrightarrow{r}} \quad (1.12)$$

These two eigenvalue problems for $\overrightarrow{E}_{\overrightarrow{k}\,n}(\overrightarrow{G})$ and $\overrightarrow{H}_{\overrightarrow{k}\,n}(\overrightarrow{G})$ give photonic bands as the solutions, and $\overrightarrow{H}_{\overrightarrow{k}\,n}(\overrightarrow{G})$ are used to construct orthogonal basis because the operator for the

eigenvalue problem on Equation 1.11 is Hermitian. A complete photonic bandgap is defined as the energy range $\hbar\omega$ where there are no allowed propagation states over all $\overrightarrow{k}$. One can obtain orthogonality condition described by

$$\int_V \overrightarrow{H}_{\overrightarrow{k}\,n}(\overrightarrow{r}) \cdot \overrightarrow{H}_{\overrightarrow{k}\,n}(\overrightarrow{r}) \;=\; V\delta_{\overrightarrow{k}\,\overrightarrow{k}'}\delta_{nn'} \tag{1.13}$$

The derived eigenvalue equation for $\overrightarrow{H}_{\overrightarrow{k}\,n}(\overrightarrow{G})$ is a basic formula for plane-wave expansion method to find photonic band(gap)s.

Using the plane-wave expansion technique, photonic bands are calculated. Photonic bands, which are calculated by 121 plane-waves $\overrightarrow{H}_{\overrightarrow{k}}$ on two complimentary structures with triangular lattice alignments of five different r/a's are shown in Figures 1.1 and 1.2. The complimentary structures consist of air cylinders in dielectric (Figure 1.1) and dielectric cylinders in air (Figure 1.2), respectively. For structures with air cylinders in dielectric, you find a large forbidden gap between the 1st and the 2nd lowest bands in TE modes whereas in TM modes an overlapping of the 1st and the 2nd lowest band states in energy axis. On the other hand, for triangular lattices made by dielectric cylinders in air, TM modes have a large forbidden gap between the 1st and the 2nd lowest bands. The forbidden gap energy positions are lowered or lifted as r/a increases for dielectric or air cylinder structures, respectively. This results from changes in mode overlap with air and dielectric. These photonic bands can be used as basis in order to construct cavity modes made in the host photonic crystal lattices.

Figure 1.3 (b)–(e) are real space band profiles for two-dimensional square lattice slab. The profiles show amplitude of the B_z components in the middle slice of slab. The band in (b) has antinodes in dielectrics whereas the bands in (c), (d) and (e) have antinodes in air. Therefore, the band in (b) is called a dielectric band. The bands in (c)–(e) are called air bands [95].

1.3 Optical Microcavities

An optical microcavity [14, 98, 90] is a structure for confining optical waves, and is useful for miniaturizing functional photonic devices. Lasers require feedback of optical waves and gain media, and an optical cavity is responsible for providing that feedback of electromagnetic

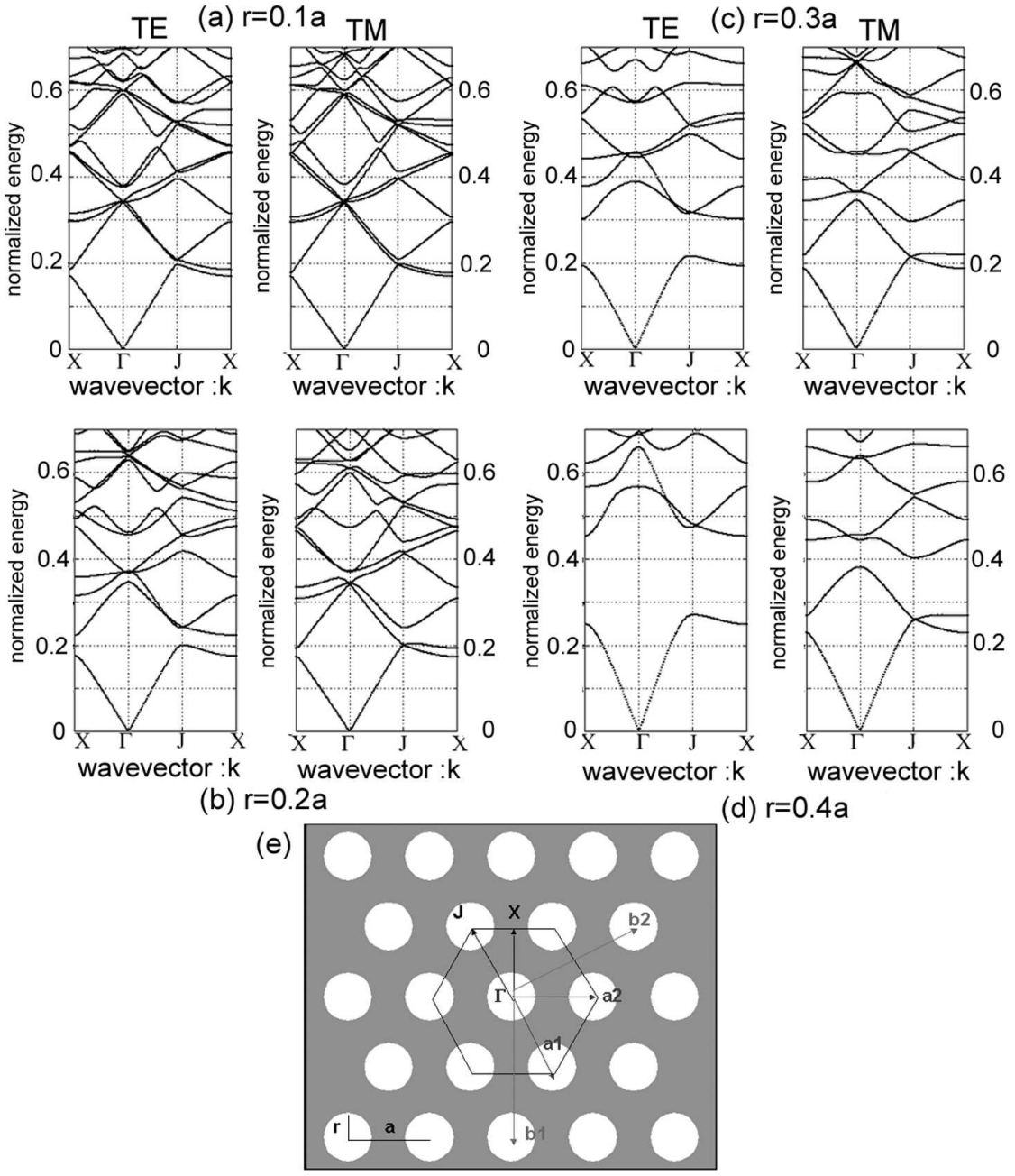

Figure 1.1: Photonic bands obtained by 2D plane-wave expansion method with 121 plane-waves. The photonic crystals consist of two-dimensional triangular lattices. The dielectric constants are 1.0 and 12 for air and dielectric. Circular areas in panel (e) have smaller dielectric constant. TM and TE modes have nonzero H and E fields in cylinder axis direction, respectively.

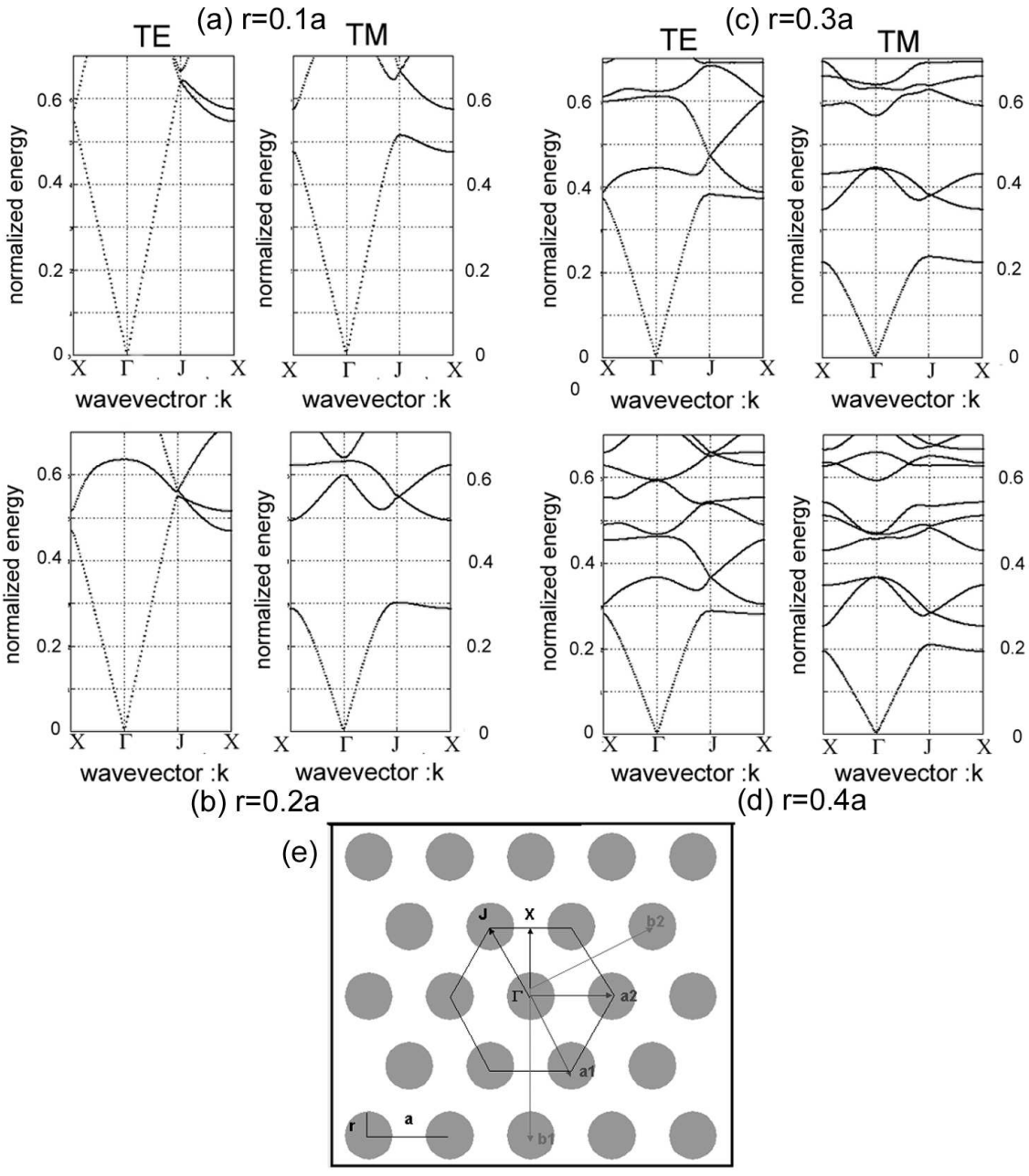

Figure 1.2: Photonic bands obtained by 2D plane-wave expansion method with 121 plane-waves. The photonic crystals consist of two-dimensional triangular lattices. The dielectric constants are 1.0 and 12 for air and dielectric. Circular areas in panel (e) have bigger dielectric constant. TM and TE modes have nonzero H and E fields in cylinder axis direction, respectively.

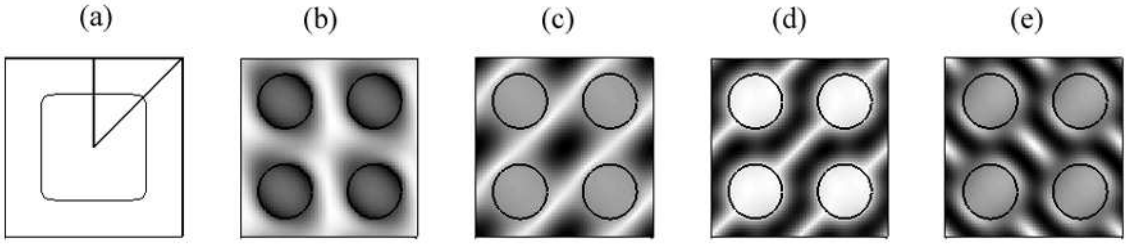

Figure 1.3: Photonic bands in real space for square lattice rod alignment. (a) shows a mode propagation direction. (b),(c),(d), and (e) show mode profiles for the 1st, 2nd, 3rd, and 4th lowest modes, respectively. Courtesy of Jeremy Witzens.

radiation. For example, edge-emitting laser diodes are equipped with Fabry-Perot Etalons to provide feedback, and gain media such as quantum wells are embedded in the optical path. When one builds such lasers, the microcavity has an identical function with a large cavity. However, a microcavity is fundamentally different as it can modify the radiation dynamics of an oscillator at resonance in the cavity. When one limits the volume in which the electromagnetic waves can exist, the emission rates can be influenced.

The quality factor (Q) is useful for measuring confinement of light by cavities with different geometric shapes. Let us consider a resonator, which contains a monochromatic oscillator at $\omega = \omega_0$ and escaping radiation rate of $1/(2\tau)$ [31]. The rate equation for field U can be derived in a form of a differential equation given by

$$\frac{dU}{dt} = -\left(i\omega_0 + \frac{1}{2\tau}\right) U \tag{1.14}$$

Therefore, the energy change is described by

$$\frac{d(UU^*)}{dt} = \frac{d|U|^2}{dt} = -\frac{1}{\tau}|U|^2 \tag{1.15}$$

Using the definition of Q factor, one obtains

$$Q = \omega \frac{|U|^2}{-d|U|^2/dt} = \omega\tau \tag{1.16}$$

Let us next consider two resonators with energy exchange between them. The rate

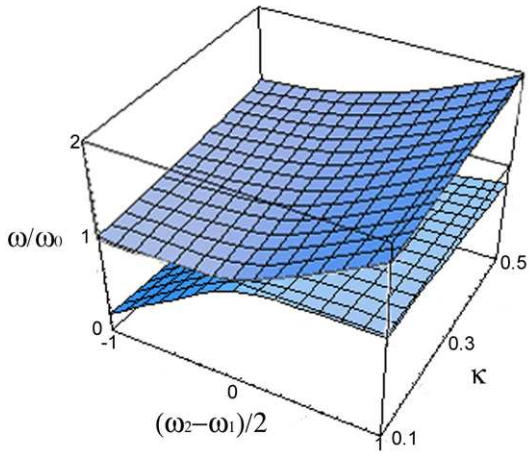

Figure 1.4: Anti-crossing of mode frequencies in two-coupled cavities. $\omega_0 = (\omega_1 + \omega_2)/2$

equations are given by

$$\frac{dU_1}{dt} = -i\omega_1 U_1 + \kappa_{12} U_2 \tag{1.17}$$

$$\frac{dU_2}{dt} = -i\omega_2 U_2 + \kappa_{21} U_1 \tag{1.18}$$

Assuming $U_{1,2}(t) = \widetilde{U}_{1,2} e^{-i\omega t}$ and $\kappa = \kappa_{12} = -\kappa_{21}^*$, one obtains

$$\omega = \frac{\omega_1 + \omega_2}{2} \pm \sqrt{\left(\frac{\omega_1 - \omega_2}{2}\right)^2 + |\kappa|^2} \tag{1.19}$$

Therefore, there are two solutions at zero detuning ($\omega_1 = \omega_2$) and these do not cross each other as a function of ω. Such splitting will be described in Chapter 3 where coupled cavity designs are discussed, and is seen in Figure 1.4.

1.3.1 Linewidth and mode volume of an optical resonator

In the extreme limit, nature does not permit a simultaneous decrease in both the emission linewidth in a resonator (increased Q factor) and in the mode volume. This can be seen from Equation 1.1 by using *de Broglie*'s wavelength. Taking only one-dimensional space,

one obtains

$$\Delta x \Delta(\frac{2\pi n}{\lambda_e}) \geq \frac{1}{2} \tag{1.20}$$

$$\Delta x \Delta\lambda_e \geq \frac{\lambda_e^2}{4\pi n} \tag{1.21}$$

where

$$(\Delta x)^2 = \int_{-\infty}^{\infty} dr[\langle\psi|r^2|\psi\rangle - \langle\psi|r|\psi\rangle^2] \tag{1.22}$$

One can assume that an oscillator with linewidth $\Delta\lambda_e$ at wavelength λ_e is placed into a one-dimensional optical cavity for simplicity. The Q_e value is defined as $\lambda_e/\Delta\lambda_e$. It is noted that Q_e is not the same as the cold cavity Q factor, but these two values are correlated when an oscillator radiates within a small cavity. Heisenberg's uncertainty relation then gives the following inequality relation

$$\Delta x \geq \frac{\lambda_e Q_e}{4\pi n} \tag{1.23}$$

Therefore, sharp emission lines inherently tend to have difficulty in confining light within small volumes, and $Q_e/\Delta x$ values have upper limits. This is the fundamental limit of photon localization, and radiation at resonance has a lower limit of the volume (Δx in 1D) confined by a cavity.

Using quantum theory [31], one can derive the mean square fluctuations of radiation emitted from an optical resonator. b and $b^\dagger$ are annihilation and creation operators. $b^{(1)} = \frac{b+b^\dagger}{2} \propto q$ and $b^{(2)} = \frac{b-b^\dagger}{2} \propto p$ where p and q are position and momentum operators. $b^{(1)}$ and $b^{(2)}$ are then normalized position and momentum operators.

$$\langle|b^{(1)}(\omega)|^2\rangle = \langle|b^{(2)}(\omega)|^2\rangle = \frac{1}{4}\left[1 + \frac{8/(\tau_e\tau_g)}{(\omega-\omega_0)^2 + (1/\tau_0 - 1/\tau_g + 1/\tau_e)^2}\right] \tag{1.24}$$

where $1/\tau_0$. $1/\tau_e$, $1/\tau_g$ are decay rate of the noise, the cavity damping rate, the growth rate from gain. In a resonator without any gain ($1/\tau_g = 0$), these fluctuations are zero point fluctuations. On the other hand, in a resonator with gain, such fluctuations are enhanced at the resonance and the photon flow rate is also enhanced around the resonance for optical

Cavity Type	Active or Passive	Q factor	V_{mode} $[\times(\lambda/n)^3]$	Q/V_{mode} $[\times(n/\lambda)^3]$	References
Photonic Crystal	Passive	35,000	1	3.5×10^4	[1]
–	Active(QD)	2,800	0.43	6.5×10^3	this thesis [107]
Microdisk	Active(QD)	12,000	6	2×10^3	[44]
Micropost	Active(QD)	2,000	5	4×10^2	[25]
Microsphere	Passive	8×10^9	∼260	$\sim 3 \times 10^7$	[80]

Table 1.1: Comparison table of typical microcavities. The Q factors are experimentally obtained, and the mode volume are theoretically obtained.

cavity with gain.

1.3.2 Typical microcavity designs

Total internal reflection and Bragg reflection are useful tools when constructing geometries for efficient confinement of light in small volumes. Microdisks [44], micro-spheres [80] and planar photonic crystals [59] all use total internal reflection, and micropillars [35, 76, 25] as well as photonic crystals benefit from Bragg mirrors. Table 1.1 compares Q factors, V_{mode}, and Q/V_{mode} among typical small cavities. The Q/V_{mode} values are often used as figures of merit for cavity QED. The higher the value of Q/V_{mode}, the stronger the coupling. In this thesis, the highest quality factors in active photonic crystal cavities [107] are shown in Chapter 2. Whispering gallery modes, defined in relatively large passive structures (Microsphere), produce very high Q factors, and thus the figures of merit of cavity QED are higher than the other cavity designs. However, at present, the inclusion of active material such as quantum dots is still difficult. Instead, planar photonic crystal cavity designs easily incorporate stable active material by the process of crystal growth and provide the smallest optical cavities as useful functional devices.

1.4 Microcavity Lasers

The radiation process within a microcavity provides an experimental system rich in physics. Purcell's prediction [65] can be observed in many state of the art microcavities. The so-called microcavity effect requires a modification of the radiation process or low-Q cavity QED effect. Figure 1.6 (b) shows a typical temporal evolution of self-assembled InAs QD

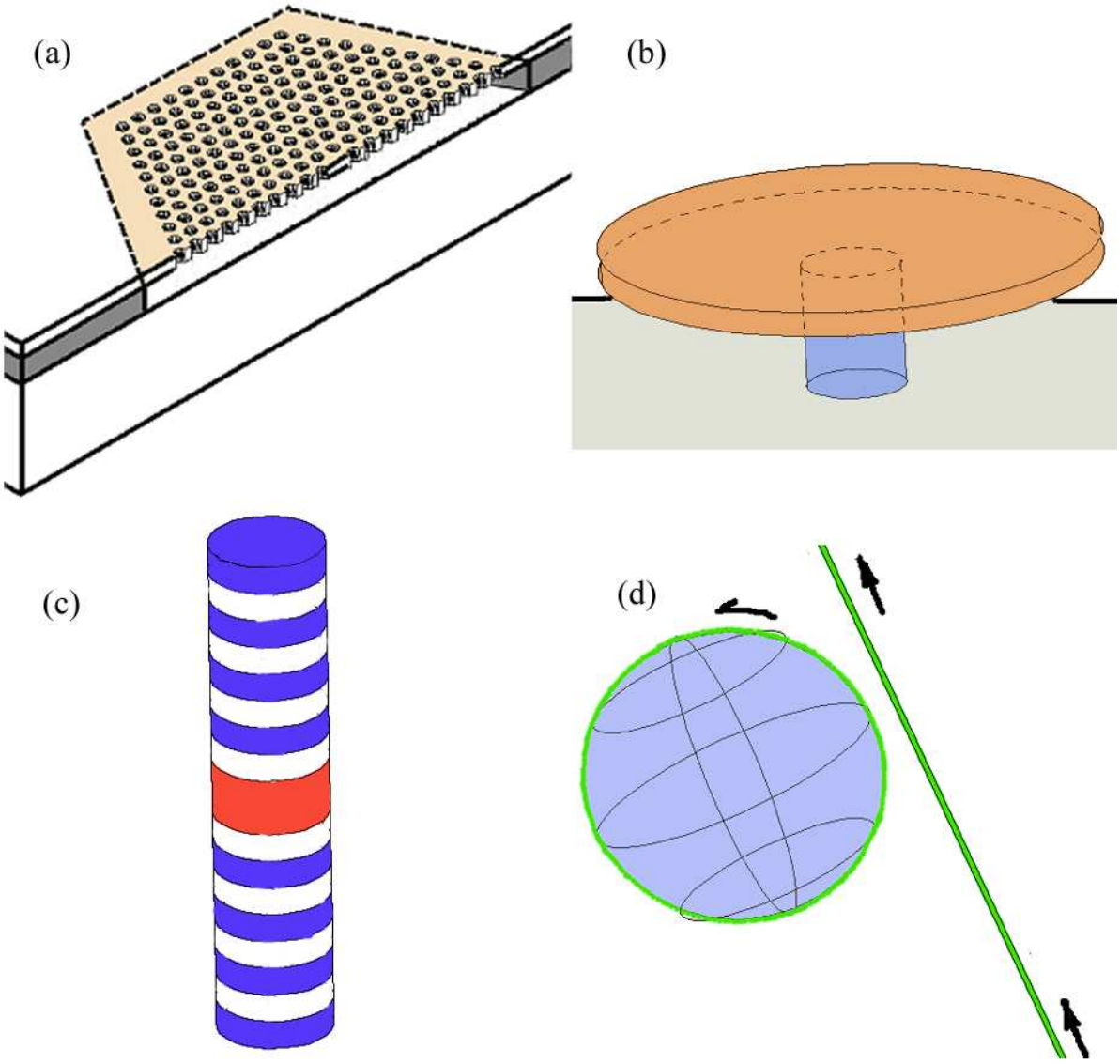

Figure 1.5: Typical microcavity structures. (a) photonic crystal cavity, (b) microdisk cavity, (c) DBR micropost cavity, and (d) silica microsphere cavity.

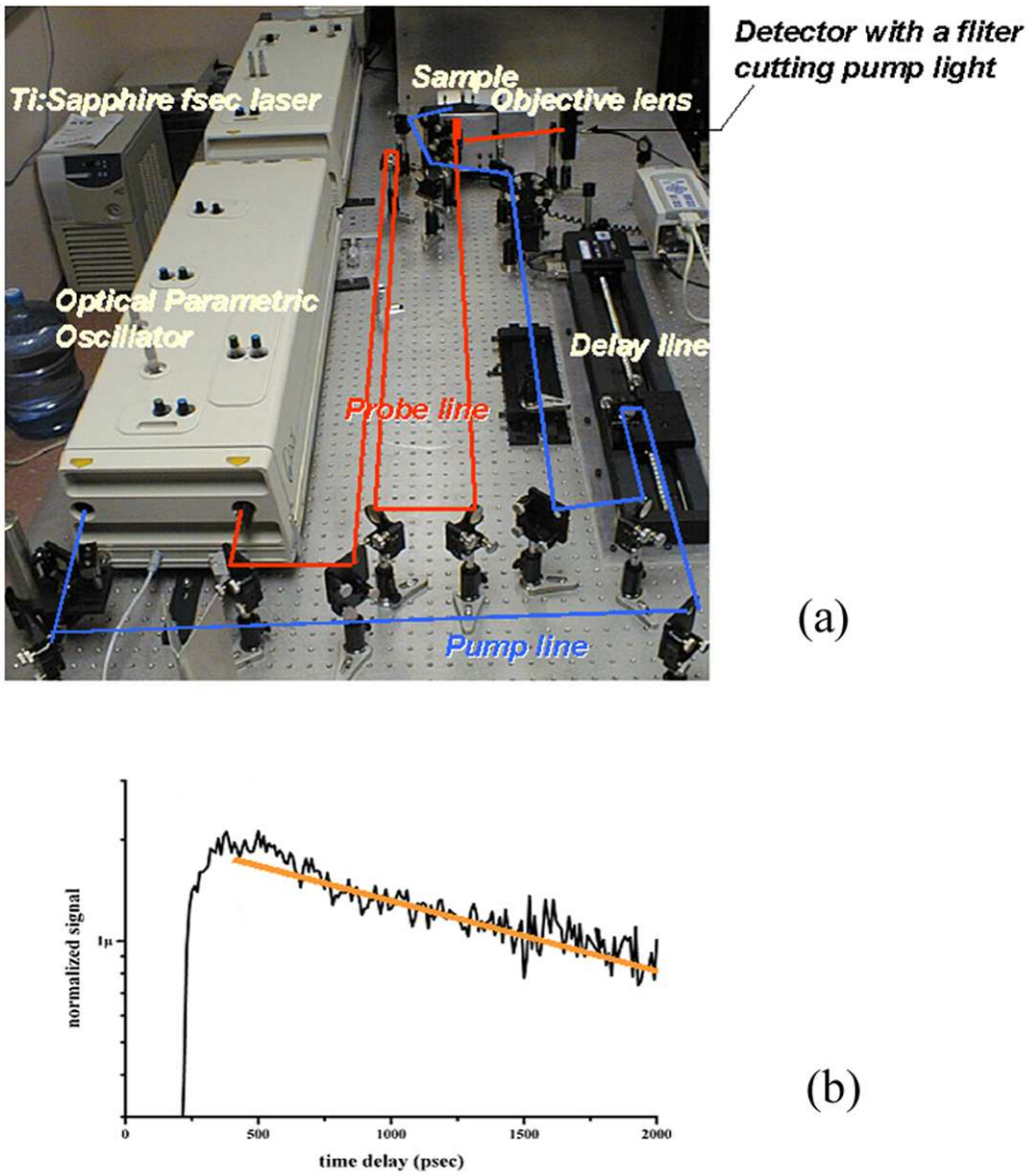

Figure 1.6: A panel (a) shows lifetime measurement system of two color pump-probe spectroscopy. A panel (b) shows temporal evolution of QD carrier occupied in upper level, which was measured by the pump-probe spectroscopy. The QD oscillators are located in free space.

emission in free space, which is measured by two-color pump probe spectroscopy. The radiation rate is enhanced when emitted photons are located at resonance. This can be described within the framework of weak light-matter coupling or Purcell's effect [24]:

$$\Gamma_{cav} = \frac{3Q(\lambda/n)^3}{4\pi^2 V_{mode}} \frac{|d \cdot f|^2}{|d \cdot f'|^2} \Gamma_{free} \tag{1.25}$$

where Γ_{cav},Γ_{free},f, f' and d are the radiation rates in the cavity and free space, the electric field at the emitter in a cavity and in free space, and the dipole moment of the emitter, respectively. Thus it can be seen that photons are emitted more frequently within a cavity than in free space. On the other hand, when photons find good mirrors at off-resonance, the radiation rate Γ is inhibited due to the negligible density of states $\rho(E)$. This inhibition of radiation can be understood by Fermi's golden rule when using time-dependent perturbation theory [50]:

$$\Gamma(\omega) = \frac{2\pi}{\hbar} \rho_f(E_s) |\langle k|V|s\rangle|^2 \tag{1.26}$$

This is true when a small perturbation V is constant or varies harmonically in time. The radiation rate is proportional to the density of states, and Fermi's golden rule tells us that the radiation decays exponentially.

The modification of optical processes is one of the distinct characteristics of microcavities. High spontaneous emission coupling [102, 99, 7, 93] is another benefit of such microcavities. The mode separation in a cavity increases as the size of cavity is decreased, and when the cavity size is comparable to the wavelength, the number of modes in the radiation range approaches one. When this number is only one in the radiation spectrum, a light-emitting cavity operates as a single-mode emitter. This way, undesirable coupling to non-lasing modes can be suppressed and lasers tend to lose the threshold kink in their LL curves. For conventional edge-emitting lasers, the spontaneous emission coupling (β) factors are around 10^{-4} to 10^{-5}. At the same time, because the threshold is inversely proportional to the β factor, the threshold value decreases. Thus, high β factors, high-Q factors and low non-radiative recombination are key to constructing zero-threshold lasers. Photonic crystal cavities should exhibit both high β and Q factors, but non-radiative recombination should still be seriously considered.

1.5 Light-Matter Coupling

Cavity quantum electrodynamics (QED) [8, 16, 47] provides an essential approach to understanding the physics of radiation in a cavity. Light-matter coupling is a major topic of cavity QED, and atoms are often used to obtain strong light-matter coupling and for examining it. Instead of using free atoms, in this thesis, quantum dots (sometimes called artificial atoms) are used to show such coupling with the intense cavity fields obtained by planar photonic crystal resonators.

To clarify the effects of the interaction between atoms and cavity fields, basic formulas are shown here. For simplicity, we consider a two-level atom in a quantized field. The total Hamiltonian of the coupled system is obtained to show a dressed state view or Jaynes-Cummings model [8] as

$$H = \hbar\omega a^{+}a + \frac{1}{2}\hbar\omega_{\sigma}\sigma + \hbar(a + a^{+})(g\sigma_{+} + g^{*}\sigma_{-}) \tag{1.27}$$

where a^{+}, a, σ_{+}, $\sigma_{-}$and $\frac{1}{2}\hbar\omega_{\sigma}\sigma$ are creation operator of photon, annihilation operator of photon, creation operator of atom, annihilation operator of atom, and the unperturbed Hamiltonian of the two level emitter. With a rotating wave approximation, one can neglect two terms $a\sigma_{-}$ and $a^{+}\sigma_{+}$, and one obtains

$$H = \hbar\omega a^{+}a + \frac{1}{2}\hbar\omega_{\sigma}\sigma + \hbar(ga\sigma_{+} + g^{*}a^{+}\sigma_{-}) \tag{1.28}$$

$a\sigma_{+}$ is the operator to excite one atom and annihilate one photon (one photon absorption) whereas $a^{+}\sigma_{-}$ is one to de-excite one atom and create one photon (one photon emission).

When the coupling is weak, as described in the previous section, the optical process can be understood by weak light-matter coupling. However, strong coupling of light with matter allows a reversible process between radiation and absorption. The eigen-states of the Jaynes-Cummings Hamiltonian form a ladder of pairs of entangled states $|e, n\rangle \pm |g, n+1\rangle$ as well as nondegenerate ground states $|g, 0\rangle$. Values n are photon numbers and non-negative integers. $|s, m\rangle$ is an entangled state with m photons and carrier with a state s (s is excited (e) or ground (g)). The pair of entangled states is separated by $2\hbar\Omega\sqrt{n+1}$ where $\Omega = \frac{E_0}{\hbar}\overrightarrow{d}\cdot\overrightarrow{f}$ is the Rabi frequency. The electric field of the modes is $E = E_0[a\overrightarrow{f}^{*} + a^{\dagger}\overrightarrow{f}]$, $E_0 = \sqrt{\frac{\hbar\omega}{2\epsilon_0 V}}$ is the field per photon, and the effective mode volume is $V = \int |\overrightarrow{f}(r)|^2 d^3r$.

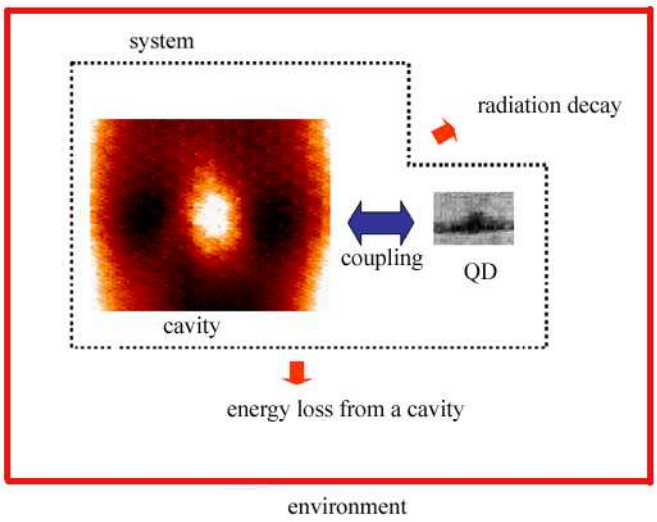

Figure 1.7: Coupled cavity-quantum dot system. The radiation from a quantum dot is coupled with the cavity mode.

This splitting of eigen-states is a signature of strong light-matter coupling, and an origin of Mollow's triplet in resonance fluorescence. In fact, state of the art microcavities have the potential to observe strong light-single quantum dot coupling, as shown in figure 1.8, including our planar photonic crystal cavities. For solid-state microcavities with single quantum dots [39] shown in Figure 1.7, strong light-matter coupling is essential to build indistinguishable single photon sources.

1.6 Photonic Crystal Nanocavity Designs

One can find many photonic crystal cavity designs in the literature [1, 48, 49, 61, 68, 82, 70, 91]. Here we focus on planar photonic crystals, which have translational symmetry in refractive index. There are different symmetric structures such as rotational symmetry structures (photonic quasicrystals [108]) and photonic crystals with periodicity in permeability μ. An example of a quasicrystal structures is shown in Figure 1.9 (a).

There are only three geometries, which can be filled with identical 2D tiles without any space or overlap between them. They are triangles, squares and hexagons. Their popularity as photonic crystals goes the same as this order. Photonic bandgaps decrease in this order, and larger bandgaps help photons to localize in small spaces. However, in two-

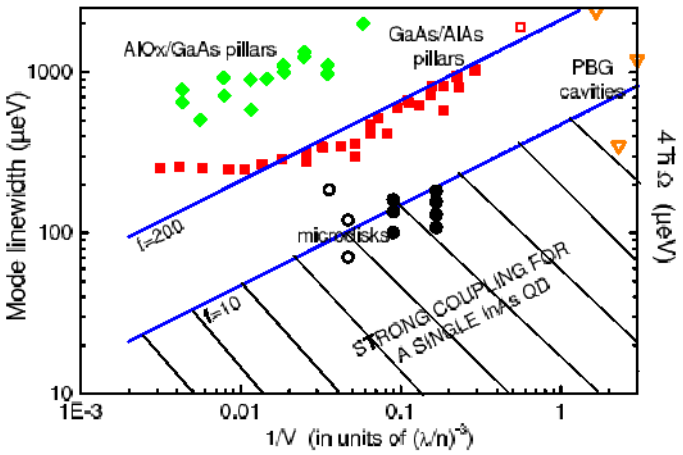

Figure 1.8: (After Jean-Michel Gérard [24].) This figure shows the mode linewidth of some microcavities as a function of an inverse of mode volume. The lowest open triangle is our cavity shown in Chapter 2.

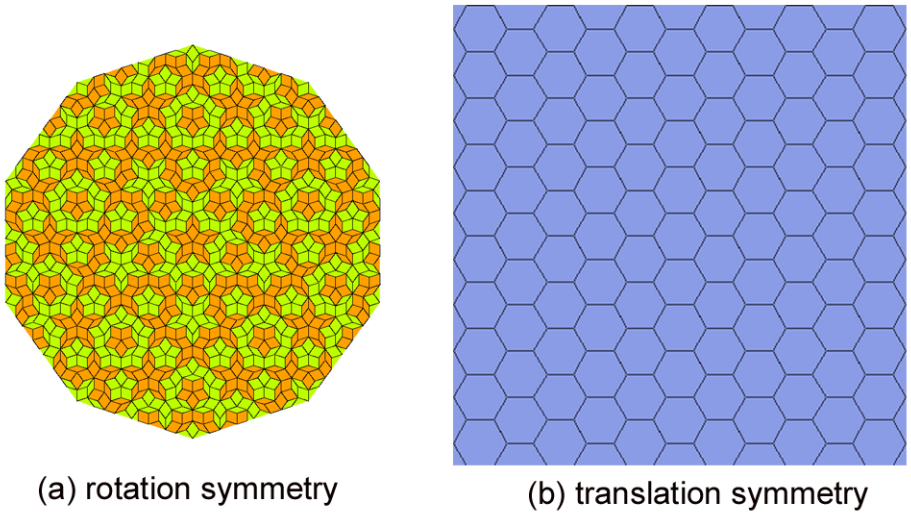

Figure 1.9: Panels (a) and (b) have rotational symmetry and translation symmetry. When one ignores the colors in panel (a), the structure has 10-fold rotation symmetry whereas one needs a horizontal mirror reflection with the colors. Panel (b) has a C_{6v} symmetry as point group and translational symmetry.

dimensional photonic crystals, large bandgap photonic crystals are not always suitable for good confinement of light. The reason is that the optical modes are three-dimensional, and planar photonic crystals rely on vertical confinement of light only through total internal reflection. In this thesis, we consider only slab structures, which have two-dimensional translational symmetry in refractive index.

Some disorder in periodicity can induce additional modes of electromagnetic waves. A mode is useful when the mode frequency is in the bandgap or at the band edges. When located at band edges [73], the group velocity v_g slows down due to the small slope in the dispersion curve. This slowing of light is beneficial for increasing the length of interaction between light and matter. For example, by using band edge modes, one can easily construct broad-area laser diodes. On the other hand, when located in the bandgap, the mode behaves such that periodic structures surrounding the disorder act as mirrors. This is the exact method used to construct photonic crystal cavities shown in this thesis. Readers shall see several designs for building photonic crystal devices in this thesis to control mode volumes, Q factors, and electric field profiles, depending on requirements of each device. In order to design small mode volumes, the number of mode nodes should be small. Therefore, typical planar photonic crystal cavity modes are monopoles [63], dipoles [61], or quadrapoles [68].

1.7 Conclusions

In this chapter, characteristics and methods of photon localization are presented. Photon localization is a fundamental topic in electromagnetic engineering and optics, and is essential in building functional devices in future nano-photonics and quantum information systems. A photonic crystal cavity is one such type of microcavity, offering novel characters as optical sources such as thresholdless lasing, high spontaneous emission coupling, and modified spontaneous emission.

Chapter 2

Localized Modes in a Planar Photonic Crystal

2.1 Introduction

As described in the preceding chapter, compact and high-quality cavities are essential building blocks in constructing nano-photonic systems and quantum information systems. It is important in understanding the performances of localized modes produced by disorder in two-dimensional photonic crystals. In this chapter, we first show the fundamental processes to fabricate high quality photonic crystals. These processes allow the transfer of our designs into semiconductor material. Designs, fabrication techniques, and characterization of two kinds of photonic crystal cavities are then described. These two-dimensional structures differ in symmetry by a σ_v operation. One design has a broken symmetry in the vertical (z-) direction with respect to the slab due to the presence of the substrate under the photonic crystal slab, whereas the other design has symmetry in the z-direction as the slab is surrounded by air on both top and bottom. Finally, modification of radiation processes is described by tuning the emission from a single quantum dot relative to a cavity resonance peak at low temperatures.

2.2 Fabrication Basics of Two-Dimensional Photonic Crystal Cavity

Key fabrication steps for our two-dimensional photonic crystals consist of lithography and dry etching. Precise patterning and anisotropic etching are essential to transfer our designs

System	Electron Gun	V_{acc}	Beam Spot	Current
1) Hitachi S-4500	Cold Field Emission	30 kV	1 nm	50 pA
2) Leica EBPG 5000	Thermal Field Emission	100 kV	30 nm	1 nA

Table 2.1: Electron beam systems used in this thesis. V_{acc} is acceleration voltage.

into dielectric materials, such as InGaAs or GaAs. In this section, we show details of electron beam lithography and pattern transfer using three dry-etching methods, i.e., reactive ion etching (RIE), inductively coupled plasma reactive ion etching (ICP-RIE), and chemically assisted ion beam etching (CAIBE).

2.2.1 Electron beam lithography

Lithography describes the first step in fabricating planar photonic crystals, and the process of transferring geometric shapes from a mask into the surface of the material of interest. Sub-micron scale designs of photonic crystals require a resolution of a few tens nanometers in lithography and pattern transfer. Typical lithographic methods for satisfying such stringent requirement are limited to electron beam (EB) lithography and industrial photolithography, such as photolithographic steppers using KrF and ArF light sources. In this thesis work, two electron beam lithography systems have been used to define patterns onto the substrate. The important features of our EB lithography systems are summarized in Table 2.1. The Hitachi system has superior resolution featuring a spot size of below 1 nm whereas the Leica system has fast and reliable electron beam writing performance with accurate specimen alignment on large wafers up to six inches in diameter.

A cold-field emission source, as used in the Hitachi system, provides a narrower energy distribution, resulting in smaller focused electron spot sizes than a thermal field emission source, as used in the commercial Leica system. On the other hand, a thermal field emission source has better current stability over time. The beam current fluctuations are typically less than 0.1% and 3% for thermal-field emitters and cold-field emission sources, respectively. Each of these system features adequate writing resolution to fabricate our planar photonic crystal structures. Samples in this chapter as well as the quantum dot photonic crystal lasers in the next chapter are typically fabricated by the Hitachi system, and the Leica system was used for both high-speed photonic crystal lasers with quantum wells active material and quantum dot photonic crystal cavities for light-matter coupling experiments.

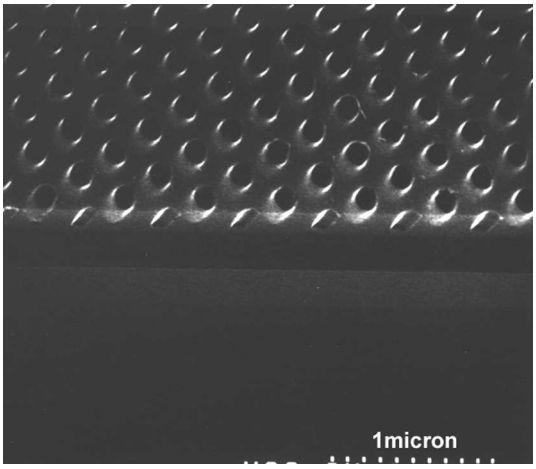

Figure 2.1: Scanning electron microscopy image of ZEP-520 resist patterned by the Leica electron beam lithography system EBPG 5000.

A proper selection of the electron beam resist is very important to obtain the resolution inherent to these lithographic systems. Three types of electron beam resists were used in this thesis work: (1) 950 K molecular weight single layer PMMA resist, (2) ZEP-520 resist, and (3) 950 K/495 K bilayer PMMA resist. PMMA is an abbreviation of poly-methyl methacrylate. PMMA and ZEP-520 resists are positive-type resists for high-resolution purpose, and double layer PMMA resists are also positive resists, which are used when a lift-off process is needed. ZEP-520 resists have much better chemical resistance than PMMA. Etching rates in CHF_3-RIE are 40 nm/minute and 3 nm/minute for 950 K-PMMA and ZEP-520, respectively, while 40 nm/minute for PCVD-grown SiON film. This good selectivity of ZEP resist over SiON film enables us to have more freedom in the fabrication process. Figure 2.1 shows an angle view of patterned ZEP EB resists during photonic crystal fabrication. After resist development, the sample was exposed to oxygen plasma in the RIE system for five seconds in order to conduct resist descum. More details in the etching technique are found in each section below, depending on the materials and structures that were fabricated.

2.2.2 Dry etching

After defining precise designs onto electron beam resists, dry etching is conducted to transfer these patterns into the semiconductor material or an underlining etch-mask layer. Here, four types of etching are shown, depending on material systems.

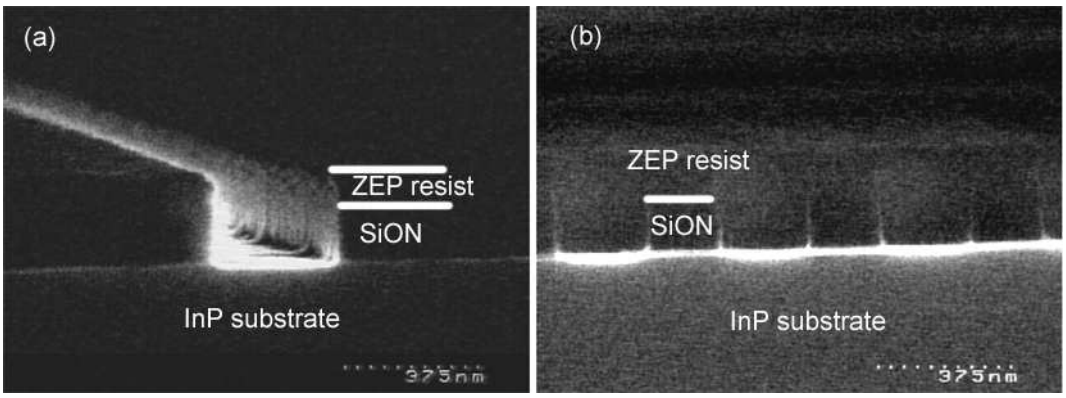

Figure 2.2: Scanning electron microscopy images of SiON samples etched by RIE. ZEP resist was used for the etching mask.

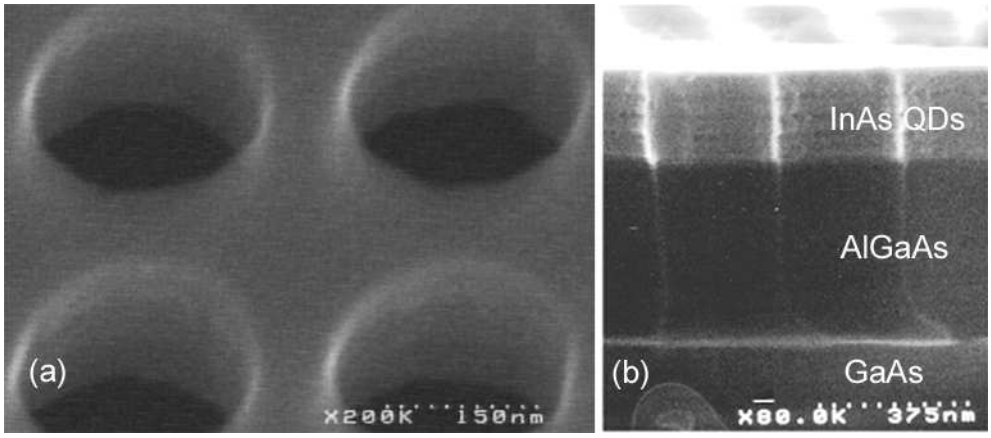

Figure 2.3: Scanning electron microscopy images of InAs/GaAs quantum dot samples etched by Ar-CAIBE method. 950 K PMMA positive resist was used for the etching mask. Three wetting layers under QDs are observed in a white layer written as InAs QDs in panel (b).

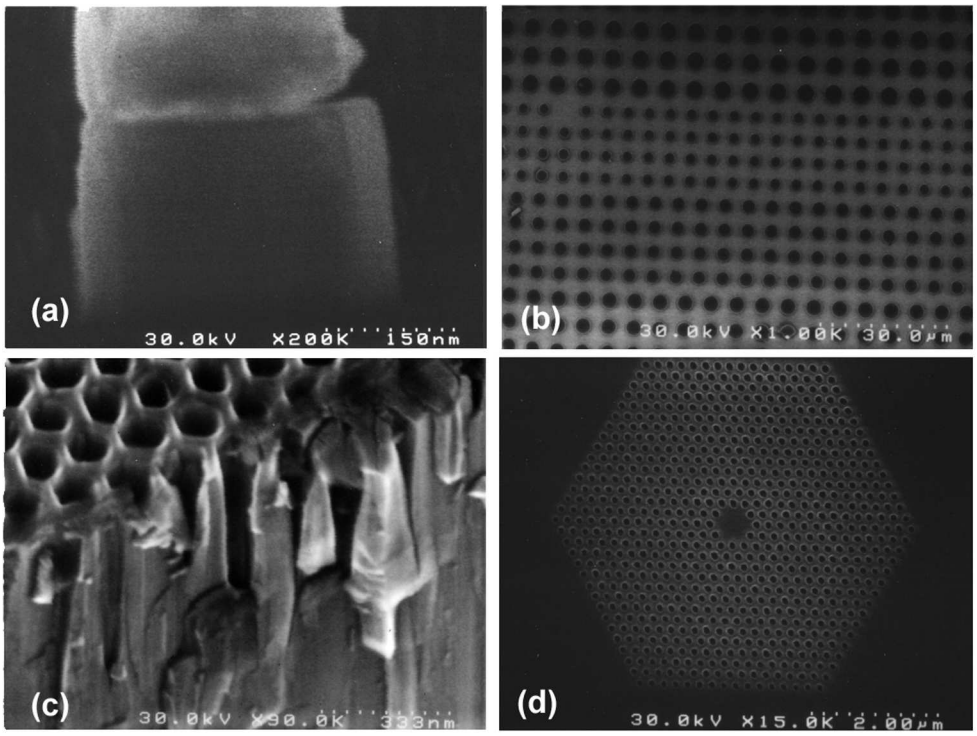

Figure 2.4: Scanning electron microscopy images of InGaN/GaN quantum well samples etched by Xe-CAIBE. A multilayer etching mask, 180 nm 950K PMMA EB resist/50 nm Au/ 30 nm Cr/300 nm SiO_2, was used to fabricate GaN nanostructues for photonic components. Panel (a) is a cross-sectional view of etched GaN structures by CAIBE. Panel (b) shows disk structures. Panels (c) and (d) are two-dimensional photonic crystal defined in InGaN/GaN quantum well material.

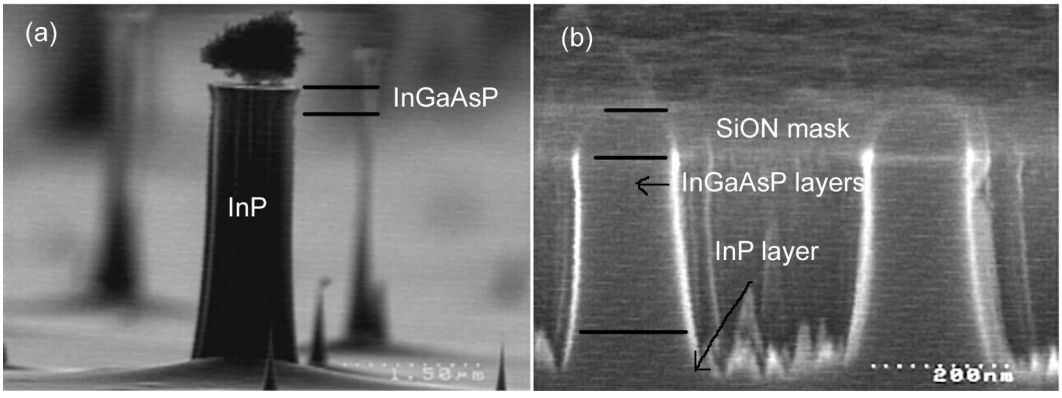

Figure 2.5: Scanning electron microscopy images of InGaAsP/InP QW samples etched by ICP-RIE.

- SiO_2, Si_3N_4, and SiON etching: (RIE) [67]:

  Reactive ion etching is a popular etching technique that employs a capacitively-coupled plasma, and provides an excellent method for etching SiO_xN_y films. Trifluoromethane (CHF_3) was used during RIE of SiO_xN_y films. Patterned resists serve as an etching mask during the reactive ion etching, and the patterned SiO_xN_y film functions as a subsequent mask for etching following this RIE step. High aspect-ratio etching of SiO_xN_y films is obtained in our system when using CHF_3 flow rates of 20sccm, process pressures of 16 mTorr, input powers of 90 W, and a parallel plate distance of 3 inches. The DC bias is typically around 500 V, and the etching rate is 40 nm/min. Figure 2.2 shows a cross sectional image of SiO_xN_y film patterned using CHF_3-based RIE.

- InAs/GaAs quantum dot systems: CAIBE [104]

  Chemically assisted ion beam etching (CAIBE) was used to etch InAs/GaAs QD films. An accelerated argon ion beam is responsible for backscattering and eroding atoms from the sample surface during etching. Chlorine molecules are attached to the sample surface and disassociate at the surface due to the high vapor pressure of the attached surface compounds such as $GaCl_2$ or $AsCl_3$. The combination of these two processes allows us to develop anisotropic etching procedures. High aspect ratio etching of InAs/GaAs QD films is obtained in our systems under the following condition: Argon pressure = 2×10^{-4} Torr, argon acceleration voltage = 500 V, ion beam current = 10 mA, chlorine gas flow = 550 sccm, chlorine jet distance to the sample = 15 mm. The etching rate for a few hundred nanometer hole pattern array, typical in photonic crystals, is 100nm/min. Figure 2.3 shows cross sectional images of InAs/GaAs QD film etched by Cl_2 -based CAIBE. The CAIBE has an advantage in selectivity with respect to resists compared to typical plasma etching methods such as (ICP)-RIE because in the RIE, plasma species that do not contribute to the substrate etching can still attack and erode the mask. On the other hand, only the desired gas species for etching the semiconductor are injected and approach the sample surface during a CAIBE process.

- InGaN/GaN quantum well systems: CAIBE [103]

Gallium nitride is one of the most difficult semiconductor materials to be etched because of its inherent hardness and etch resistance resulting from its high cohesive bonding energy. Chemically assisted ion beam etching can be used to etch InGaN/GaN quantum well films. Accelerated xenon ion beams assisted by a chlorine gas jet enables the manipulation of anisotropic etching conditions of GaN. Xenon gas is used to enhance the sputtering rate, as more energy is deposited locally at the surface when milling with this ion species. High aspect-ratio etching of InGaN/GaN films was obtained in our CAIBE system under the following conditions: Xenon pressure = 2×10^{-4}Torr, xenon acceleration voltage = 1,500 V, ion beam current = 30 mA, chlorine gas flow = 1,000 sccm, chlorine jet distance = 10 mm, and substrate temperature = 200^{o}C. The etching rate for 100 nm-diameter hole pattern of photonic crystals is 300 nm/min. Figure 2.4 shows cross sectional images of InGaN QW film etched by Cl_2-based CAIBE system. The anisotropy of the etching of GaN material is evident in Figure 2.4(c).

- InGaAsP/InP quantum well systems: ICP-RIE [46]

  InGaAsP semiconductor is also a difficult material to etch anisotropically. Inductively coupled plasma reactive ion etching was used here to etch InGaAsP/InP films. The inductively driven source at 13.56MHz provides a good discharge efficiency because only a smaller part of voltage is dropped across the plasma sheath, which is a thin positively charged layer, and the loss of ion energy is much smaller than capacitive coupling. This efficient plasma discharge makes the plasma density larger than the one in a comparable RIE process. Therefore, the ICP-RIE method is particularly suitable to drill nanometer-scale holes efficiently. Moreover, hydrogen iodide vapor can be used to react with indium atoms in InP material even at room temperature whereas chlorine gas typically leaves $InCl_3$ deposits, which can be removed only at 150 ^{o}C or higher surface temperatures. On the other hand, chlorine is a very reactive gas for etching GaAs materials. Therefore, a mixture of HI vapor and chlorine gas was employed as an optimal reactive gas mixture to etch InGaAsP films. Anisotropic etching of InGaAsP/InP quantum well material was optimized in our system under the condition: HI flow = 20 sccm, H_2 gas flow = 9 sccm, Cl_2 gas flow = 5 sccm, process pressure = 10 mTorr, ICP power = 850 W, and RF power = 100 W. The

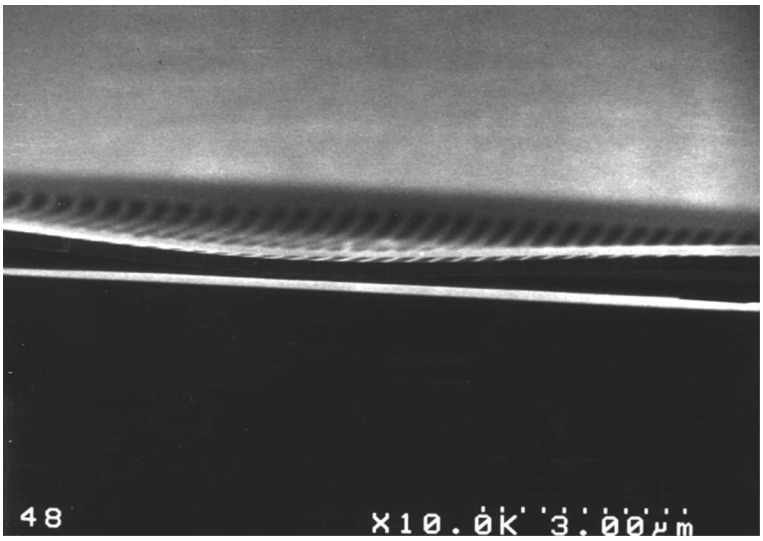

Figure 2.6: Scanning electron microscopy image of a structure bent by surface tension when dried in water.

etching rate of InGaAsP film is 300 nm/min. Figure 2.5 shows cross sectional images of etched InGaAsP quantum wells on InP substrate. The line features on the sidewall are results of surface roughness on the material , created by Indium droplets at the end of SiON etching.

The sample drying process is crucial in fabricating precise and symmetric membrane structures. Trapped liquid underneath the membranes pulls the membranes down during the evaporation process as a result of surface tension. In particular, water has a large surface tension force due to the polarized charge distribution of water molecules. Figure 2.6 shows an example of a bent structure distorted due to surface tension forces during drying. To avoid this undesirable effect, we typically employ hexane or isopropyl alcohol as the last rinsing solvent after the dissolving reagent is removed in water. The organic solvents exert a smaller external force on the membranes during drying, and prevent distortions. A more sophisticated way to avoid this problem consists of using a critical point drying system for removing the solvent. Critical drying uses an equilibrium phase in the P-T phase diagram above the critical point, that allows liquid and gas to exist simultaneously. This is achieved by pressurizing and heating the liquid until it reaches the gas-liquid mixture state (P,T)$>\simeq$(7×10^{16} N/m^2, 50 ^{o}C), which is the critical point of CO_2. Then, following reduction of pressure, the sample is cooled down to reach the point of ambient temperature

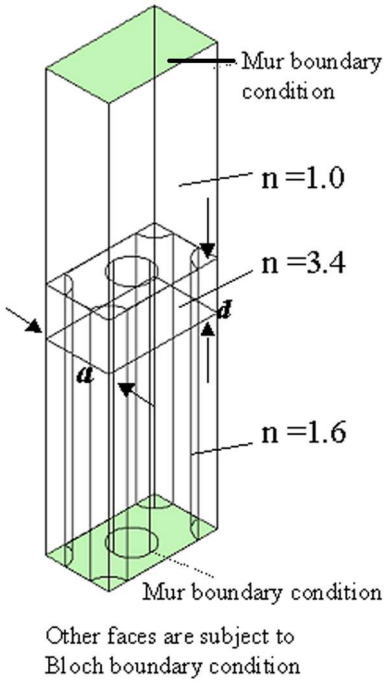

Figure 2.7: Analyzed structure for 3D-FDTD. The analyzed structures are asymmetric in z-direction, resulting in intermixing TE modes with TM modes.

and atmospheric pressure. This way, without drying membranes in liquid phase, symmetric membranes can be fabricated.

2.3 Triangular-Lattice Asymmetric Structure: Intermixing of TE and TM Modes

Planar photonic crystal platforms exhibit many interesting and potentially useful applications. To fabricate high-Q planar photonic crystals, for example, we might consider asymmetric structures for a simpler fabrication process. Cavities formed on a solid substrate offer greater opportunities for operating electrically pumped light emitters because the substrate provides both heat sinking and a convenient current pathway. However, we have to take into account the accompanying performance deterioration of light confinement in such asymmetric structures, in particular those resulting from the intermixing of TE and TM modes [104, 21].

To determine the bandgap in an asymmetric planar photonic crystal structure, we have analyzed the structure shown in Figure 2.7. The photonic crystal is sandwiched between

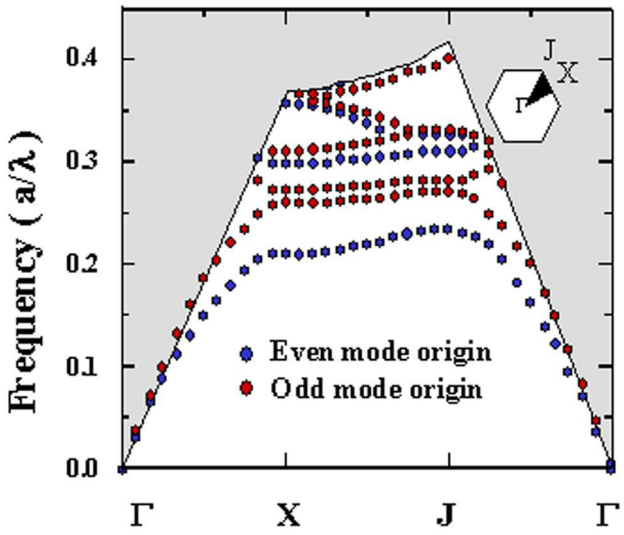

Figure 2.8: Photonic band diagram of asymmetric planar photonic crystal slab.$r/a = 0.3$,$d/a = 0.75$.

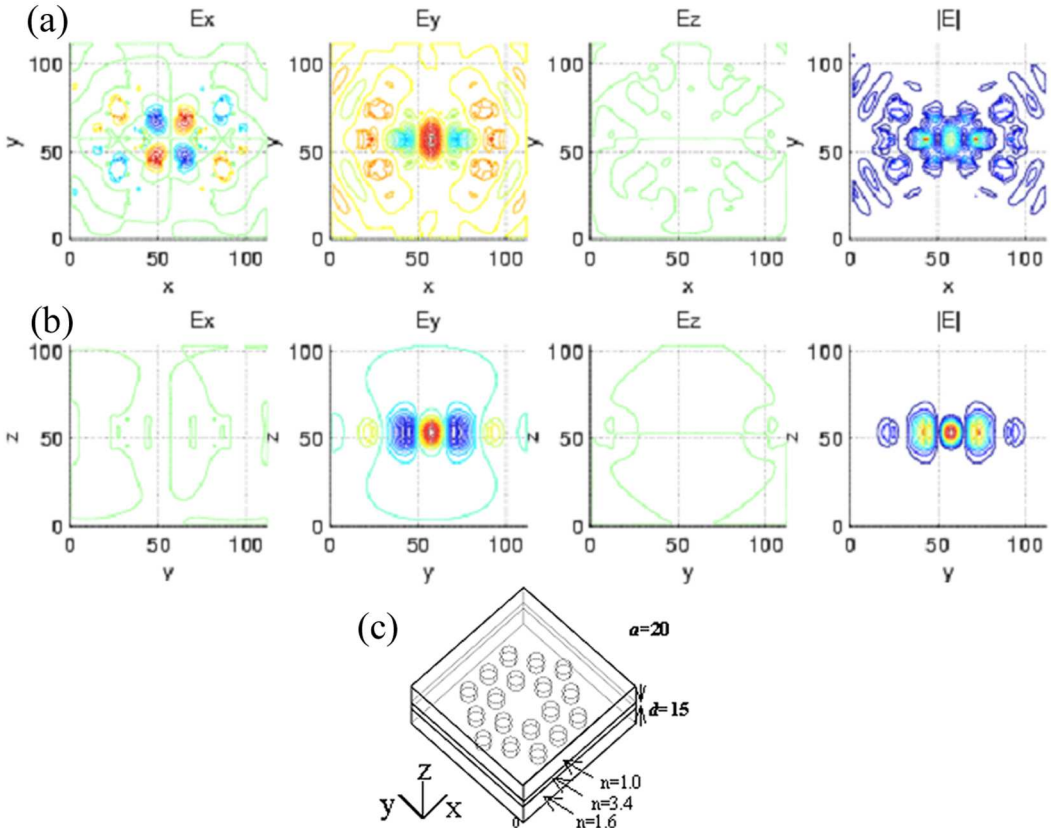

Figure 2.9: Y-dipole mode excited in an asymmetric planar photonic crystal cavity.

air and AlO_x layers on either side. Moreover, the AlO_x layer is perforated by a triangular lattice array of holes to imitate our designed structures. A 3D-FDTD model [85] was used with Bloch boundary conditions on the vertical sidewalls and absorbing boundary condition at the top and bottom boundaries. The refractive indices used for this modeling exercise are 3.4, 1.6, and 1.0 for GaAs, AlO_x, and air, respectively. Figure 2.8 is a calculated band diagram for the resultant asymmetric photonic crystals. In this figure, the TE modes have a bandgap of 0.07 in a unit of a/λ with a midgap of 0.27 while a similar symmetric structure provides a bandgap of 0.085 with a midgap of 0.28. The electric field profiles on two different orthogonal slices are shown in Figure 2.9.

Translational symmetry of photonic crystal determines allowed Bloch waves propagation in the crystal, and localized modes created by disorder in the periodic lattice are represented by a superposition of the Bloch wave states. Therefore, symmetry analysis [60, 71, 72, 73] is useful in predicting the mode characteristics lattice-type by lattice-type. It is noted that there are also photonic (quasi-)crystals with rotational symmetry. For a triangular lattice, two-dimensional photonic crystal slabs sandwiched by air, from a viewpoint of space group, are $D_{6h} = C_{6v} \times \sigma_h$ groups whereas slabs sandwiched by air and a substrate are asymmetric by a (σ_h) operation and are classified as C_{6v} groups. Likewise, for a square lattice, slabs with symmetry by a σ_h operation have D_{4h} groups, and ones with asymmetry by a σ_h operation are C_{4v} groups. Using this group information, modes can be constructed. Readers can find good references to analyze photonic crystal structures from a group theory viewpoint.

2.3.1 Asymmetric photonic crystal nanocavity with quantum dot internal light sources

Quantum dots (QDs) [9, 84] are three-dimensionally confined electronic structures with lateral dimensions on the order of the *de Broglie* wavelength. When used as light sources, quantum dots provide fascinating properties such as atom-like density of states and narrow emission linewidth. Moreover, the past efforts on growth of QDs, especially self-assembled QDs, now enable us to use QDs as reliable emission sources. Here we show that active QDs can be embedded within high-Q photonic crystal microcavities to create light emitting devices. For solid-state microcavities, an ensemble of QDs or a single quantum dot could be used as a narrow spectrum light source which matches the linewidth of a high finesse cavity. It is predicted that such a quantum dot source, included in an optical nanocavity,

would result in a very low threshold laser source. The In(Ga)As system is also found to have low surface recombination rate, and therefore is a good candidate for constructing light emitting devices from photonic crystal nanocavities in which large surface to volume ratios are unavoidable. While an ensemble of QDs often results in inhomogeneous broadening and limits the benefits of using quantum dots in larger cavities, the emission linewidth of a single QD is subject to only homogeneous broadening. Thus, at low temperature, single QD emission within a narrow linewidth nanocavity can result in large enough fields to modify the spontaneous emission processes and to demonstrate strong coupling. The use of narrow-linewidth sources, available from QD emission, is key in providing the desired large enhancement of intensity for weak light-matter coupling.

2.3.2 Sample preparation of 2-D photonic crystal cavity with a broken symmetry in the vertical direction.

We describe the sample preparation of two-dimensional photonic crystal slab nanocavities fabricated on an AlO_x layer, which breaks the symmetry in the z-direction, and contains InAs self-assembled quantum dot active material. Epitaxial quantum dot layers were grown on (001) GaAs by molecular beam epitaxy. Three stacked InAs QD layers were clad by $Al_{0.16}Ga_{0.84}As$ layers on top of a 400 nm $Al_{0.94}Ga_{0.06}As$ layer. The QDs density in these samples is 3×10^{10} dots/cm^2. A GaAs cap layer was added to protect the top of the epitaxial structure on the final layer. The overall cavity thickness (d) was designed to be 240 nm and was grown by Dennis Deppe's group [20, 19, 32, 33, 62, 78, 77] at the University of Texas, Austin. The ground state emission of the QDs used in this study showed inhomogeneous broadening as narrow as 43 meV. The layer structure is shown in Table 2.2.

The patterns forming the triangle-arrayed photonic crystal defect cavity were defined in a 250nm-thick poly-methyl methacrylate (PMMA) resist, which was spun on the quantum dot epilayers and exposed using the Hitachi field emission electron beam lithography system. Photonic crystal cavities are surrounded by ten layers of PBG, and the lattice spacing (a) was lithographically controlled from 270 nm to 390 nm. The ratio of hole radius (r) to lattice spacing a was similarly tuned from 0.16 to 0.4. After lithography, the beam-written patterns were transferred through the active membrane by using an Ar^+ ion beam assisted with a Cl_2 jet, and the $Al_{0.94}Ga_{0.06}As$ layer under the cavities was subsequently oxidized in steam at 400 ^{o}C for 5 minutes to define a perforated dielectric slab structure on top of

Material	Function	Doping [cm^{-3}]	Thickness [nm]	QD Density [/cm^2·layer]
n-GaAs	cap layer	1×10^{17}	10	
n-$Al_{0.16}Ga_{0.84}As$	carrier confinement	1×10^{17}	50	
i-GaAs	barrier	undoped	25	
i-InAs QDs	Active region	undoped	5	$1{\times}10^{10}$
i-GaAs	barrier	undoped	25	
i-InAs QDs	Active region	undoped	5	$1{\times}10^{10}$
i-GaAs	barrier	undoped	25	
i-InAs QDs	Active region	undoped	5	$1{\times}10^{10}$
i-GaAs	barrier	undoped	25	
n-$Al_{0.16}Ga_{0.84}As$	carrier confinement	1×10^{17}	50	
n-GaAs	-	1×10^{17}	10	
n-$Al_{0.94}Ga_{0.06}As$	sacrificial layer	1×10^{17}	400	
n-GaAs	substrate	1×10^{18}		

Table 2.2: Layer structures of quantum dot samples used for asymmetric photonic crystal nanocavities

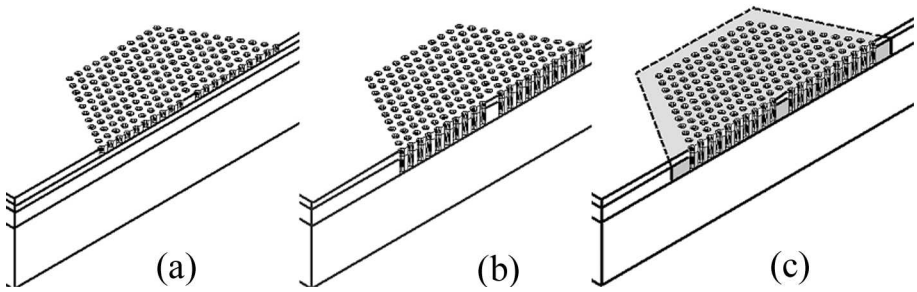

Figure 2.10: Fabrication procedures for asymmetric planar photonic crystal cavities. (a) structure after electron-beam lithography, (b) after chemically-assisted ion beam etching, (c) after wet-oxidation.

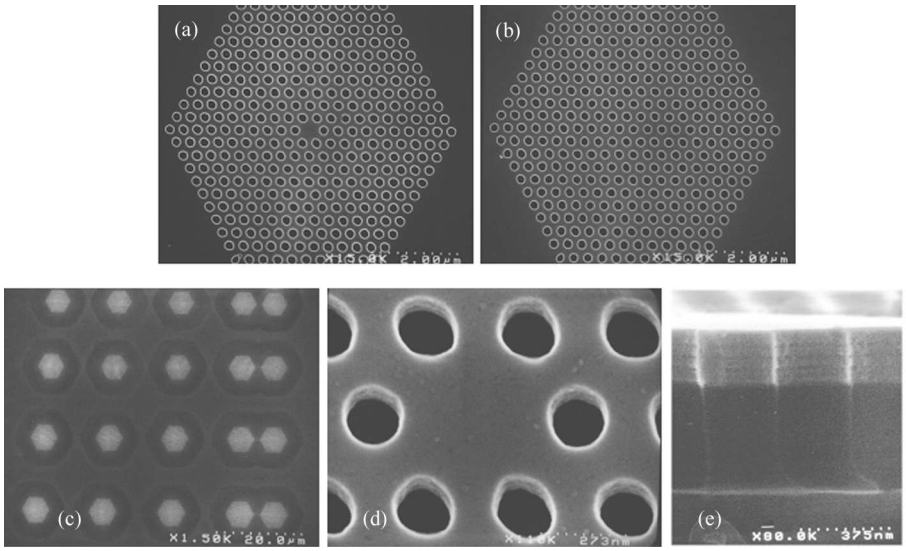

Figure 2.11: Images taken by scanning electron microscopy for 2-D photonic crystal single-defect cavity used in this work. (a) entire cavity, (b) photonic crystals without a center defect, (c) an array of photonic crystal cavities, (d) a single defect, and (e) side view of a sample.

an AlO_x cladding layer. For most of the structures, the $Al_{0.94}Ga_{0.06}As$ was oxidized as far as 3 μm from the edge of photonic crystal hexagons. Figure 2.11 shows images taken by scanning electron microscopy for an array of photonic crystal cavities with a single defect used in this report. The precise transferred pattern can be seen in these figures. Light parallel to the surface is confined by Bragg reflection from the photonic crystal in the plane whereas the high index slab structure is used to vertically confine light by total internal reflection.

2.3.3 Characterization of quantum dot photonic crystal cavity with a broken symmetry in a vertical direction.

Optical pumping normal to the surface was carried out by using an 830nm semiconductor laser diode operated by 2.5 μsec wide pulses with a 3 μsec period. The 830 nm pump light can be absorbed only by the InAs quantum dots and the wetting layers, and the pump light can be focused onto the sample surface with a spot diameter of 2 μm. Light emission was extracted from the sample surface and detected using an optical spectrum analyzer. The peak pump power was 2.4 mW, which corresponds to a power density of 75 kW/cm^2. All of the measurements were performed at room temperature. Figure 2.12 shows typical

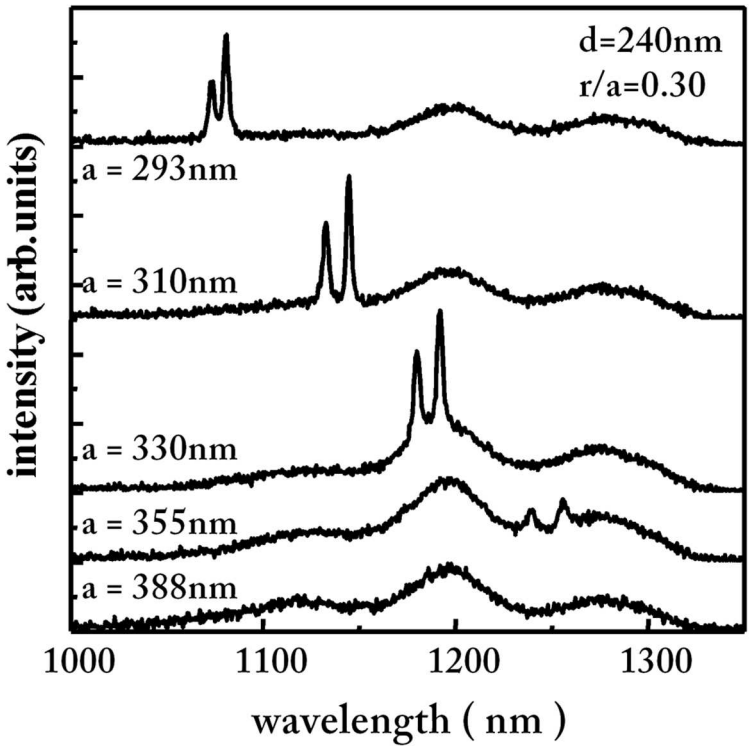

Figure 2.12: Photoluminescence spectra for samples with different lattice spacing (a) and same r/a of 0.30.

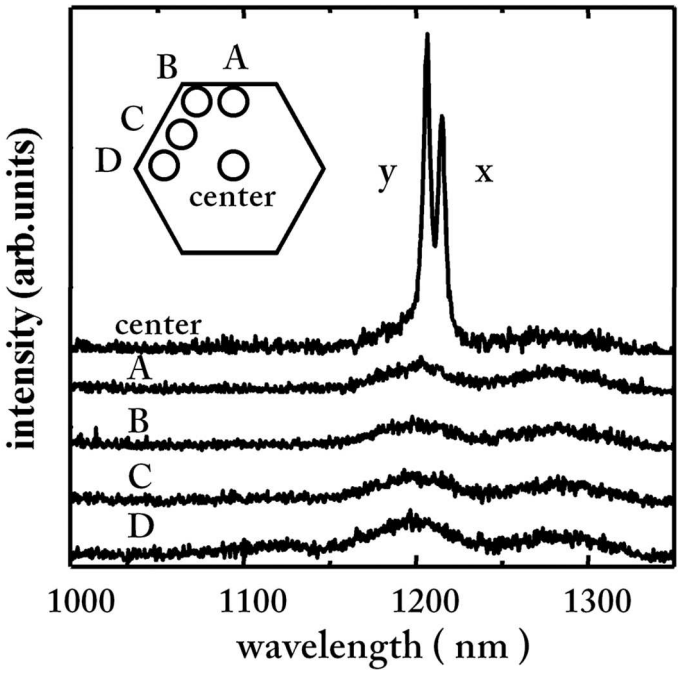

Figure 2.13: Position-dependent photoluminescence for a photonic crystal with a single defect. The spectra labelled as A, B, C, and D were taken in each point in a cavity away a single defect as shown in an inset.

photoluminescence spectra for photonic crystal single-defect cavities with different lattice spacings and identical r/a. The cavity resonance was measured to exhibit a 3 to 5 nm emission linewidth, and the spectrum was found to change significantly by the introduction of small lithographic changes to the patterns. Therefore, the experimental $\lambda/\Delta\lambda$ values are around 300, which corresponds to results from our 3D-FDTD analysis. The spectra of the resonant modes can be tuned throughout the emission range of the quantum dots by changing the lattice period of the photonic crystal [58]. However, it is noted that d/a values are varied when lattice spacings are modified. One might wonder why broad quantum dot emission is detected in the spectra. Quantum dots emit light in three dimensions, and some components are within an escape cone defined by the air/GaAs interface. Therefore, we see resonant emission as well as inhomogeneously broadened QD emission.

We also conducted position-dependent μ-photoluminescence measurement to approximately determine the mode volume of the donor modes. Figure 2.13 shows photoluminescence spectra taken in different points of the photonic crystal pattern described in the inset. Pumping points labelled as A, B, C, and D are within the photonic crystal, but

close to the edge of the pattern. We found that only the spectrum taken from the center of the photonic crystal pattern exhibits the two resonance peaks associated with the optical nanocavity modes while the other points exhibit weak QD emission in the spectra. Although only four points close to the edge of hexagon are shown in this figure, many other points were tested and the result was carefully verified on many patterns. Optical pumping on points close to the edge was not related to the two distinct peaks in the spectrum, which we expect to originate from the localized donor modes. Since the pumping diameter is 2 μm and the distance from the center of the cavity to the edge is 3.5 μm, the measured modes are well confined to the single-defect cavity. We believe, from these data, that carrier diffusion length is short relative to the lattice spacing. The pair of modes observed in Figure 2.13 is a result of the two perpendicular dipole modes in this cavity. When filtering the spectrum with a broadband polarizer, we observe that each of these peaks is purely x- or y-polarized as described in the figure, and the higher energy line corresponds to y-polarized light. Spectral splitting of donor modes ideally does not occur in a completely symmetric single-defect cavity within a two-dimensional photonic crystal, since the structure with a C_{6v} symmetry leaves two degenerate eigenmodes. Therefore we expect the measured mode splitting of around 1% relative to the frequency in the figure to result from fabrication fluctuations within the photonic crystal close to the cavity. Such a degeneracy lifting occurs even in 3D-FDTD simulations by coarse samplings for constructing photonic crystal structures. Resonances at a=355 nm in Figure 2.12 show broader emission linewidth. This might be a result of changes in the effective photonic bandedge during lithographic tuning since the d/a ratio is inadvertently altered.

We also measured photoluminescence from cavities defined within photonic crystals with different r/a values, which favored extended modes. As an example, Figure 2.14 shows photoluminescence spectra for two photonic crystals with r/a values varying from 0.16 to 0.37. Photoluminescence spectra from such photonic crystals with single-defect cavities can be compared with those taken from photonic crystals without defect cavities. For r/a=0.37, the spectrum from the photonic crystal defect cavity again shows the two dipole modes associated with the localized donor mode. There are no other significant features in this spectrum. However, for photonic crystals with r/a=0.16, a set of sharp lines is observed in addition to the two dipole resonances. Moreover, the photoluminescence spectra from photonic crystals without defect cavities also demonstrate similar sharp resonances, and

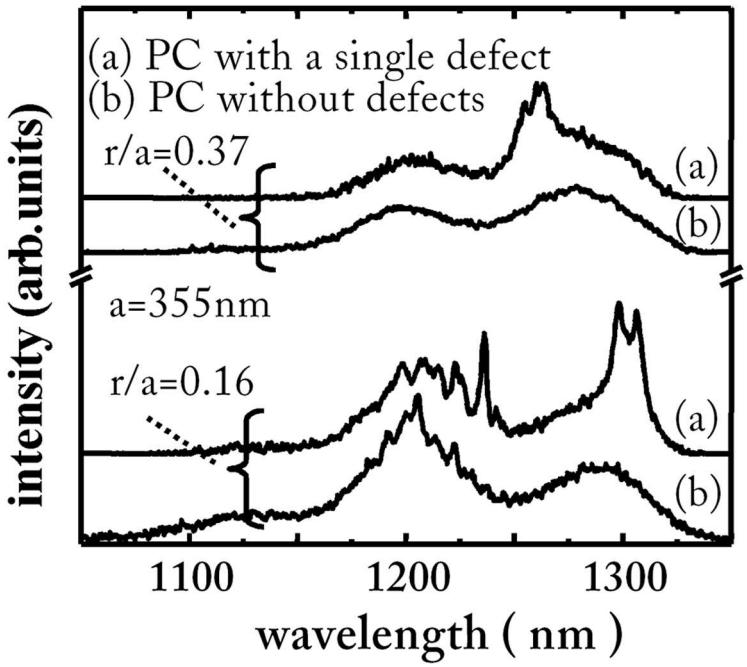

Figure 2.14: Photoluminescence spectra for photonic crystal cavities with a single defect and without a defect for r/a of 0.16 and 0.37. The lattice spacing is kept at 355 nm.

these lines are attributed to shallow modes from lithographic variations in the photonic crystal itself. There tends to be a qualitative correlation between the number of sharp lines and the fluctuations in the hole dimensions from the PBG crystal surrounding the cavities. Anderson localization [2] is an electronic bound state caused by random fluctuations of scattering in crystals, and our observations in photoluminescence spectra are similar to the Anderson localization. For electrons, complex amplitudes are summed over all trajectories. In perfectly aligned crystals, there is constructive interference allowing the propagation of electrons. However, random fluctuations of crystal lattice points disturb this constructive interference sufficiently to localize the electrons. Likewise, the random fluctuations of photonic crystal lattice induce a similar disturbance of constructive interference for photons. The Anderson localization effects can be frequently seen around photonic bands, not deeply in photonic bandgap.

This discussion is supported by position-dependent μ-photoluminescence spectrum measurements, as shown in Figure 2.15, which were taken both in the center and close to the edges. Thus, the sharp peaks are signatures of band edge modes and/or shallow impurity modes. For r/a of 0.16, the donor mode is closer to the air band edge than the ones for

r/a of 0.37, and more likely to support shallow acceptor modes. Thus, we typically do not see both donor modes and shallow band-edge modes in the measured range of wavelength. When fluctuations are completely removed from the photonic crystals, we believe that the localized modes caused by the Anderson localization should also be removed.

In order to confirm that negligible resonant emission is seen by pumping at the edges of a photonic crystal lattice, 3D-FDTD analysis was employed. Figure 2.16 (a) is an analyzed planar photonic crystal, which has seven layers around a defect. An initial source is prepared in the structure to excite localized modes and obtain mode profiles. In this case, the initial source position is a parameter, and the coordinate is $(x, y) = (0, na\sqrt{3}/2)$ where n is a non-negative integer. Therefore, the initial source is located at the n-th photonic crystal layer on the y-axis. For example, the initial source in the figure is positioned at the seventh layer of photonic crystal cavity to model optical pumping of modes at the photonic crystal edges. Doubly-degenerate dipole modes are excited and the dipole modes are seen at $a/\lambda \simeq 0.280$ in an H_z spectrum of Figure 2.16(b). The air and dielectric band edges are seen at 0.325 and 0.245, respectively. The spectrum was constructed by summing up components at several points around the defect. The crystal symmetry was considered to pick up the pumping points. The H_z amplitudes of dipole mode, air band, and dielectric band are plotted in Figure 2.17. Whereas dipole modes have a monotonic decrease trend in the amplitude, both air and dielectric bands do not have strong correlation with the initial source position. This simulation supports our measurement observations, which showed strong location dependence for dipole modes. This analysis assumes that no carrier diffusion is involved in the process, but such perforated structures, by nature, are believed to have short diffusion length.

2.4 Improvement of Q Factors in Symmetric Planar Photonic Crystal Cavities

The combination of high-quality factors and small mode volumes are two important attributes for high performance nanocavities. High-Q microcavities will become very important in enhancing interactions between photon system and carrier system and obtaining novel light emitters. Our photonic crystal cavities are constructed in thin slabs, which are perforated with triangular hole arrays and used to define photonic crystal mirrors. In

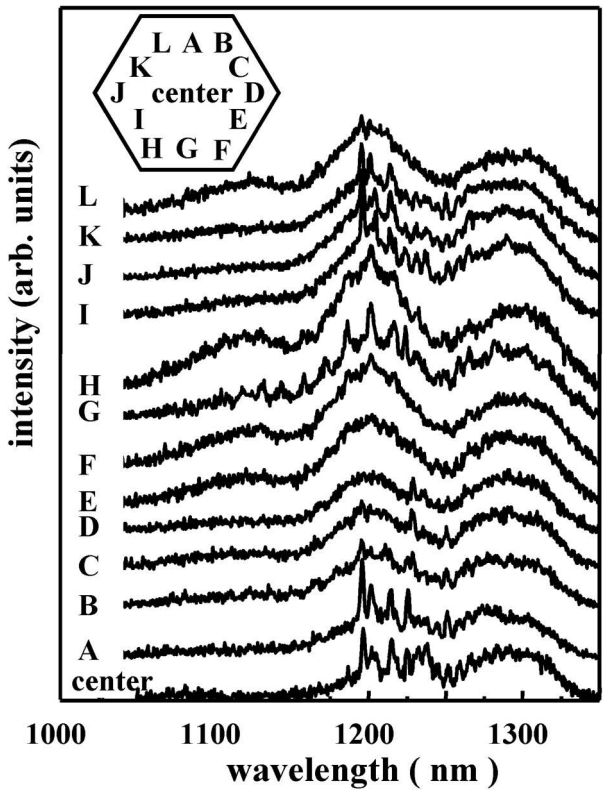

Figure 2.15: Position-dependent photoluminescence for a photonic crystal without defects. The spectrum labelled from A to L were taken in each point in a cavity away a single defect as shown in the inset.

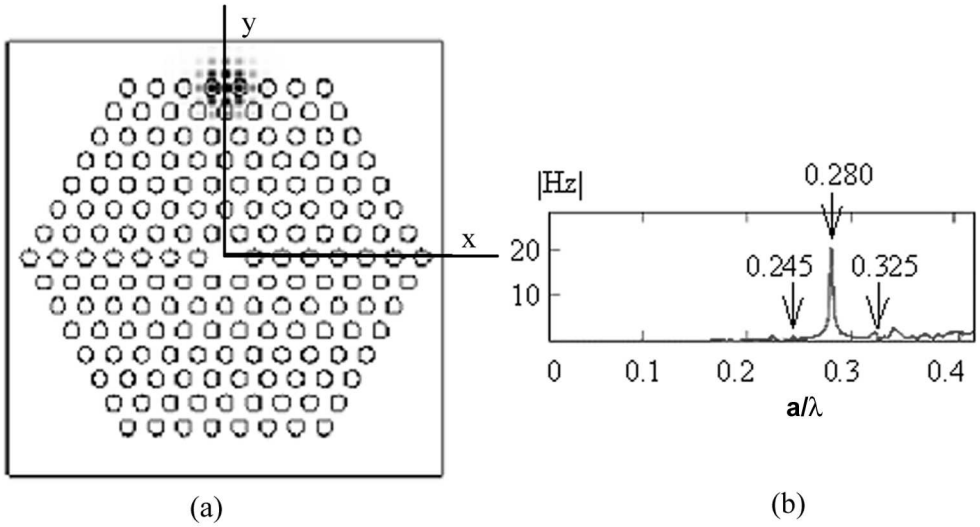

Figure 2.16: 3D-FDTD analysis setup. Initial light source was prepared at a point $(0, y_0, 0)$ as a Gaussian source. A panel (a) shows the initial source position in a photonic crystal cavity. A panel (b) shows an example of the Fourier spectrum obtained with the initial source.

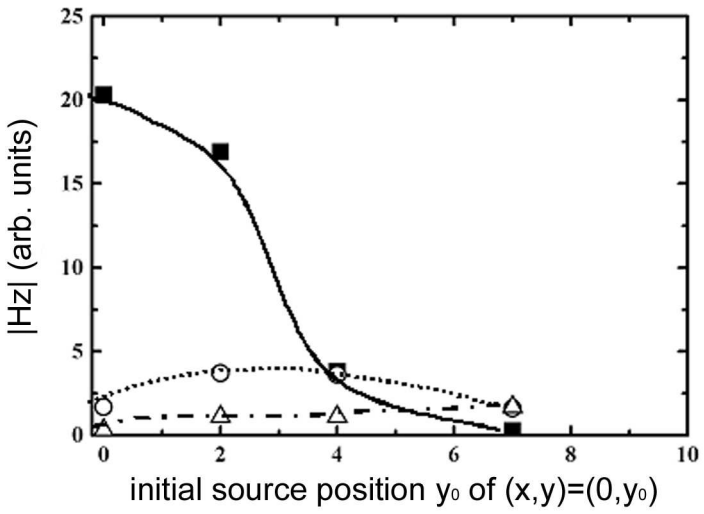

Figure 2.17: $H_z(\omega_i)$ dependence on a distance from a cavity center to an initial source. Black squares, open circles, and open triangles are data for dipole modes, air bands, and dielectric bands, respectively. $a' = \sqrt{3}a/2$.

the simplest defect cavity designs, regardless of whether we increase the number of defects forming the cavity, it has so far not been possible to demonstrate both small mode volume and high-Q factors. In the preceding section, low-Q localized modes are measured on an aluminum oxide substrate. In this section, modification of symmetric cavity structures is used to obtain improvement of cavity quality.

The maximum Q factors for donor cavities with D_{6h} symmetry are around 1500 from extended modes in empty lattice photonic crystal cavities [34], but the mode volume is much larger than that found in single-defect cavity modes, which is comparable to several times $(\lambda/2n)^3$. Previous work to obtain higher Q values has focused on thin slabs patterned within hexagonal hole patterns missing several holes within a photonic crystal lattice. However, those cavities are not suitable for many applications since they also have relatively large mode volumes and many modes exist within the semiconductor emission range. An example is the H3 cavity shown in Figure 2.18. The mode volume is $1.2(\lambda/n)^3$, and the vertical quality factor is 900. Large mode volumes efficiently decrease the field intensity within the cavity, and a higher number of modes induced by the cavity size inadequately increase radiation coupling with uninterested modes, meaning a reduction of spontaneous coupling factors. Typical well-confined donor mode cavities have small mode volumes, but also

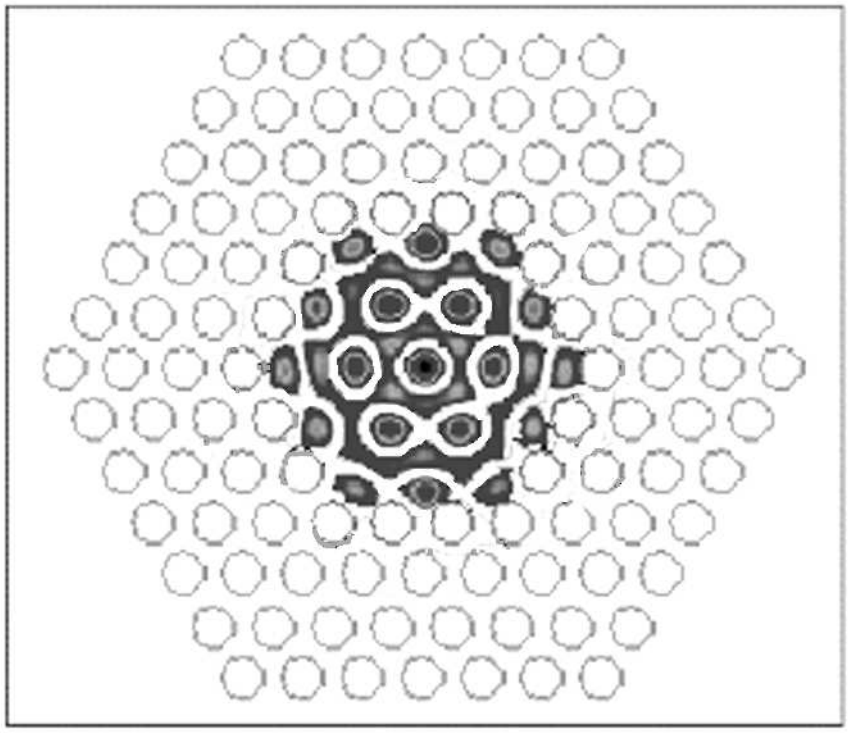

Figure 2.18: Magnetic field amplitude in a middle of slab of H_3 cavity.

suffer from relatively low Q values, which are usually limited by vertical scattering losses. To address the problem, Vučković *et al.* [91] predicted by 3D-FDTD calculations that single-defect cavities with fractional edge dislocations can have well-localized modes with surprisingly high-Q values of as high as 30,000. In this section, we describe the experimental demonstration that by using fractional edge dislocations in photonic crystal cavities, it is possible to measure microcavities with high-Qs as well as small mode volumes.

2.4.1 Design of triangular lattice high-Q cavity

Figure 2.19 is a schematic of a cavity used to see improvements in quality factors. Our single-defect photonic crystal nanocavity is constructed within a thin slab of GaAs, which is perforated with a triangular lattice of holes. A single smaller hole replaces a larger hole within the center of this slab to define the optical cavity. This cavity supports doubly degenerate shallow donor states. In our design, we have modified this geometry in two important ways: (1) In the x direction, in line with the smaller hole, ellipsoids rather than circles are fabricated at lattice spacing (a) with an elongated major axis of $2r + s =$

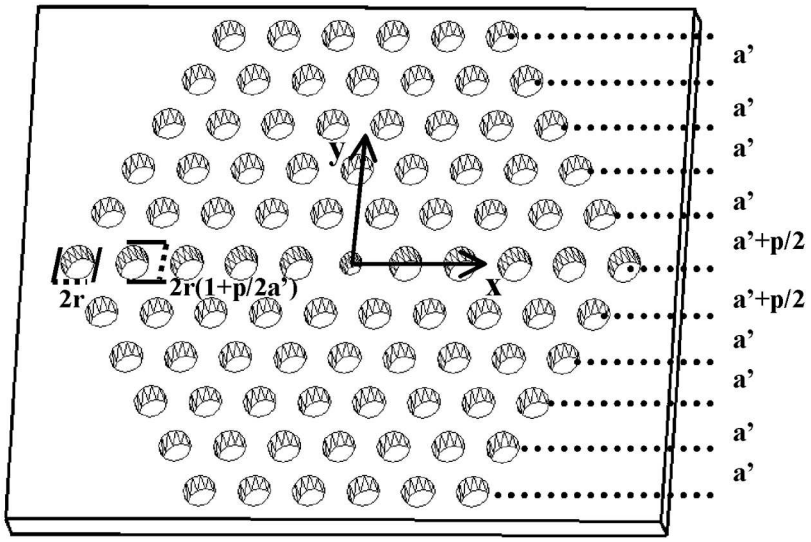

Figure 2.19: A schematic drawing shows a two-dimensional photonic crystal slab cavity with fractional edge dislocation.

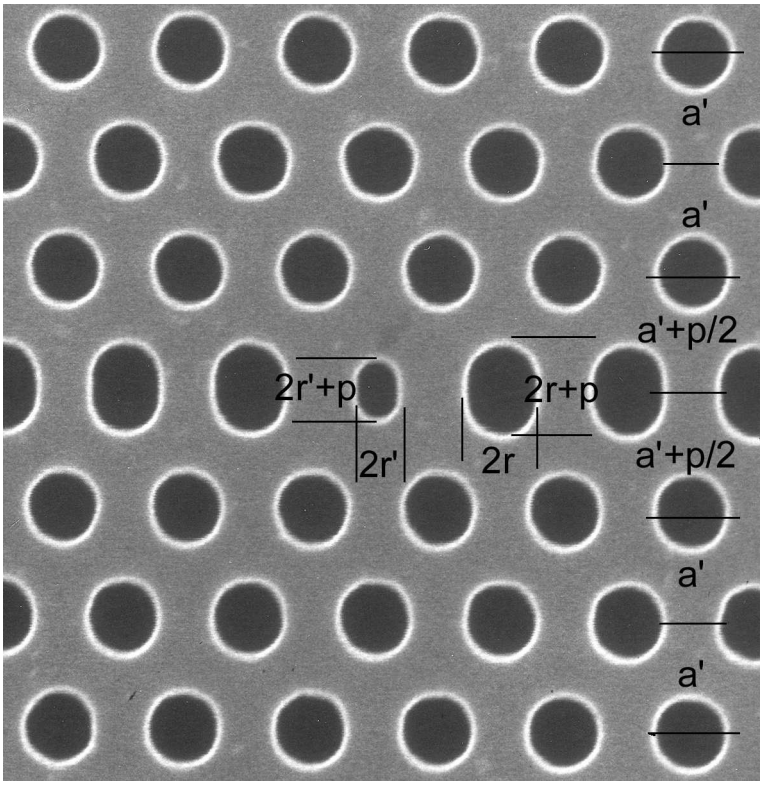

Figure 2.20: Fractional edge dislocation design. It should be noticed that this design is slightly different from a design used in this work shown in Figure 2.19. The elongated hole sizes is different on x-axis.

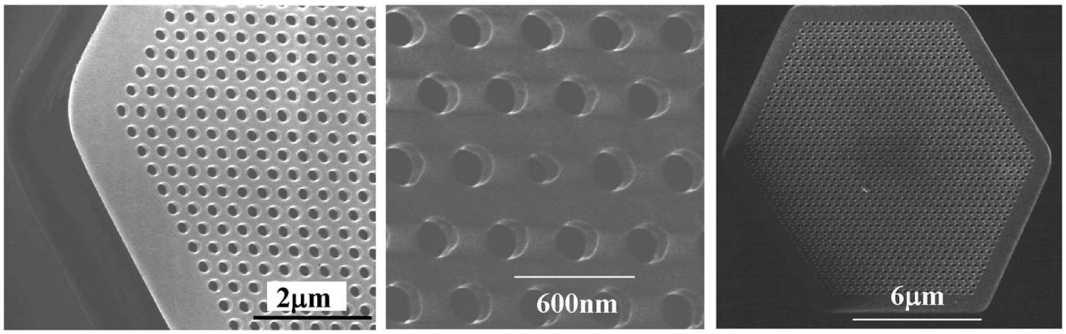

Figure 2.21: Scanning electron microscopy image of photonic crystal slab with fractional edge dislocation.

$2r(1+p/2a')$ where r is a radius of original hole, $a' = \sqrt{3}a/2$ is an original distance of vicinal lattice array in y direction and p/a is an elongation parameter. (2) Holes are moved away from the x axis by $p/2$ toward the +y or -y direction. In the +y or -y direction, the minor axis of ellipsoids remains as $2r$. These two operations are similar to adding a fractional edge dislocation in the y direction. It should also be noted that Vučković *et al.* used the major axis of ellipsoids of $2r + p$ which is larger than the value $2r(1 + p/2a')$ used in this article. The fabricated designs on InAs QD material is shown in Figure 2.20. However, the idea is effectively identical.

2.4.2 Mode characterization of high-Q 2-D photonic crystal cavity.

Self-assembled quantum dots are employed as the light-emitting material grown on (001) GaAs by molecular beam epitaxy. Three stacked InAs quantum dot (QD) layers (QDs density: 3×10^{10} dots/cm^2) were clad by $Al_{0.16}Ga_{0.84}As$ layers on top of a 400 nm $Al_{0.94}Ga_{0.06}As$ layer. A GaAs cap layer is then added to protect the top on the final layer. The cavity thickness (d) is 240 nm. The ground state emission of QDs used in this report showed linewidths as narrow a 40 meV. The ground state emission at room temperature peaks around 1240 nm. The sample layer structures are very similar to Table 2.2.

The patterns for forming hexagonal-array photonic crystal defect cavities were lithographically defined. Photonic crystal cavities are surrounded by twenty layers of photonic crystal for good confinement of light within the photonic crystal plane. The lattice spacing (a) used in this work is lithographically controlled to 370 nm (d/a=0.65). After lithography, the beam-written patterns were transferred through the active membrane by using

an Ar^+ ion beam assisted with a Cl_2 jet, and the $Al_{0.94}Ga_{0.06}As$ layer under cavities was subsequently oxidized in steam to define a perforated dielectric slab structure on top of an AlO_x cladding layer. Then, the AlO_x layer was completely dissolved in potassium hydroxide solution, and the sample was carefully rinsed and dried. Figure 2.21 shows images taken by scanning electron microscopy (SEM) for photonic crystal cavities containing a single donor defect with fractional edge dislocations. We fabricated samples with four different p/a values ($p = 0, 10a$,$0.15a$, and $0.20a$). The value of the hole radii defining the photonic crystals r ranged from $0.28a$ to $0.29a$, whereas the radius of the smaller hole defining the cavity ranged from $0.20a$ to $0.23a$. In the four samples, the geometric parameters have slight fluctuations, but the imperfections could be measured by careful SEM characterization and compared to modelling results. Local micro-photoluminescence pumping of the center of the cavity and measuring the luminescence normal to the surface allow us to quickly compare the performance of different cavity designs. The 830nm pump laser light was absorbed by the InAs quantum dots and the wetting layers, and the pump light could be focused onto the sample with a spot diameter of 2 μm. Light emission from the photonic crystal slab surface was then detected by an optical spectrum analyzer. The resolution was varied from 2nm to 0.2 nm, depending on measurements. The peak pumping power was 1.4 mW, which corresponds to a power density of 45 kW/cm^2.

Figure 2.22 shows the p/a dependence of photoluminescence spectrum measured from four cavities with almost identical r/a and r'/a. In this case, we selected a 2 nm bandwidth for the spectrum measurement to detect weak emission from the samples. The shallow donor (D1 and D2) peaks have distinct y- and x-polarizations, respectively. By considering polarization dependence and simulation results, D1 and D2 were found to match numerically predicted shallow donor modes. We believe that the degeneracy of shallow donor modes for $p/a = 0$ is lifted because of fabrication fluctuations in our quantum dot nanocavities. In Figure 2.22, it can be observed that, for $p/a = 0$, only two donor modes are seen, whereas a group of peaks labelled as (X) emerges just above the D2 resonance in cavities with higher p/a asymmetries. All of the peaks shift toward longer wavelengths as p/a increases. However, the shift of the D1 resonance seems to be more pronounced than that of the D2 resonance. This can be understood by assuming that the added edge dislocation overlaps better with the D1 mode than with the D2 mode. This red shift of the D1 mode helps moving the mode energy toward the midgap of the photonic bandgap, resulting in better

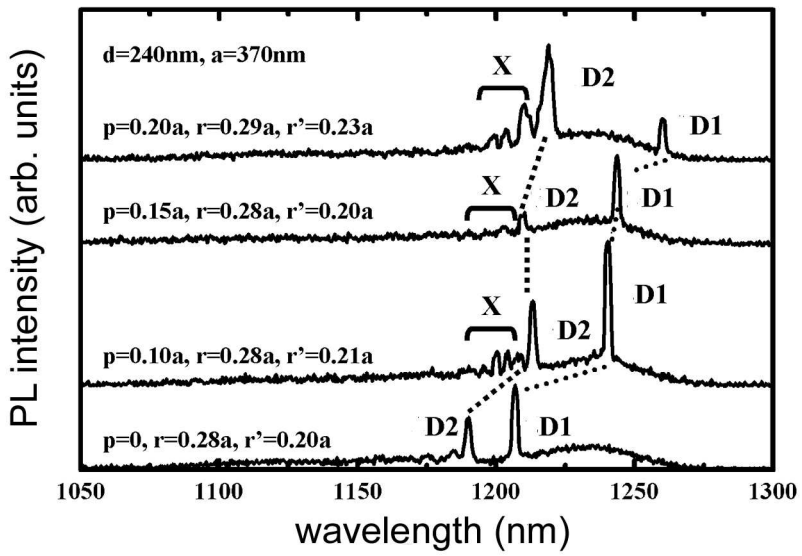

Figure 2.22: PL spectra of samples with different elongation parameter (p/a) ranging from 0 to 0.20.

in-plane confinement of light.

Figure 2.23 shows the influence of p/a asymmetry on the Q factor as well as the normalized resonance energy (a/λ) taken from D1 resonances. The D1 resonance energy monotonically decreases almost linearly as p/a increases for the same reason as described above. Though the shift is small, the D2 frequency dependence also follows the same trend. On the other hand, Q factors continue to increase as p/a increases for this plot. In our samples, a maximum Q factor was obtained at $p/a = 0.20$. A spectrum taken from the nanocavities is shown in Figure 2.24, where the resolution width of the spectrometer was set to 0.2 nm. The measured Q factor was as high as 2800. Therefore, by adding fractional edge dislocation, we could increase the measured Q factor to twice the value measured from a symmetric cavity. To compare the measured Q factor with our simulation results, we have carefully measured the geometries of our fabricated structures, and modelled these with our three-dimensional FDTD code. Indeed, we find that the calculated Q values for our experimentally realized geometries (of 4400) are much closer to the measured values, and that the simulated mode volume is $0.43(\lambda/n)^3$. The Purcell's factor $F_p = 3Q(\lambda/n)^3/(4\pi^2 V)$ is 500, but the maximum field of the mode is positioned at the middle of the center defect in air. The maximum field

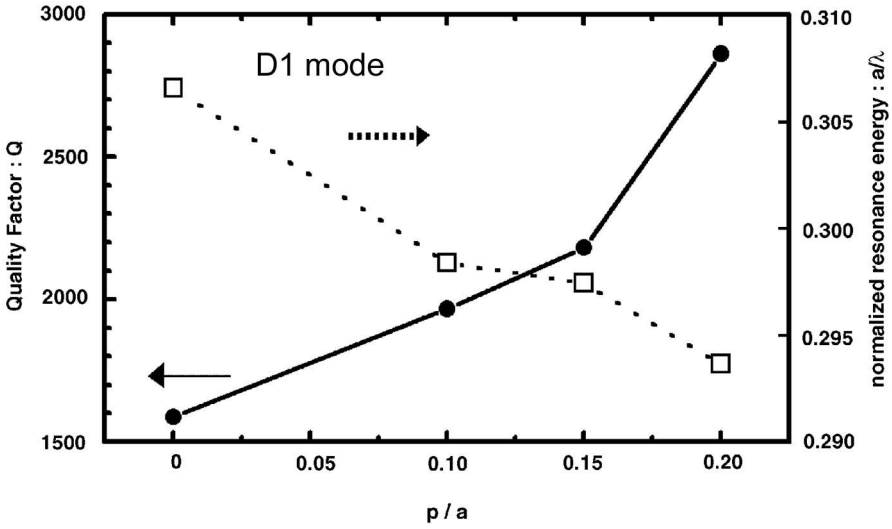

Figure 2.23: Elongation parameter (p/a) dependence of Q and frequency (a/λ). The resonance is D1 mode defined by a fractional edge dislocation cavity.

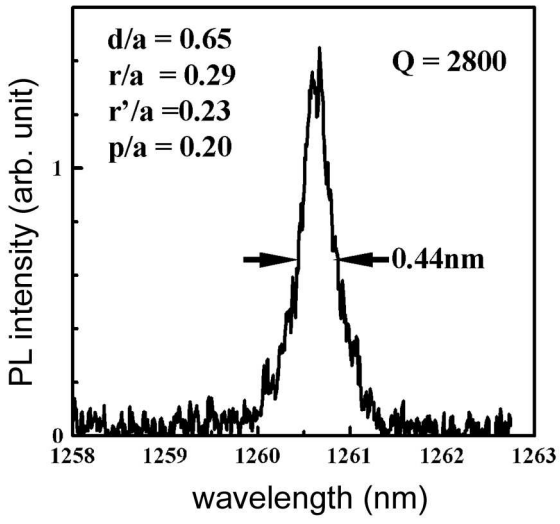

Figure 2.24: PL spectrum of the sample with a Q factor of 2800.

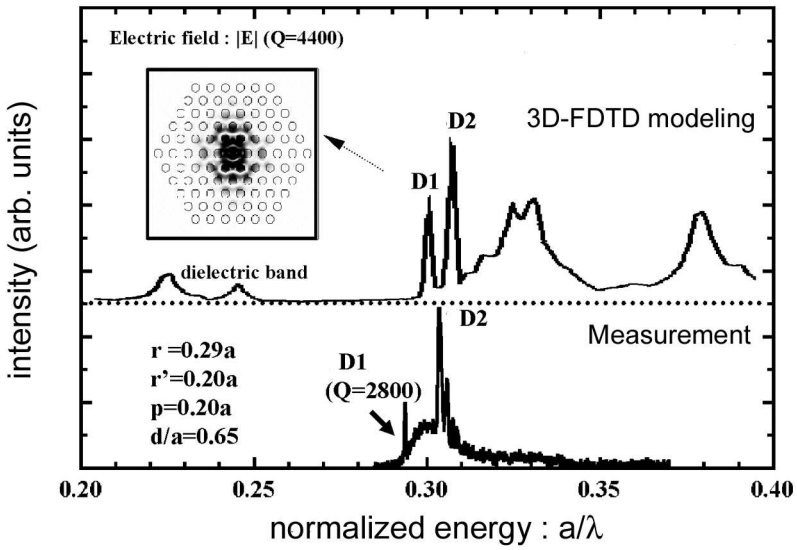

Figure 2.25: Simulated Fourier spectrum of optical modes around a band gap.

in semiconductor is half the maximum field. The possible Purcell factors of this mode is up to 120 in the point within the semiconductor, and the spontaneous emission from the semiconductor can be enhanced on resonance by a factor of up to 120. However, if one prepares an oscillator at the maximum electric field point, the Purcell's factor is indeed 500. In comparison, typical F_p values are a few tens for microdisk cavities.

2.4.3 Verification of high-Q localized modes

To confirm that the measured mode is localized to the defect region, we also altered the spatial location of the pumping position to several points ten lattice layers away from the central hole. We could not see the D1 resonance in such measurements, which leads us to believe that the high-Q donor modes are well confined. This is a strong indicator that the measured cavity mode has both high-Q as well as small mode volume.

In order to verify whether the resonances appear in an appropriate range of emission, we compared the observed spectra with spectra obtained by 3D-FDTD simulations, as shown in Figure 2.25. For the simulation, spectral intensities at several points in the middle of slab were added. Therefore, the spectra reflect on both the confined and propagating modes in the slab while the detected spectra reflect on the leaky part of the modes. That is why we

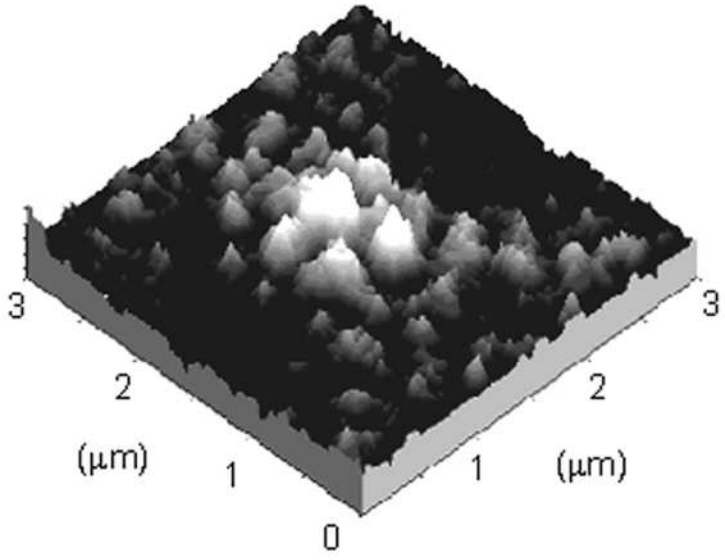

Figure 2.26: Near-field scanning image of localized modes on the slab surface.

also observe inhomogeneous emission from the QD layer in the measured spectra. The D1 and D2 resonance frequencies are very similar to values predicted by the simulation. As the QD emission covers only the D1, D2, and air band region, we did not see any prominent peaks around $a/\lambda = 0.33$, which is shown in the simulated Fourier spectrum. However, we believe those modes do not leak into the air significantly since they are guided modes in the slab and the original intensity of the QD emission in this frequency range is too weak to be observed. Therefore, we conclude that the measured spectra showed a good agreement with the simulated one. Though our predictions indicate that Q values of 30000 are possible in geometries similar to the ones presented here, our measurement results are sufficient to show the advantage of using fractional edge dislocation over conventional designs, and the importance of good cavity designs. We believe it will become feasible to obtain the high-Qs predicted once the optimum photonic crystal parameters are precisely fabricated.

Direct observation of optical mode is attractive, but more difficult because of the diffraction limit of light. Micro-photoluminescence method may be employed to make sure that the mode is small, but cannot display the fine features within the modes, which are seen in our 3D-FDTD simulations. On the other hand, near-field scanning optical microscopy (NSOM) [56] offers a better resolution than the diffraction limit of light (micro-photoluminescence method), and is a useful tool to observe the optical intensity distribution within fabricated

nanophotonic structures [57].

The metal-coated fiber tip with a small aperture size (150 nm) was used to suppress propagating far-field modes, and to pick up more precise profiles of high-Q cavity modes. This way, the signal-to-noise ratio for detecting evanescent waves in a background of propagation waves increases. A 780 nm diode laser was used as CW excitation laser sources through the fiber tip. Photoluminescence (PL) signals were filtered out to remove pump laser signals, and were subsequently detected using a high-gain InGaAs photodiode. The sample was scanned with a piezoelectric stepper motor unit. During the scanning the distance between the fiber tip and the sample was kept constant with an electrical shear-force sensor. The emitted light was collected from a special objective lens above the sample.

The sample used for the NSOM is an InGaAsP quantum well photonic crystal cavity with a fractional edge dislocation. The PC nanocavities fabricated in active InGaAsP material used in this work are very similar to those used to realize low-threshold lasers with low threshold of 220 μW in the design of r'/a=0.18 (r': defect air hole size, a: periodicity of the lattice) [46]. The PC nanocavities have strong high-Q localized modes (D1) and weak low-Q mode (D2) in the QW emission range by micro-photoluminescence. The cavity can get lased under appropriate conditions. We measured Q=2,000 from the high-Q mode (D1). An NSOM image of localized modes in the photonic crystal cavities is shown in Figure 2.26. The bright spot was observed in this image located at the center of the PC structures, matching the positions of the defect cavities. The small spots indicate that, indeed, the modes have small mode volumes as expected from our modeling. Spot size in nanocavity was small and exhibited the high spatially resolved optical mode profile around the center hole. The measured image shows a maximum antinode located at the center of the defect,and six antinodes at hexagonal positions around the center defect. Neither high-Q D1 mode nor low-Q D2 mode excited by the geometry has six antinodes around the center defect, respectively. The measured NSOM images are optical power mapping on the photonic crystal slab. 3D-FDTD modelling was employed to explain this observation. The high-Q and low-Q localized modes are filtered out by the modelling. Under NSOM observations, the sample did not surpass lasing threshold because the NSOM tip excited only a small portion of optical modes and only CW pumping was used. Under such sub-threshold conditions, the photoluminescence mainly shows two high-Q and low-Q modes in the emission range of the broad QW emission. The broad QW emission results from light

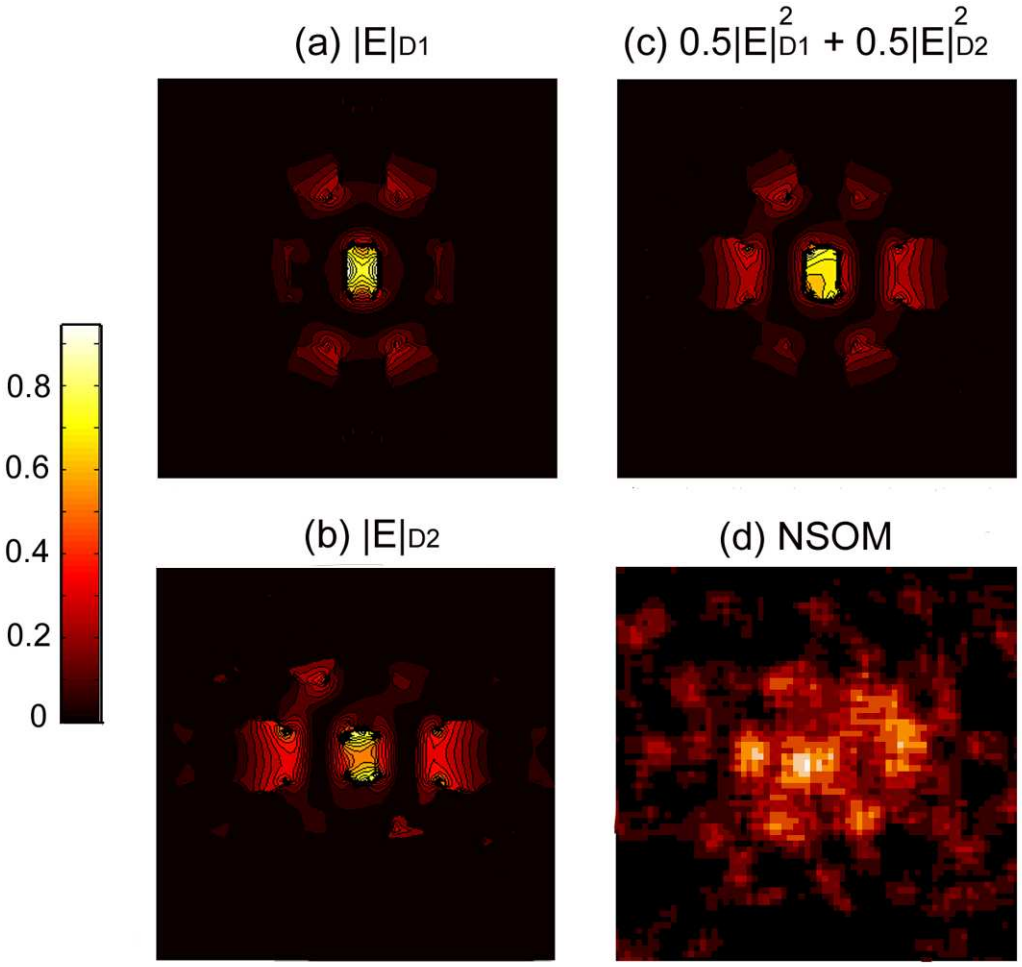

Figure 2.27: (a) and (b) show electric field amplitude mappings of high-Q and low-Q mode in a middle of slab. (c) is squared electric field amplitude $|E|^2$ mapping equally-contributed from the two modes. (d) is a measured NSOM image.

leakage through an escape cone at the air/semiconductor interface, and does not have strong position-dependence. Therefore, the broad emission can be understood as background noise, and the NSOM images should be a superposition of both high-Q and low-Q modes. Figure 2.27 shows electric field amplitude profiles of low-Q D2 and high-Q D1 modes for (a) and (b). The panel (c) shows mapping of $0.5|E_{D1}|^2 + 0.5|E_{D2}|^2$ slightly above the slab/air interface to imitate measurement conditions. The six antinodes are clearly seen in the modelling results. Our observed NSOM image is very similar to predictions from our numerical FDTD simulation, and one can understand that high-Q and low-Q modes are seen together in our measurement and that the modes are indeed localized around the defect.

2.5 Light-Matter Coupling in a Single Quantum Dot Photonic Crystal Cavity System

A single quantum dot in a three-dimensional nanocavity provides the ideal semiconductor system for demonstrating genuine strong coupling. Due to the fermionic nature of quantum dot transitions, it is the true analog of the single-atom/cavity system [39]. In contrast, the strong coupling between a quantum well exciton and the mode of a planar semiconductor microcavity occurs in the nonperturbative regime, corresponding to the many-atom case. The quantum well exciton represents a collection of excited unit cells, and thus compares with the many-atom case; in addition, it also behaves as a boson for weak excitation. In fact, saturation of normal-mode coupling between a quantum well and the mode of a 2 μm-diameter oxide-aperture microcavity requires 300 photons, much greater than the strong-coupling one photon. Genuine strong coupling in semiconductors has not been demonstrated yet. Strong coupling is characterized by the vacuum Rabi splitting $\hbar\omega = 2|\langle \overline{d} \cdot E \rangle|$, where $\overline{d}$ is the dipole moment of the quantum dot and E is the vacuum electric field at the dot location, which must exceed the sum of the decay rates of the cavity and dot polarization. In contrast, weak coupling is manifested by spontaneous emission enhancement for an emitter placed in the field maximum of a cavity. The enhanced spontaneous emission linewidth is $\gamma_{se} = F_p\gamma_0$, where the Purcell factor $F_p = 3Q(\lambda_{cav}/n)^3/(4\pi^2 V_{mode})$ is the vacuum wavelength of the cavity mode, n is the background refractive index of the medium, $Q = \hbar\omega_{cav}/\gamma_{cav}$ is the quality factor of the cavity, and V is the effective mode volume of the cavity. γ_{cav} is the FWHM energy linewidth of the cavity mode, and $\gamma_0/\hbar$

is the cavity-free radiative quantum dot decay rate in the medium. Spontaneous emission enhancement has already been demonstrated in ensemble measurements of quantum dots in a micropillar [25], in a microdisk [23], and in a photonic crystal [30]. However, both regimes, strong and weak coupling, are only extreme cases of the same phenomena, namely the cavity-field/matter interaction. Here we show photoluminescence (PL) experiments of a single InAs quantum dot coupled to a two-dimensional photonic-crystal slab cavity mode in the intermediate regime between weak and strong coupling. The idea of the present experiment is shown in Figure 2.28: in the intermediate-coupling regime for Q increasing towards Q_{split} the eigenenergies of the quantum dot and nanocavity are degenerate and the linewidths approach each other; for $Q > Q_{split}$, the eigen-energies split and the linewidths are equal. Analysis of our dot/nanocavity system shows that our Q results in intermediate coupling.

2.5.1 Sample preparation and experimental technique

The sample was grown on a (001) GaAs substrate by molecular beam epitaxy. On top of a 800 nm $Al_{0.94}Ga_{0.06}As$ layer, a single 30 nm layer of InAs quantum dots was grown between 80 nm $Al_{0.10}Ga_{0.90}As$ layers followed by 40 nm GaAs layers above and below to protect the top and bottom surfaces of the final dielectric slab. The cavity thickness amounts to d = 270 nm, and the quantum dot density is 3×10^{10} dots/cm^2. Several hexagonal-arrayed photonic crystals were fabricated. The cavities are surrounded by fifteen periods of air holes for a good in-plane optical confinement. The lattice spacing a used in this work is lithographically controlled to 360 nm ($d/a = 0.75$). The lithographically written patterns were transferred through the active membrane by using an Ar^+ ion beam assisted with a Cl_2 jet, and the $A_{0.94}Ga_{0.06}As$ layer underneath the cavities was subsequently oxidized in steam to Al_xO_y. Then the Al_xO_y layer was completely dissolved in potassium hydroxide solution, leaving behind a perforated dielectric slab structure surrounded by air above and underneath. Figure 2.29 shows an image taken by scanning electron microscopy of a typical photonic crystal cavity containing a single donor defect. The parameters of the photonic crystal under investigation are: $a = 360$ nm, $r = 0.29a$, $r' = 0.16a$. Here r is the hole radius defining the photonic crystal, whereas r' is the radius of the donor defect in the center of the photonic crystal. Detailed fabrication procedures can be found in the previous section. The PL measurements have been performed in a liquid helium cryostat with temperature

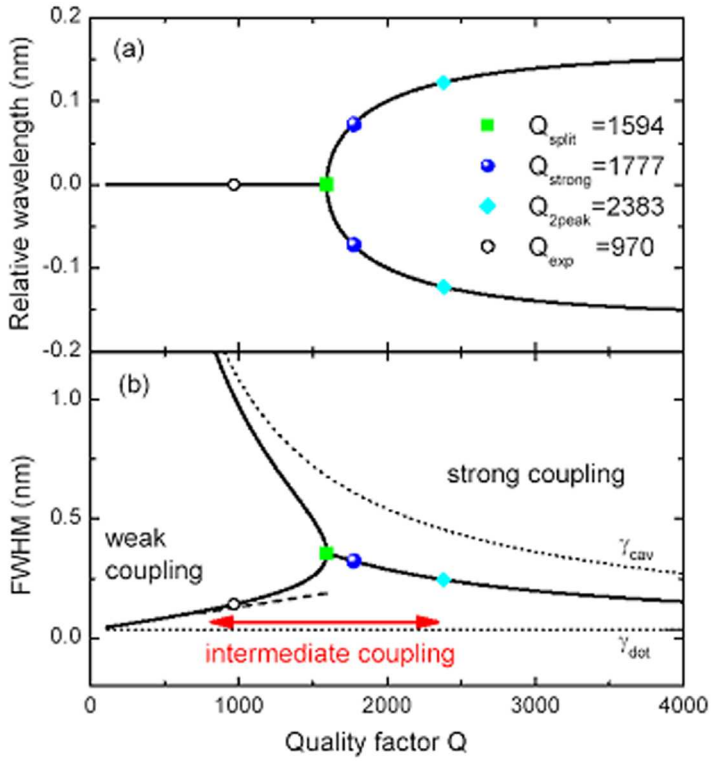

Figure 2.28: Energies (a) and FWHM linewidths (b) calculated using Equation 2.1 for zero detuning. The dashed line in (b) shows the dot linewidth broadened by the enhanced spontaneous emission rate in the weak-coupling regime.

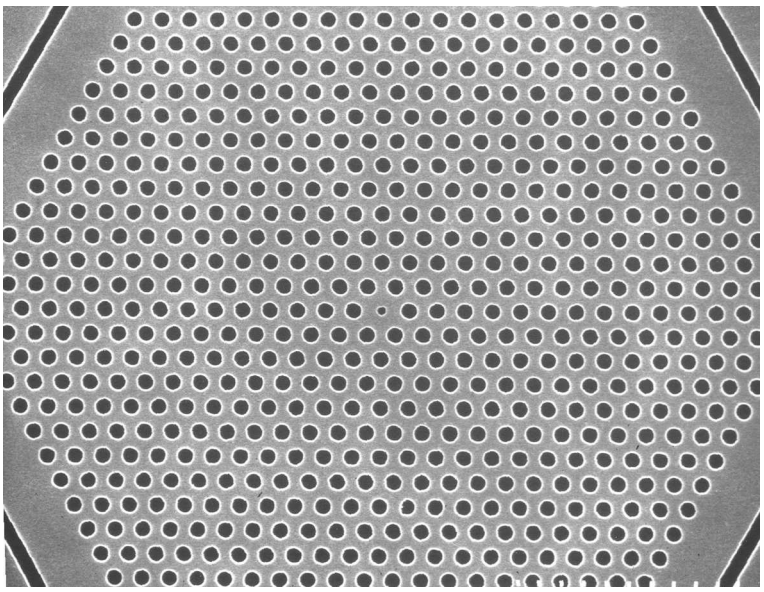

Figure 2.29: Image taken by a scanning electron microscope of a typical photonic crystal cavity containing a single donor defect (r/a=0.29, r'/a=0.16). The photonic crystal cavity supports two orthogonal dipole modes.

control and internal x-y nanopositioner. The samples were optically pumped by the 770 nm output of a Ti:Sapphire CW laser. The pump beam was focused by a 0.5 NA reflecting microscope objective onto the sample resulting in a spot size of 1 μm. The emission from the sample was collected by the same microscope objective, and subsequently analyzed with a spectrometer and detected by a CCD array. In the nonperturbative regime, in-plane emission can be single peaked at the same time that normal emission is double peaked, but not in the strongly coupled regime. Therefore, the quantum dot spectrum can be detected by emission that escapes from the top for internal angles less than the 16^o angle of total internal reflection and by scattering and leakage from the cavity mode. Because temperature shifts the quantum dot resonance faster than the cavity mode, a quantum dot transition can be temperature scanned through the cavity resonance. With the present sample we have found only one case of intermediate coupling: there are only 5-10 quantum dots within the cavity antinodes, and they are spread out spectrally over 100 nm; furthermore there are only a few high-Q nanocavities, and the cavity-dot tuning range is only about 5 nm.

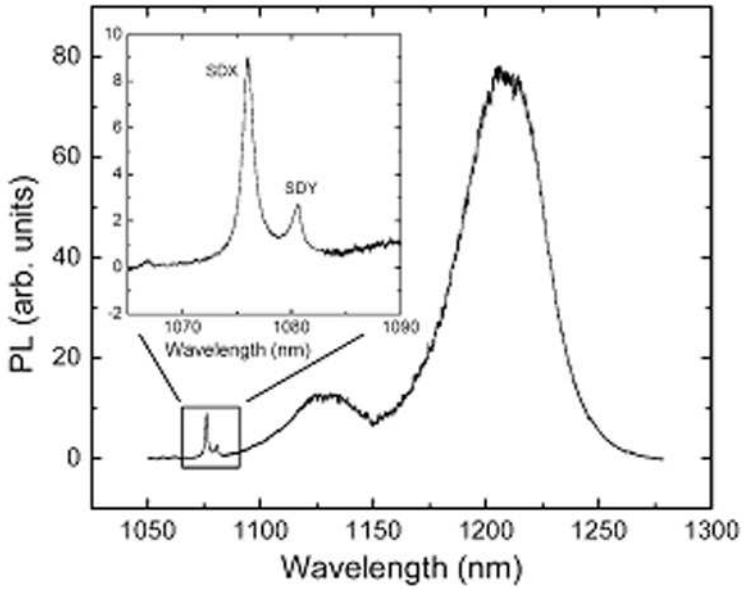

Figure 2.30: Photoluminescence spectrum obtained from the photonic crystal cavity under investigation at a temperature of 20 K and high excitation power density.

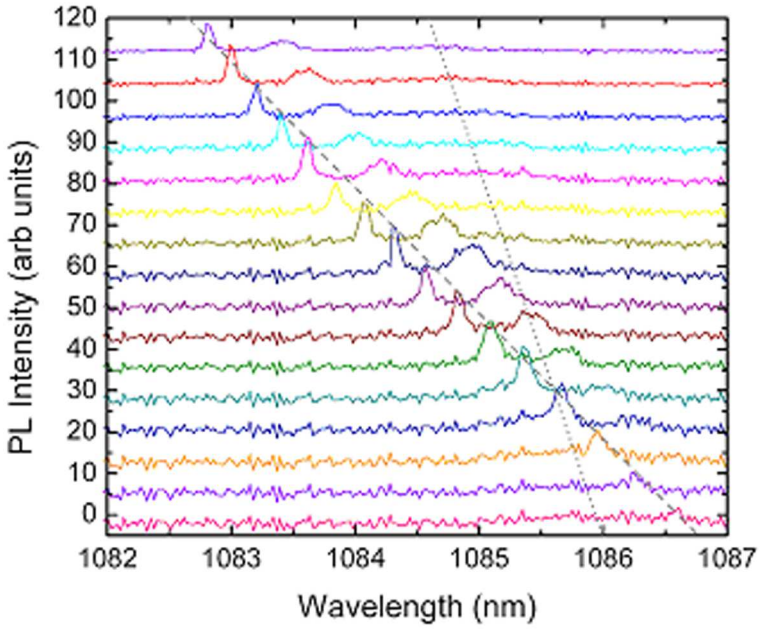

Figure 2.31: Normalized PL spectra for various temperatures for a low excitation power. The temperatures from top to bottom are 42 K to 72 K in steps of 2 K. The dashed line follows the quantum dot, the dotted lines the cavity peak position, which were determined by higher power measurements.

2.5.2 Experimental results

Figure 2.30 shows the PL spectrum obtained from the photonic-crystal cavity under investigation at a temperature of 20 K at high excitation power. The broad background maps the energetic distribution of the dots at the ground (centered around 1210 nm) and the first excited transition (centered around 1130 nm). Two cavity modes are located at the high-energy tail of the first excited transition. They are identified as donor modes, called DX and DY, having distinct x and y polarizations. Both modes can only be observed when pump area and defect area tightly overlap, which leads us to believe that these truly are small volume modes. Using our three-dimensional finite difference time domain (3D-FDTD) code, we find a simulated mode volume $V_{mode} = 0.4 \times (\lambda_{cav}/n)^3$. The FWHM widths of these modes are $\gamma_{cav} = 1.12$ nm (DY) and $\gamma_{cav} = 1.29$ nm (DX) resulting in cavity quality factors of 970 (DY) and 834 (DX); the Q factors are 1100 from our modeling. The degeneracy was lifted due to fabrication fluctuations, but the energy difference between two orthogonal dipole modes is very small ($\Delta(a/\lambda) < 0.002$). The maximum electric field in the semiconductor material is approximately 0.5 times the maximum field of the nanocavity from our 3D-FDTD modeling. In the following we will concentrate on the high-energy cavity mode DY, shifted in wavelength in Figures 2.30 and 2.31 because of temperature and possible spectrometer miscalibration in Figure 2.30. Figure 2.31 shows the PL spectra for various temperatures for a low excitation power. In the vicinity of the cavity resonance, the dot emission is enhanced and broadened. Intermediate coupling is best seen using intermediate powers, where the saturation of uncoupled quantum dot PL helps in the search for coupled QDs. Of course, low powers are best for seeing sharp lines in PL associated with single quantum dot transitions. However, both spontaneous emission enhancement and the cavity resonance are difficult to see in a CW experiment using low power. Enhancing the spontaneous emission rate at low power reduces the lifetime between excitation and photon emission, but it does not increase the number of photons emitted per second. But if the power is increased until an off-resonance (inhibited) quantum dot is well-saturated, *i.e.* the PL is limited by the lifetime and not the pump power, then tuning the quantum dot transition into resonance with the cavity mode reduces the lifetime and increases the PL power. By the same argument, the cavity resonance can be seen more clearly when the power is high enough to saturate the emission from the off-resonance quantum dots. Using this fact, the

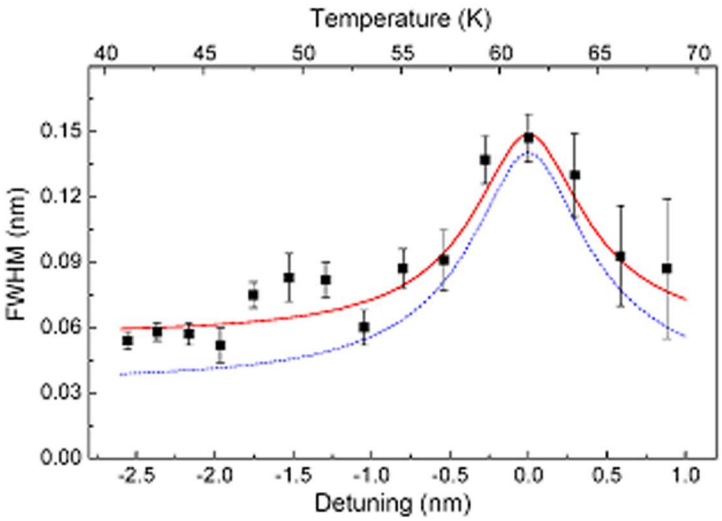

Figure 2.32: FWHM linewidth of the quantum dot (black squares) as a function of the dot-cavity detuning δ compared to calculated linewidths without (dotted line) and with (solid line) convolution with the spectrometer function.

positions of the cavity peak in Figure 2.31 were determined by higher power measurements. Figure 2.32 shows the extracted FWHM linewidth of the quantum dot (black squares) as a function of the wavelength detuning $\delta\lambda = \lambda_{dot} - \lambda_{cav}$. The extracted maximum linewidth amounts to $\gamma' = 0.148$ meV $= 0.141$ nm at resonance. Is this enhanced emission in the weak-coupling regime, or are there clear signatures of intermediate coupling marking the crossover to strong coupling? In next subsection, we use theory to find out the origin of the enhanced emission.

2.5.3 Analysis of the experimental findings and discussion

In order to analyze the experimental findings in greater detail, we use the Jaynes-Cummings Hamiltonian and include the finite dot and cavity linewidths by solving the corresponding master equation for the density matrix of an atom-cavity system [3, 13]. The resulting spontaneous emission spectrum for the dot emission out the top is

$$SE(\omega) = \frac{C}{|\alpha_+ - \alpha_-|^2} \left| \frac{\alpha_+ + \gamma_{cav}/2 + i\delta}{\alpha_+ - i\hbar(\omega - \omega_{dot})} - \frac{\alpha_- + \gamma_{cav}/2 + i\delta}{\alpha_- - i\hbar(\omega - \omega_{dot})} \right|^2 \qquad (2.1)$$

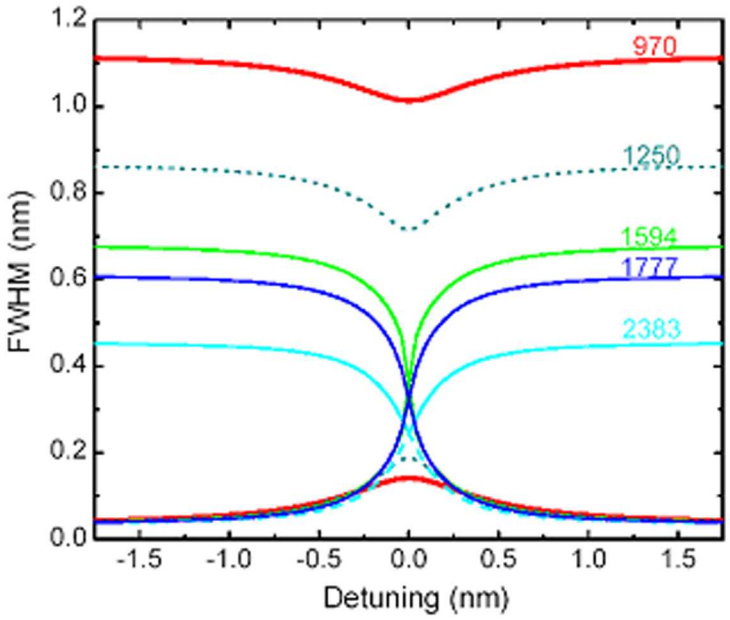

Figure 2.33: FWHM linewidth calculated by using Equation 2.2 as a function of the detuning δ for various cavity quality factors stated in the figure. Q_{exp}=970, Q_{split}=1594, Q_{2peak}=2383.

C is a lengthy normalization constant not shown explicitly here. The complex eigenvalues α_+ and α_- are given by

$$\alpha_{\pm} = -\frac{1}{2}(\frac{\gamma_{dot}}{2} + \frac{\gamma_c av}{2} + i\delta) \pm \frac{1}{2}\sqrt{(\frac{\gamma_{dot}}{2} - \frac{\gamma_{cav}}{2} + i\delta)^2 - 4\hbar^2 g^2} \qquad (2.2)$$

where γ_{dot} and γ_{cav} are the FWHM energy linewidths of the uncoupled dot transition and nanocavity mode, $\delta = \hbar(\omega_{cav} - \omega_{dot})$, and $\hbar g = |\langle \overline{d} \cdot E \rangle|$ is the coupling strength between the dipole moment of the quantum dot and the cavity mode field at the site of the quantum dot. Equation 2.2 contains the eigenenergies and linewidths of the coupled system as shown in Figure 2.28 (a) and (b). Here we treat only the "bad cavity" case for which $\gamma_{cav} \gg \gamma_{dot}$, experimentally verified for our dot/nanocavity. In the weak-coupling limit, $4\hbar g \ll (\gamma_{cav} - \gamma_{dot})$, eqn. 2.1 reduces to a single Lorentzian line when the dot transition and cavity mode are in resonance. The emission spectrum is broadened by the sum of γ_{dot} and γ_{se}, where $\gamma_{se} = 4\hbar^2 g^2/_{cav}$ [3]. In the strong-coupling limit, $2\hbar g \gg (\gamma_{dot} + \gamma_{cav})/2$, the spontaneous emission spectrum in the resonant case becomes a doublet, split by the vacuum Rabi energy $\hbar\Omega_R = 2\hbar g$, with equal linewidths given by $(\gamma_{dot} + \gamma_{cav})/2$ [13]. The intermediate-coupling regime provides a smooth transition from these limiting cases, *i.e.*,

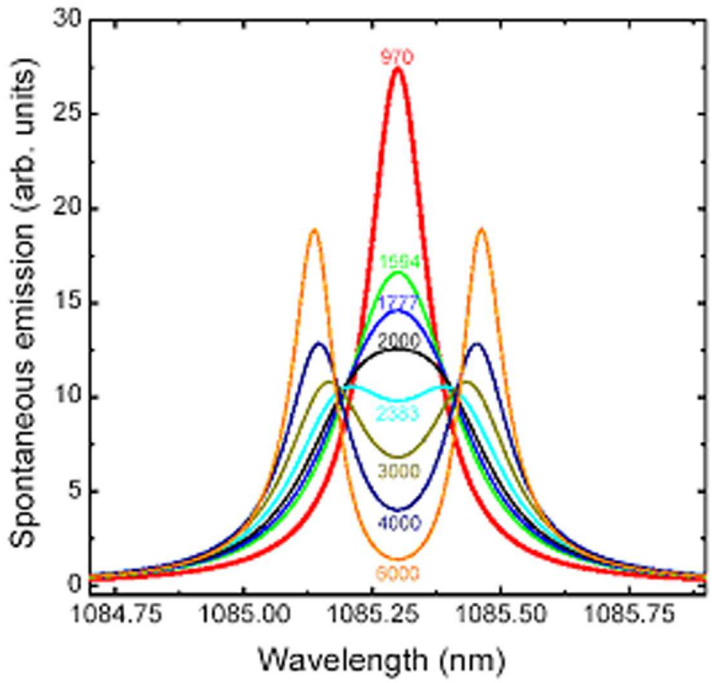

Figure 2.34: FWHM linewidth calculated by using Equation 2.2 as a function of the detuning δ for various cavity quality factors stated in the figure. Q_{exp}=970, Q_{split}=1594, Q_{2peak}=2383.

from a single Lorentzian to double-peaked structure. It is characterized by both a linewidth γ', fulfilling the condition $(\gamma_{dot}+\gamma_{se}) < \gamma" \leq (\gamma_{dot}+\gamma_{cav})/2 \geq \hbar\Omega$, and a lineshape deviating from a Lorentzian. The splitting $\hbar\Omega$ between the eigenenergies drastically increases in the intermediate coupling regime with increasing $Q > Q_{split}$ and approaches $\hbar\Omega_R$ in the strong coupling regime; see Figure 2.28 (a). A similar reduced splitting has been found and investigated for a planar microcavity, when the mirror reflectivity is quite low. Figure 2.28 (b) shows the dot linewidth evolving from the linear onset given by $\gamma_{dot}+\gamma_{se}$ (dotted line) in the weak-coupling regime toward the averaged linewidth in the strong coupling regime. Note that the mathematical transition from degenerate to nondegenerate eigenenergies is given by $2\hbar g = (\gamma_{cav} - \gamma_{dot})/2$, defining Q_{split} in Figure 2.28, and is experimentally determined by the point where the linewidths become equal to each other and to the uncoupled average linewidth. For $Q > Q_{split}$ almost as large as Q_{split}, as the detuning is reduced to zero the cavity linewidth decreases while the dot linewidth increases as indicated by dotted lines in Figure 2.33. For $Q > Q_{split}$ all curves look similar in that the on-resonance linewidths are equal to $[(\gamma_{cav} + \gamma_{dot})/2]$. The corresponding changes in lineshape can be seen in Figure

2.34. The commonly used condition for strong coupling, $2\hbar g \geq (\gamma_{cav}+\gamma_{dot})/2$, also denoted by Q_{strong}, is where the spectrum becomes somewhat flat-topped as shown by the Q_{strong} = 1777 curve in Figure 2.34. Consequently we also show curves for Q_{2peak} = 2383 for the clearly resolved case in Figures 2.28 and 2.33, where Q_{2peak} refers to the condition $\hbar\Omega \geq (\gamma_{cav}+\gamma_{dot})/2$ where $\hbar\Omega$ is the actual splitting and not $2\hbar g$. With increasing Q, the single Lorentzian of the weak-coupling regime evolves through the intermediate-coupling regime into a well-resolved doublet in the strong-coupling regime. After this discussion of the general features of the intermediate-coupling regime, we return to the data in order to show that intermediate coupling has been achieved. We computed spontaneous emission spectra for various detunings, convolved each with the experimental instrument function, and compared the extracted linewidths with the experimental data; see Figure 2.32 dotted and solid curves. The fit using γ_{cav} = 1.18 meV = 1.12 nm yields γ_{dot} = 0.037 meV = 0.035 nm and $\hbar g$ = 0.170 meV = 0.161 nm. These fit values result in the enhanced spontaneous emission linewidth $\gamma_{se} = 4\hbar^2 g^2/\gamma_{cav}$ = 0.098 meV = 0.093 nm, whereas the coupled linewidth is γ' = 0.148 meV = 0.141 nm at resonance. Therefore, γ'= 0.141 nm $> (\gamma_{dot}+\gamma_{se})/2$ = 0.128 nm indicate the onset of intermediate coupling; *i.e.*, the linewidth has begun to increase with Q more rapidly than the linear Purcell enhancement of the weak coupling regime. The thick lines in Figures 2.33 and 2.34 are the linewidth and the on-resonance spectrum for the experimental Q here, namely Q_{exp} = 970.

The analysis to this point has involved only three parameters: γ_{cav}, the FWHM measured uncoupled cavity photoluminescence linewidth, and the two fit parameters for the measured dot linewidth in Figure 2.32, the uncoupled dot linewidth γ_{dot} and the coupling strength $\hbar g$. We now show that the fit value of $\hbar g$ is not unexpected. The maximum value of F_p, given by eqn. 2.1, is 184 assuming the computed mode volume $V_{mode} = 0.4(\lambda_{cav}/n)^3$. But the actual F_p is proportional to $|E|^2$ at the quantum dot, computed to be no more than 0.25 times that at the peak which occurs in the middle of the center hole. This reduces F_p to 46. Then one can use the fact that $\gamma_{se} = F_p\gamma_0 = F_p\hbar/\tau$ = 0.098 meV to extract the lifetime $\tau \leq$ 309 ps as well as the dipole moment $\overline{d}$ = 63 Debye. The latter is a reasonable value for a quantum dot transition, even somewhat large for an excited state transition. A ground state transition of a quantum dot in the field maximum of a Q = 3000 photonic crystal slab nanocavity should exhibit clear strong coupling. That should be achievable, but so far we have failed to resolve ground state transitions in the present quantum dot

samples or to find single quantum dot transitions close enough to couple to photonic crystal modes with Q's approaching 3000.

2.6 Designs of High-Q Planar Photonic Crystal Cavities

In this section, some important design rules are shown. We have seen improvement of quality factors by avoiding an intermixing of TE and TM modes in a cavity and introducing dislocations in the lattice. Even after removing the intermixing, there is no guarantee of getting high-Q planar photonic crystal cavities. Here we take dipole mode and quadrapole mode produced in single-defect square lattice as an example.

High-Q planar photonic crystal cavities have odd symmetry about certain axes of at least one in E_x, E_y, H_x, and H_y. The radiated power within an escape cone in planar photonic crystals [92] is written by

$$P_{rad} = \frac{\sqrt{\frac{\epsilon_0}{\mu_0}}}{4\lambda^2 k^2} \int\int_{k<<k'} dk \left[|F(H_x)|^2 + |F(H_y)|^2 + \frac{\epsilon_0}{\mu_0}|F(E_x)|^2 + \frac{\epsilon_0}{\mu_0}|F(E_y)|^2 \right] \quad (2.3)$$

where

$$F(f(x,y)) = \int\int dxdy \left[f(x,y) e^{i(k_x x + k_y y)} \right] \quad (2.4)$$

It can be seen that the field components with odd symmetry cancels the corresponding Fourier components along the symmetry axis. This way, we can construct high-Q cavity structures. When combined with higher-order modes, photonic crystal cavity modes can have much higher Q factors. For example, one can use dipole modes ($l = 2$) and quadrapole modes ($l = 4$) in planar square lattice. The number l is used to describe the mode. Their magnetic components should be zero at any location of xy plane since the modes are TE modes. Figure 2.35 shows field components (E_x and E_y)in the middle of the slab. Let's look at field components of quadrapole modes shown in Figure 2.35 (c and d). E_x has an odd symmetry about y=0 axis, and E_y has odd symmetry about x=0 axis. On the other hand, for dipole modes shown in panels (a) and (b), E_x component has an odd symmetry about $x, y = 0$ axes. However, E_y component has an even symmetry in all in-plane directions. The vertical quality factors are 74,300 and 1,100 for quadrapole and

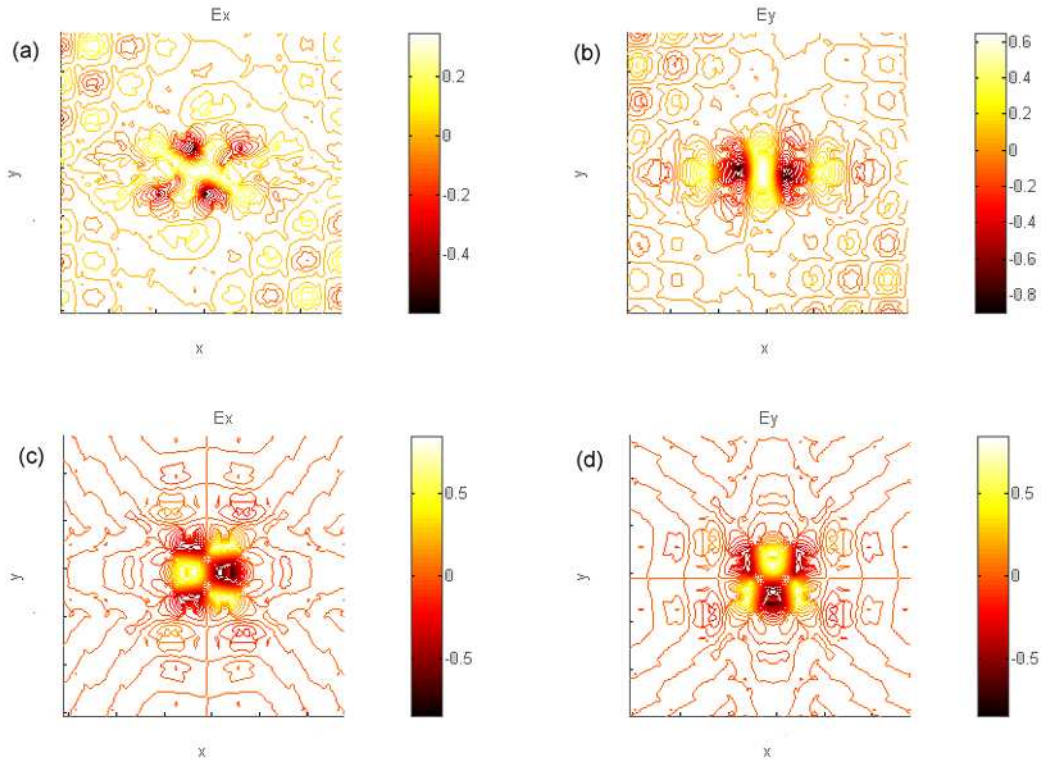

Figure 2.35: Field components (E_x and E_y) distributions of dipole mode (a and b) and quadrapole mode (c and d) created in a single-defect square lattice photonic crystal. The geometric parameters are $r/a = 0.36$, and $d/a = 0.60$.

dipole modes, respectively. The even symmetry of E_y component around the defect is the reason why the dipole mode has significant energy dissipation toward vertical directions. Therefore, choosing a higher number l can enable a cavity to have higher Q factors due to the cancellation of E_x (H_x) and E_y (H_y) at more propagation directions. However, the mode inherently has bigger mode volume since the mode needs the space to accommodate the number of antinodes around the defect region in a $\lambda/2n$ slab. For a quadrapole mode in a square lattice, the mode has l antinodes in one square-shaped round trip, and the volume size is approximately $l \cdot (\lambda/2n)^3$, and proportional to the number l. When the mode does not have good confinement by photonic bandgap, the mode volumes deviate to bigger values. On the other hand, Q factors can increase more rapidly from dipole modes to quadrapole modes. Therefore, choosing a higher l number is desirable for some applications such as strong light-matter coupling, which requires a high Q/V value in the cavity. This odd symmetry method for getting a high-Q cavity is a limitation of planar photonic crystals, and a planar photonic crystal cavity does not have high-Q factors in fundamental modes with as small as $(\lambda/2n)^3$. Multipole cancellation [37] is a similar method used to obtain high-Q optical modes. Three-dimensional photonic crystal cavities [15, 55, 4] are necessary to obtain high-Q fundamental modes.

2.7 Conclusions

InAs quantum dot emission was used for light coupling with a two dimensional photonic crystal nano-cavity with a broken symmetry in z-direction, and was enhanced in the small cavity. Strongly localized deep donor modes were confirmed to have small mode volumes, verified with position-dependent $\mu-$photoluminescence. The x- and y-polarized donor modes could be lithographically tuned over the QD emission range, and Q factors were measured to be as high as 400. Extended modes with Q values of up to 2000 were also measured.

On the other hand, we used improved designs of single-defect nanocavities defined within 2-D photonic crystal slabs with fractional edge dislocations. The mode modulated by the dislocation was found to be well-confined around the single defect as predicted. High quality factors of up to 2800 were measured at room temperature by luminescence from quantum dot emitters at 1.2 microns. These values were higher than the values of 1500 measured for

the simpler symmetric shallow donor mode cavities without the fractional edge dislocation. Our measured Q values were limited by fabrication precision and fine design optimization, and these results indicate that further improvement of Q's is very likely in these kinds of geometries. Near-field scanning optical microscopy is also used to visualize mode profile, and the NSOM image was confirmed to match with a superposition of two modes obtained from our 3D-FDTD modelling.

The onset of intermediate coupling between a single quantum dot transition and the mode of a 2-D photonic-crystal slab nanocavity has been demonstrated. Estimates show that a clear splitting, the ultimate signature for strong coupling, could be observed by tripling the product of the quality factor Q and the dipole moment d.

Finally, design rules for achieving high-Q values in a planar photonic crystal were described. Using odd symmetry in field components, energy loss from a cavity can be suppressed.

Chapter 3

Quantum Dot Photonic Crystal Nanolasers

3.1 Introduction

Simple defect cavity designs allowed the first photonic crystal lasers [42, 59] on InGaAsP multi-quantum well (QW) structures. The Q factors used in the first PC defect nanolasers [59] were less than 100 because the modes had even mirror symmetry of E_x or E_y components about $x = 0$ or $y = 0$ planes, resulting in substantial energy loss inside the light cone [92]. Much effort has been made in order to model photonic crystal systems with, for example, three-dimensional finite difference time domain(3D-FDTD) modelling. After the demonstration of PC lasers, high quality cavity designs of $Q > 10^4$ were presented by means of the modeling [26, 68, 91, 107] to pursue thresholdless lasers [6] and strong light-matter coupling [91].

Quantum dot(QD)-PC lasers, however, have been more difficult devices to construct due to much lower available gain from QDs material. The smaller gain results not only from a lower total volume of actively emitting material but also from variations in spatial locality of QDs as well as inhomogeneous emission broadening consisting of narrow homogeneous broadening. These effects result in a smaller number of QDs contributing to the gain in resonance as the Q factor is increased. First attempts [104, 66] to make QD-PC lasers or to achieve strong light-matter coupling had been made and they showed signatures of QD emission enhancements in PC cavities [104, 66, 69, 30, 86]. However, due to poor Q factors and small available optical gain, simple cavity designs could not make PC modes transparent.

In spite of the difficulties, QD-PC lasers have some advantages as efficient light sources over QW-PC lasers. The main advantage of using quantum dots is to maximize radi-

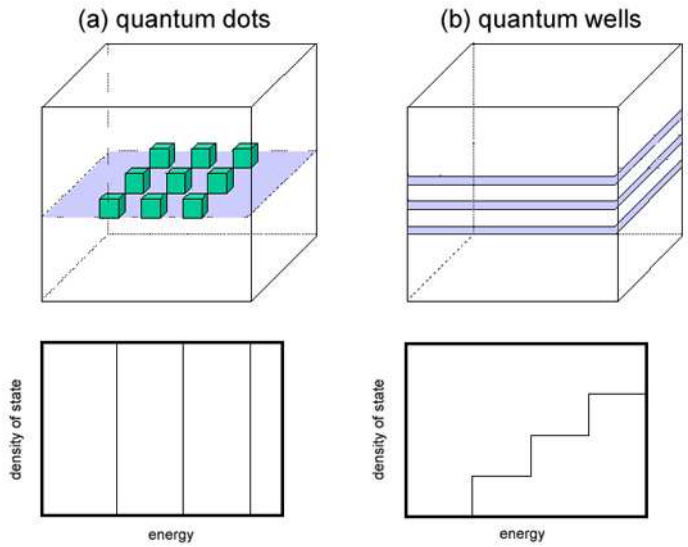

Figure 3.1: Density of state for quantum dots and quantum wells.

ation coupling with a high-Q cavity mode. Single quantum dots have narrow emission linewidth, and are suitable as oscillator in a narrow resonance. Firstly, QDs are expected to have smaller surface recombination rate than QWs, resulting from three-dimensional carrier confinements. To suppress surface recombination is essential in obtaining thresholdless lasers, especially for photonic crystal platforms containing large surface area. The sharp homogeneous broadening emission of each QD can be fitted in high-Q PC resonances. At last, locating single or several QDs at a maximum optical field point in the PC cavity can minimize significant absorption loss by unnecessary active material. In addition, for applications of solid-state quantum information system requiring long coherence time of strong light-matter coupling, self-assembled quantum dots have large dipole moment d_c, resulting in a large interaction constant of single quantum dot with optical field of cavity $g = d_c\sqrt{\hbar\omega/(2\epsilon V_{mode})}$ where ϵ is permittivity of material. Therefore, high Qs and small mode volumes are key to obtaining strong interaction of quantum dot(s) and optical field for applications.

The difficulties have been solved [105, 106] by using high-Q cavity designs with relatively larger mode volumes ranging around $0.7 - 1.2(\lambda/n)^3$. Here designs and fabrications of coupled cavities on square lattice photonic crystal slabs are shown to demonstrate lasing action from such quantum dot photonic crystal cavities. Associated with threshold condition analysis of QD microcavity lasers, we also describe possibilities of single QD-PC lasers.

3.2 Quantum Dot Laser

In 1982, Arakawa and Sakaki [5] proposed the use of quantum dot (box) as a gain source in laser diodes. Current injection QD lasers were reported in 1994 [40]. This electrically-pumped quantum dot lasers showed low threshold of 100 A/cm^2 and high characteristic temperature of $T_0 = (dJ_{th}/dT)^{-1}/J_0$. A quantum dot is a nanostructure, which quantum-mechanically confines electrons and holes in a three-dimensional scale comparable to *de Broglie* wavelength. Because of the quantum effect, allowed states for carriers are discrete, and the corresponding radiation spectrum is also discrete for several of the lowest transitions including the ground state transition. The radiation line is Lorentzian in frequency space. The homogeneous broadening (Lorentzian) is as narrow as 5–10 meV and 10 μeV for self-assembled InGaAs quantum dots at room temperature and 4.2 K, respectively. Figure 3.1 shows discrete density of state in quantum dots. The density of state is described by

$$\frac{dN}{dE} \propto \frac{d}{dE}\Sigma_{E_i<E}\Theta(E-E_i) = \Sigma_{E_i}\delta(E-E_i) \tag{3.1}$$

We can treat quantum dots as Lorentzian-shaped oscillators at optical frequency. Quantum dots are sometimes called artificial atoms because of these features. On the other hand, the density of state of quantum well is step-like, given by

$$\frac{dN}{dE} \propto \frac{d}{dE}\Sigma_{E_i<E}(E-E_i) = \Sigma_{E_i<E}1 \tag{3.2}$$

There are many kinds of quantum dots available, but self-assembled quantum dots are the most important for opto-electronic devices because of their reliability and availability as planar semiconductor material. The reliability is a direct result of crystal quality, and the nonradiative recombination at quantum dot/barrier interfaces should be avoided. Self-assembled quantum dots are grown by the Stranski-Krastanov (SK) mode [43], which uses transition from 2-D to 3-D growth on a stress-induced layer. For example, an InAs wetting layer is grown on a top of GaAs, and after the growth of a few atomic layers, InAs islands are automatically formed to minimize equilibrium energy of the system. Then, a GaAs layer is grown to cap the InAs islands and act as a barrier region for the quantum dots. The typical density of QDs is 10^{10} cm^{-3}. It is challenging to model precise electronic structures for self-assembled quantum dots. One of the best ways to model it is to calculate

electrons n	holes m	carrier density $n_c = (n+m)/2$	absorption	gain	State
0	0	0	1	-1	-
1	0	0.5	0.5	-0.5	-
0	1	0.5	0.5	-0.5	-
1	1	1	0.5	0	X
2	0	1	0	0	-
0	2	1	0	0	-
2	1	1.5	0	0.5	X^-
1	2	1.5	0	0.5	X^+
2	2	2	0	1	XX

Table 3.1: Absorption, gain, and state as a function of carrier occupation. X and XX are exciton and biexciton states.

three-dimensional strain distribution by minimizing formation energy and solve Schrödinger equation in an electronic system with appropriate potential $V(x, y, z)$ modified by strain distribution with a $k \cdot p$ method. This method works by defining specific self-assembled quantum dot structure. Stier *et al.* [83] found wavefunctions for electrons and holes in a InAs/GaAs quantum pyramid dot. Therefore, a good understanding of the structure is essential. Only two carriers can occupy the ground state for electrons and holes, respectively. Table 3.1 shows combination of absorption and gain values for (n,m) of n electrons and m holes in the ground state of a quantum dot [28]. n and m can be 0, 1, or 2. States (n,m)=(2,1), (1,2), and (2,2) can produce gain.

There are several advantages of constructing quantum dot lasers. A big difference between quantum dot and quantum well is the index change dependence on carrier density. The frequency dependence of the change is also much smaller in quantum dots for an ideal case. The ideal case means that inhomogeneous broadening is negligible. The differences result from the fact that a quantum dot is a homogeneously broadened oscillator, while a quantum well is an inhomogeneously broadened oscillator. In quantum well lasers, carrier effects are important in describing the quantum well lasers, and index dependence on carrier density leads to frequency chirps. On the other hand, susceptibility of a single quantum dot as a function of wavelength changes the amplitude, but does not change the shape when carrier density (or inversion population) changes. Therefore, frequency-chirpless laser sources can be constructed by using quantum dot gain material. The chirping restricts transmission distance due to the chromatic dispersion of optical fiber.

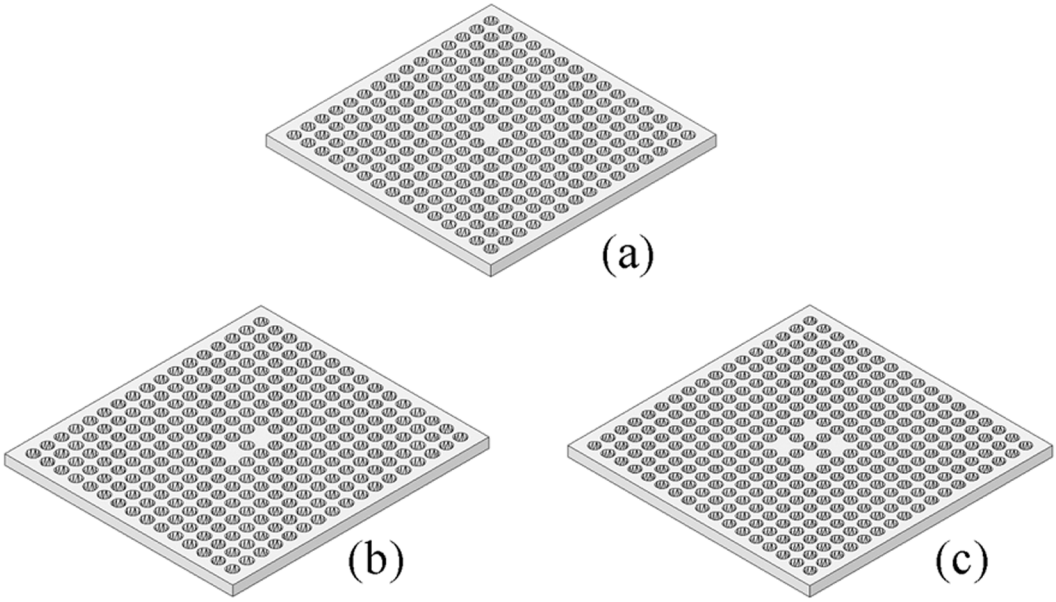

Figure 3.2: Photonic crystal cavities defined by two-dimensional square lattice holes in slab dielectrics. Figure (a) shows single defect cavity. Figures (b) and (c) are two-defect and four defect coupled cavities, respectively.

3.3 Designs of Quantum Dot Photonic Crystal Lasers

3.3.1 Single-defect square-lattice cavity

Single defect square lattice slab cavities have been found to support high-Q quadrapole modes, which can be classified as whispering gallery modes (WGMs) [68]. We started the designing of QD-PC nanolasers from this quadrapole mode. The predicted mode volumes are slightly larger due to the smaller bandgap than the ones for triangular lattices. Less confinement of light in the slab direction leads to more QDs to be included in the mode volume. This eases the difficulty in lasing action resulted from limited gain. Figure 3.2(a) shows a schematic drawing of a single defect cavity defined in two-dimensional square lattice holes. Slab thickness (d) is typically $0.3a$ to $0.8a$, where a is the lattice spacing, designed so as not to support multi-modes in the z-direction. Some assumptions were made to perform our simulation. The imaginary part of susceptibility is neglected. As a result, the analyzed structures are completely passive.

The three field components in the middle slice of slab (a) (E_x, E_y and B_z) are shown in Figure 3.3 (a)-(c). The other components (E_z,B_x,B_y) are negligible for the modes, and the electric field of which is even about the middle of the slab, which is a characteristic

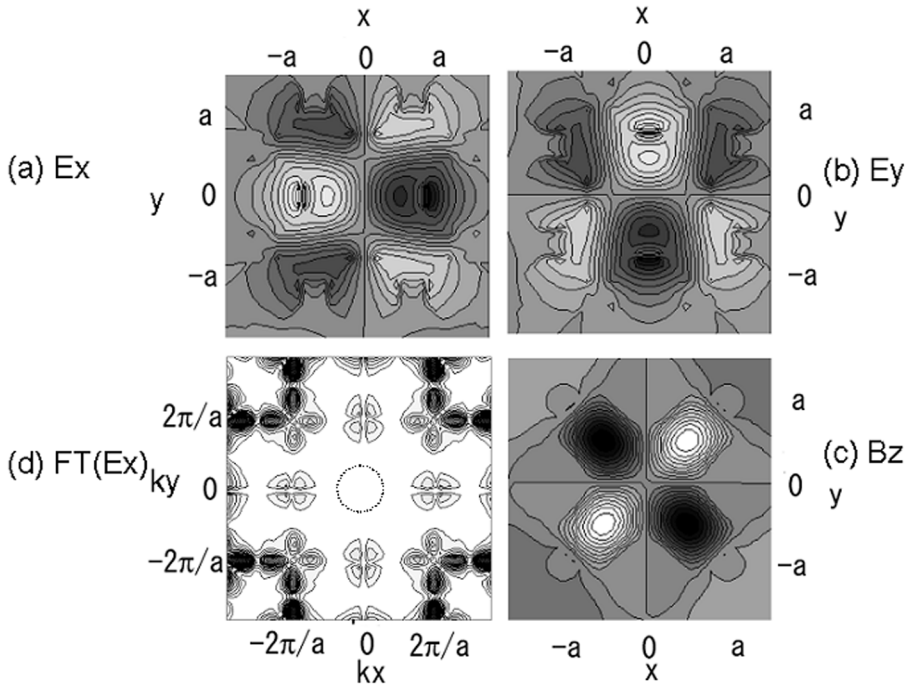

Figure 3.3: Field components mapping over a middle slice of single defect two-dimensional square-lattice for whispering gallery mode. The x- and y-components of electric field and the z-component of magnetic field are shown in (a), (b) and (c). Panel (d) shows Fourier transform of E_x components on a plane $d/4$ above the surface of photonic crystal slab. A circle in the panel (d) represents a light line. A component inside the circle couples with vertical loss of energy from cavities. Total internal reflection on slab surface is main mechanism of vertical confinement. High-Q cavity designs have negligible components inside the circle.

of TE modes. Figure 3.3 (d) shows Fourier transform $FT(E_x)$ of the x-component of the electric field on a plane, which is $d/4$ above the photonic crystal surface [92]. A circle shown about (k_x,k_y)=(0,0) indicates the light line. The component inside the circle is the electromagnetic wave leading to energy dissipation which cannot be suppressed by adding more layers of photonic crystals. The quadrapole modes then have a suppressed damping rate in the vertical direction as shown in Figure 3.3(d).

Figure 3.4 shows calculation results of quadrapole modes excited in a single defect square lattice slab. The mode volumes (V_{mode}), vertical Q factors (Q_v), lateral Q factors ($Q_{\|}$), and total Q factors for seven layers of PCs (Q_t) are shown, as a function of two independent parameters (r/a and d/a) where a, r and d are lattice constant, radius of hole, and slab thickness, respectively. The cavity performances are obtained by 3D-FDTD modelling. The refractive index of the slab and lattice spacing points are 3.4 and 15 in the simulations. It should be noted that for $r/a = 0.32$ the modes have small lateral confinement according to Figure 3.4-(c). For r/a <0.34, the photonic bandgap is partially or completely closed. It is desirable that the modes have complete photonic bandgap toward all in-plane directions in order to increase spontaneous emission coupling (β) factors. Otherwise, β factors are considerably small due to poor coupling of emitter with the mode. To have better radiation coupling of emission with quadrapole modes, r/a values have to be 0.34 or greater. Then Q_t could approach Q_v according to

$$1/Q_t = 1/Q_v + 1/Q_{\|}. \tag{3.3}$$

Figure 3.5 shows the total quality factor approaching the vertical quality factor Q_v as the number of photonic crystal layers (m) increases. Q_v values do not vary significantly when changing the number of layers of photonic crystal around the single defect whereas $Q_{//}$ values increase with an increase in the layer number. When defining many layers of photonic crystal around the defect, cavities show $Q_t \rightarrow Q_v$. This is, of course, true for the quadrapole mode located in the photonic bandgap. This increase is not evidence that modes are confined by complete in-plane bandgap, and calculation of dispersion diagram is helpful for determining the bandgap in all directions.

The maximum Q_v of 97,000 and small mode volume V_{mode} of $0.58(\lambda/n)^3$ are obtained at (r/a,d/a)=(0.34,0.73). V_{mode}s are ranged from 0.4 to $0.6(\lambda/n)^3$ depending on two inde-

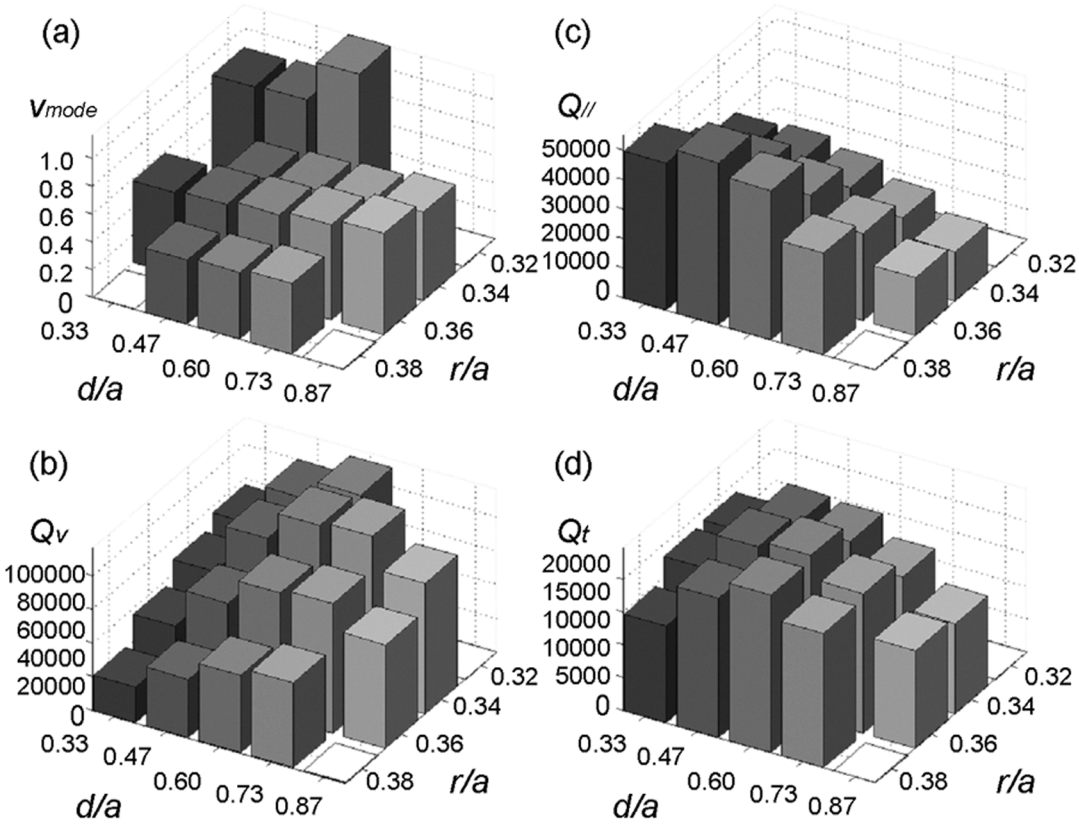

Figure 3.4: Mode volume (a) and Q factors (b,c,d) of single-defect cavity defined by two-dimensional square lattice holes in dielectric slab. V_{mode},Qv,$Q_{//}$ and Q_t are mode volume, vertical Q factor, lateral Q factor, and total Q factor. A unit of mode volume is $(\lambda/n)^3$. Geometric parameters used in this modelling are as follows: a=15, refractive index of dielectric n=3.4 and the number of layers m=7.

pendent parameters but r/a=0.32. The simulated V_{mode} is defined as

$$V_{mode} = \frac{\int \epsilon(r)E(r)^2 dr^3}{\max(\epsilon(r_o)E(r_o)^2)} \tag{3.4}$$

where ϵ(r), $E(r)$ and r_o are permittivity at r, electric field at r and the position giving maximum electric field amplitude.

3.3.2 Coupled cavity design

In order to increase the optical gain of QDs contributing to one mode of our interest, we employed coupled cavity designs [100] based on the quadrapole modes. 3D-FDTD modelling was applied to structures shown in Figure 3.2. Figure 3.2-(b) and (c) are 2D square lattice

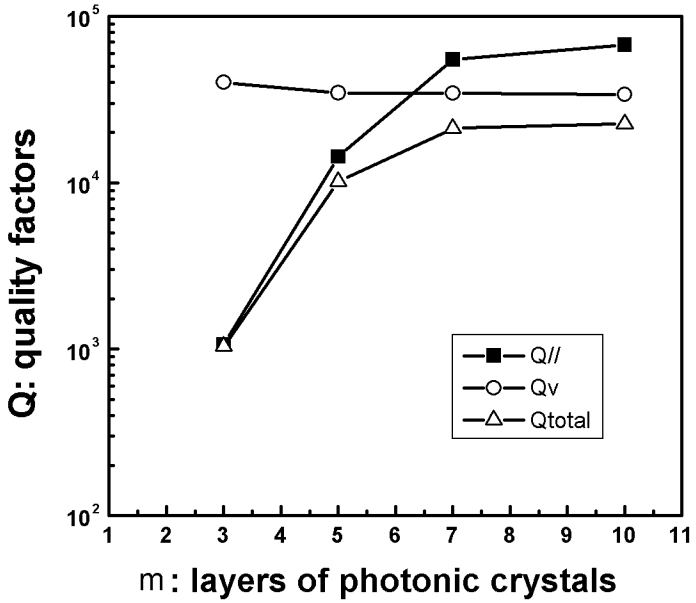

Figure 3.5: Quality factors as a function of the number of square lattice photonic crystal layers around a single defect in a slab. The parameters of photonic crystal are $r/a = 0.38$, $d/a = 0.47$, and refractive index of semiconductor$= 3.4$.

PC slabs with two and four defects, respectively. Identical defects coupled in an optical field lead to the generation of supermodes. Strong interaction of degenerate energy states results in not only the splitting of eigenmode energies but also symmetrically combined eigenmode profiles. New eigenmodes ($\phi(r)$) of connected cavities can be described in a superposition form of each unperturbed cavity mode $\phi_m(r)$ with translation r_m: $\phi(r) = \Sigma_m A_m \phi_m(r - r_m)$ where A_m is independent of the position r. A good index to describe supermodes is the z component of the magnetic field since the magnetic field is purely perpendicular to the slab in the middle of the slab for the quadrapole modes. To obtain supermodes of our two-defect coupled cavity, the z-components of the magnetic field of whispering gallery modes can be used for $\phi_{m=1,2}(r)$. $A_1 = 1/\sqrt{2}$, $A_2 = \pm 1/\sqrt{2}$, $r_1 = (a, 0, 0)$ and $r_2 = (-a, 0, 0)$. The sign of A_2 determines the symmetry of coupled cavity modes.

Figure 3.6 shows three spectra obtained from 3D-FDTD modelling for single-, two-, and four-defect coupled square lattice PC slab cavities. Dashed, solid and dotted lines represent spectra for single-, two- and four-defect coupled cavities. It can be noticed that the quadrapole resonance of a single defect cavity is split symmetrically into two resonances about the quadrapole mode frequency in the spectrum of a two-defect coupled cavity.

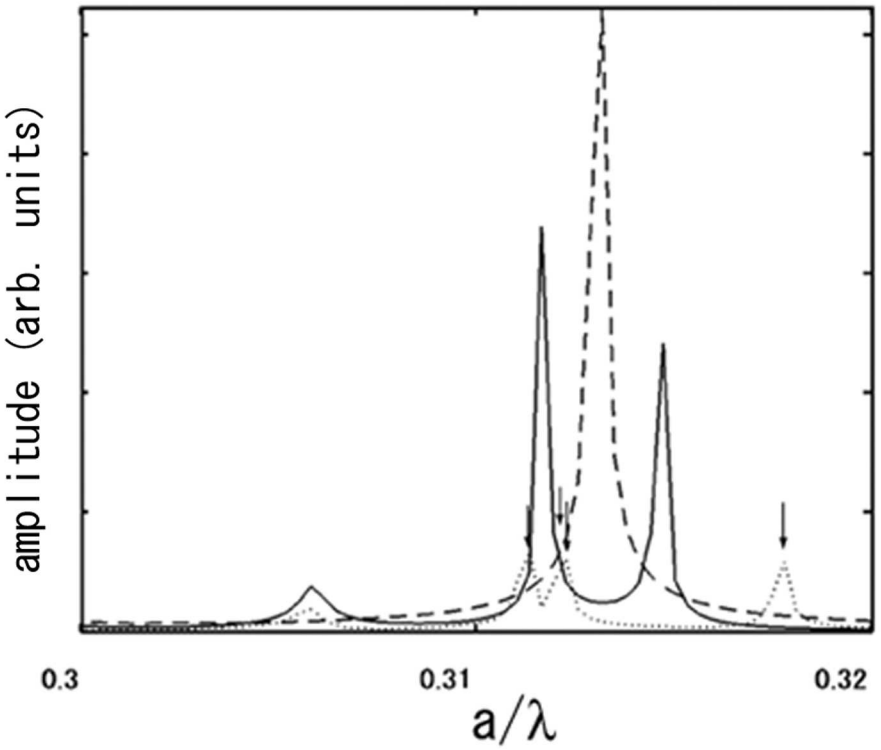

Figure 3.6: Energy spectra of single-defect, two-defect, and four-defect cavity modes. The spectra for single-defect, two-defect, and four-defect cavity modes are shown as dashed, solid and dotted lines, respectively. The spectra were obtained by 3D-FDTD modelling and Fourier-transformation of the time-series data. It can be noticed that the supermode energies are about the original mode energy.

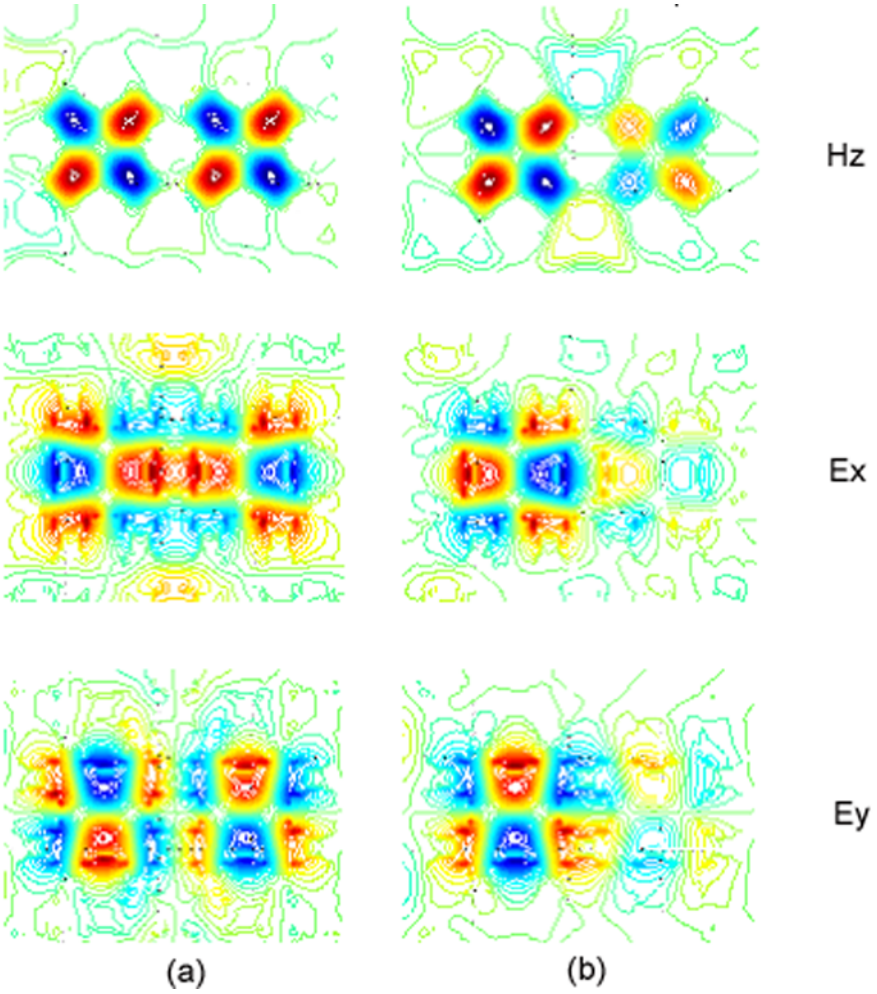

Figure 3.7: (a) and (b) are two supermodes, which are symmetrically combined from two identical quadrapole modes. The structure is a two-defect coupled planar photonic crystal cavity.

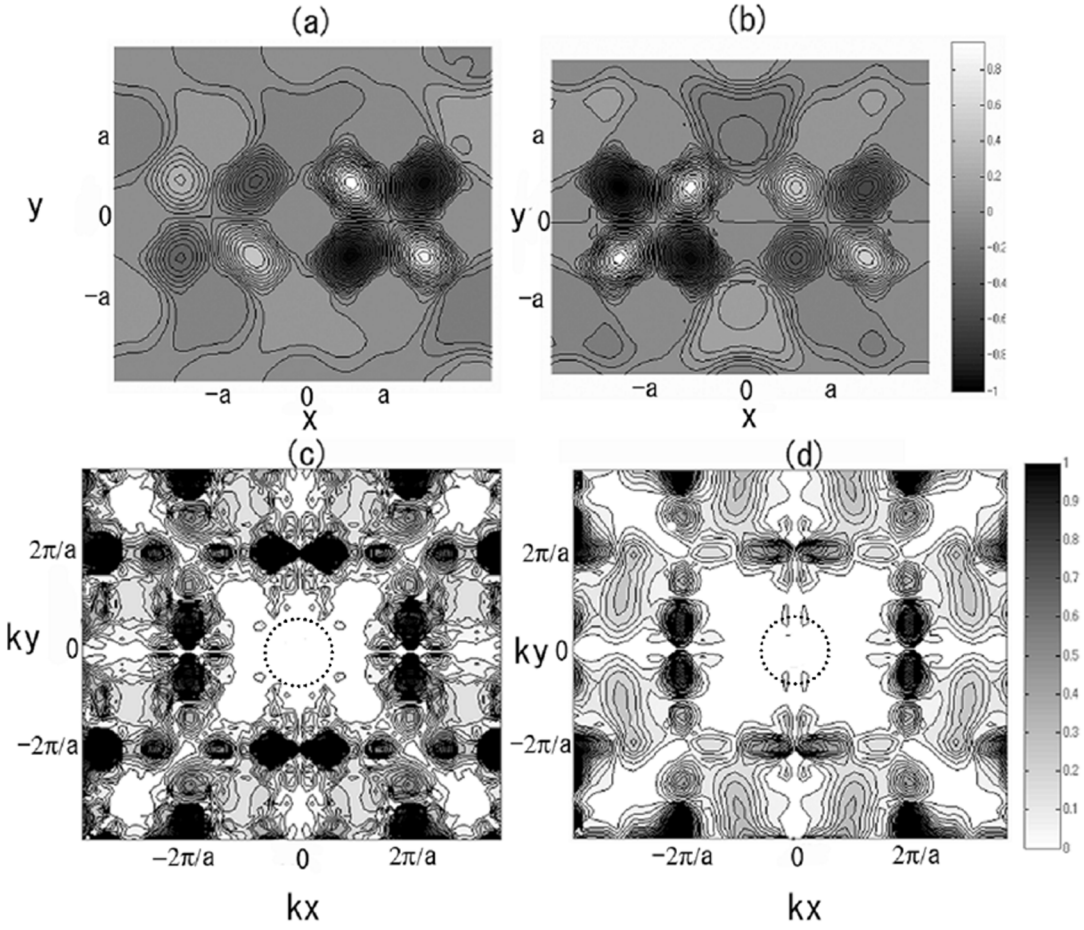

Figure 3.8: Z-component (B_z) of magnetic field mapping on a middle plane of photonic crystal slab for two supermodes are shown in panels (a) and (b). Even mode feature is shown in (a) and odd mode feature is shown in (b). Fourier components of E_x (x-component of electric field) defined by the whispering gallery mode on a plane $d/4$ above a surface of photonic crystal slab. Fig. (c) and (d) show the Fourier components FT(Ex) of even and odd symmetry supermodes obtained from two-defect cavity.

In addition, the two supermode resonances from the two-defect coupled cavity are split symmetrically into four supermodes indicated as arrows in the four-defect coupled cavity spectrum.

Two-defect coupled cavities were analyzed to map field profiles. The analyzed two-defect coupled cavities were located at two lattice constants (a) apart from each other forming one coupled cavity in a 2D-square lattice PC slab with 15 by 17 lattice periods surrounding the cavities as shown in Figure 3.2(b). For example, the modelled photonic crystal slab geometry had a thickness (d) of $0.47a$, hole radii (r) of $0.38a$. Figure 3.7 shows symmetry of H_z, E_x, and E_y components in panels (a) and (b) for odd and even supermodes, respectively. Figure 3.8 (a,b) shows two B_z amplitude profiles in the middle slice of the slab from two combinations of WGMs. You can notice symmetric features of even and odd supermodes from the figures. The electric field is vertical to the hole cylinder axis in the middle of the slab. Figure 3.8(c,d) show Fourier transform mappings of E_x for each supermode. Components in the circles are negligible, showing that the $\overrightarrow{k}$ components toward vertical directions are well-suppressed. Because of these effects, the Q_v factors are still very high. Two defect coupled cavities with (r/a, d/a)=(0.38, 0.47) produce two supermodes. The supermode shown in Figure 3.8 (a) has (Q_v, $Q_{//}$, V_{mode}) = (24000, 16000, $0.67(\lambda/n)^3$) and the odd supermode shown in Figure 3.8 (b) has (Q_v, $Q_{//}$, V_{mode}) = (28400, 16000, $0.67(\lambda/n)^3$) while the original quadrapole modes have (Q_v, $Q_{//}$, V_{mode}) = (34500, 55000, $0.4(\lambda/n)^3$). The values are obtained for seven layers of photonic crystals around defects. This way, two-defect coupled cavities increase the mode volume by 10-50% and we can generate high-Q supermodes by coupled cavities with a decrease in the Q factors. For now, this decrease in Q factors is not a problem since the Q factors of the fabricated structures are still affected by other factors such as fabrication imperfection and significant internal loss. By putting the defects farther away from each other, the high-Q factors of single defect mode can be preserved on coupled cavities with much smaller interaction of modes and the mode volume approaches twice the size of a single defect cavity quadrapole mode. The frequency separation of supermodes would be decreased as the interacted fields decrease. Supermodes can be used for optical switches and lasers with more distributed mode profiles as well.

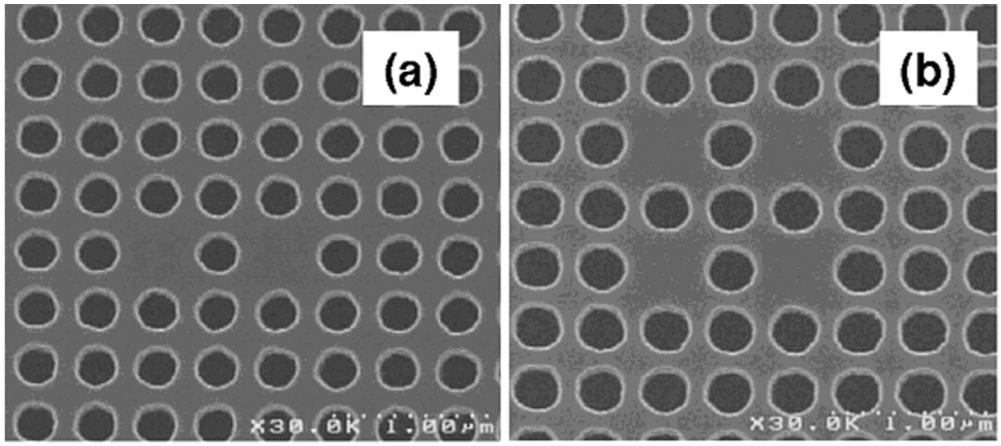

Figure 3.9: Scanning electron microscopy images of two- and four-defect coupled cavity defined in two-dimensional square lattice holes. The cavities support supermodes originating from quadrapole modes.

3.4 Sample Preparation of Quantum Dot Photonic Crystal Lasers

Five stacked self-assembled InAs QDs layers were grown by molecular beam epitaxy. The QD density is 1×10^{10} /cm^2·layer. Therefore, five hundred QDs exist in a $1\times1\mu m^2$ area before fabricating holes. 30 nm GaAs layers as quantum dot barriers separated the QD layers. $Al_{0.2}Ga_{0.8}As$ is used for cladding layers to form thin slab waveguides, which are deposited on an 800nm $Al_{0.94}Ga_{0.06}As$ sacrificial layer on top of the GaAs substrate. 170–200 nm Polymethyl methacrylate (PMMA) resist layer was coated on the surface of samples containing QDs layers, and patterns were then defined by electron-beam lithography. Chlorine-based chemically assisted ion-beam etching was used to transfer the beamwritten patterns into the $Al_{0.94}Ga_{0.06}As$ sacrificial layer through the QD layers. After the removal of PMMA left on the surface, the $Al_{0.94}Ga_{0.06}As$ layer was oxidized in the furnace with hot water vapor. Then, wet etching of aluminium oxide layer was performed with potassium peroxide aqueous form and hydrochloric acid. Many geometries of single-, two-, and four-defect coupled cavities were fabricated within the photonic crystals with lattice sizes of 31 by 31, 31 by 33, and 33 by 33, respectively. Figure 3.9 shows scanning electron microscope images of two-defect and four-defect coupled cavities.

In order to confirm quadrapole modes, photoluminescence measurements were performed at room temperature. Figure 3.10 shows typical photoluminescense spectra for single-defect, two-defect, and four-defect cavities in a square lattice of holes. As one expects, a quadrapole

Material	Function	Doping [cm^{-3}]	Thickness [nm]	QD Density [/cm^2·layer]
p-GaAs:Be	cap layer	4×10^{17}	10	
p-$Al_{0.16}Ga_{0.84}As$:Be	carrier confinement	4×10^{17}	25	
i-GaAs	barrier	undoped	25	
i-InAs QDs	Active region	undoped	5	1×10^{10}
i-GaAs	barrier	undoped	25	
i-InAs QDs	Active region	undoped	5	1×10^{10}
i-GaAs	barrier	undoped	25	
i-InAs QDs	Active region	undoped	5	1×10^{10}
i-GaAs	barrier	undoped	25	
i-InAs QDs	Active region	undoped	5	1×10^{10}
i-GaAs	barrier	undoped	25	
i-InAs QDs	Active region	undoped	5	1×10^{10}
i-GaAs	barrier	undoped	25	
n-$Al_{0.16}Ga_{0.84}As$:Si	carrier confinement	1×10^{17}	25	
n-GaAs:Si	-	1×10^{17}	10	
n-$Al_{0.94}Ga_{0.06}As$:Si	sacrificial layer	1×10^{18}	800	
n-GaAs	substrate	1×10^{18}		

Table 3.2: Layer structure of quantum dot photonic crystal lasers

mode is seen in a single defect cavity (Figure 3.10 (a)). The measured wavelength matches with one obtained by our modelling, and observed $\lambda/\Delta\lambda$ values are around 2000. Peaks D are dipole modes, and measured $\lambda/\Delta\lambda$ values range from 500 to 1000, which are smaller than the ones for quadrapole modes. For coupled cavities, supermodes are always observed with splitting. The differences of Q factors and resonance frequencies help one distinguish a quadrapole mode from a dipole mode.

3.5 Laser Characterization

A pulsed 780 nm semiconductor laser diode was used to measure luminescence spectra and peak collected resonance power (L_{out}) as a function of peak pump power (L_{pump}). Twenty nanosecond pulses with 2.86% duty cycle were applied to the pumping laser diodes. The pump light was confirmed to have a good pulse shape in the time domain. The pumping beam diameter was varied up to 4 μm.

Figure 3.11 shows two L-L curves taken from two- and four-defect coupled cavities. Each of these cavities exhibits distinct threshold and linear increase in output power above threshold. Threshold pump powers of 120 μW and 370 μW are measured for two- and

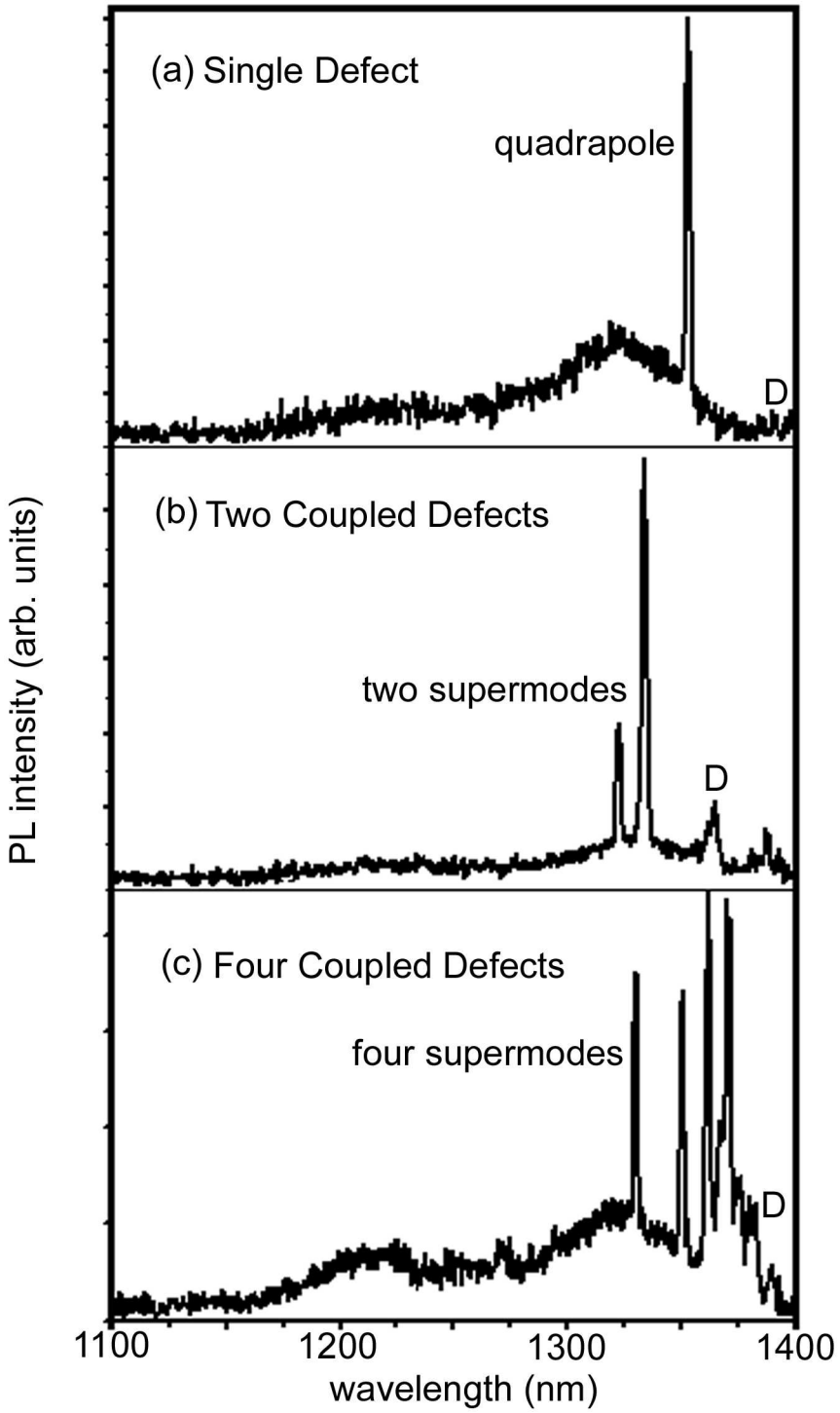

Figure 3.10: Panels (a), (b), and (c) show typical photoluminescence (PL) of single-, two-defect, and four-defect cavities at room temperature. CW Pumping power is 1 mW, and the pumping spot size is around four μm. Peaks D are dipole modes excited in square lattice defect cavities.

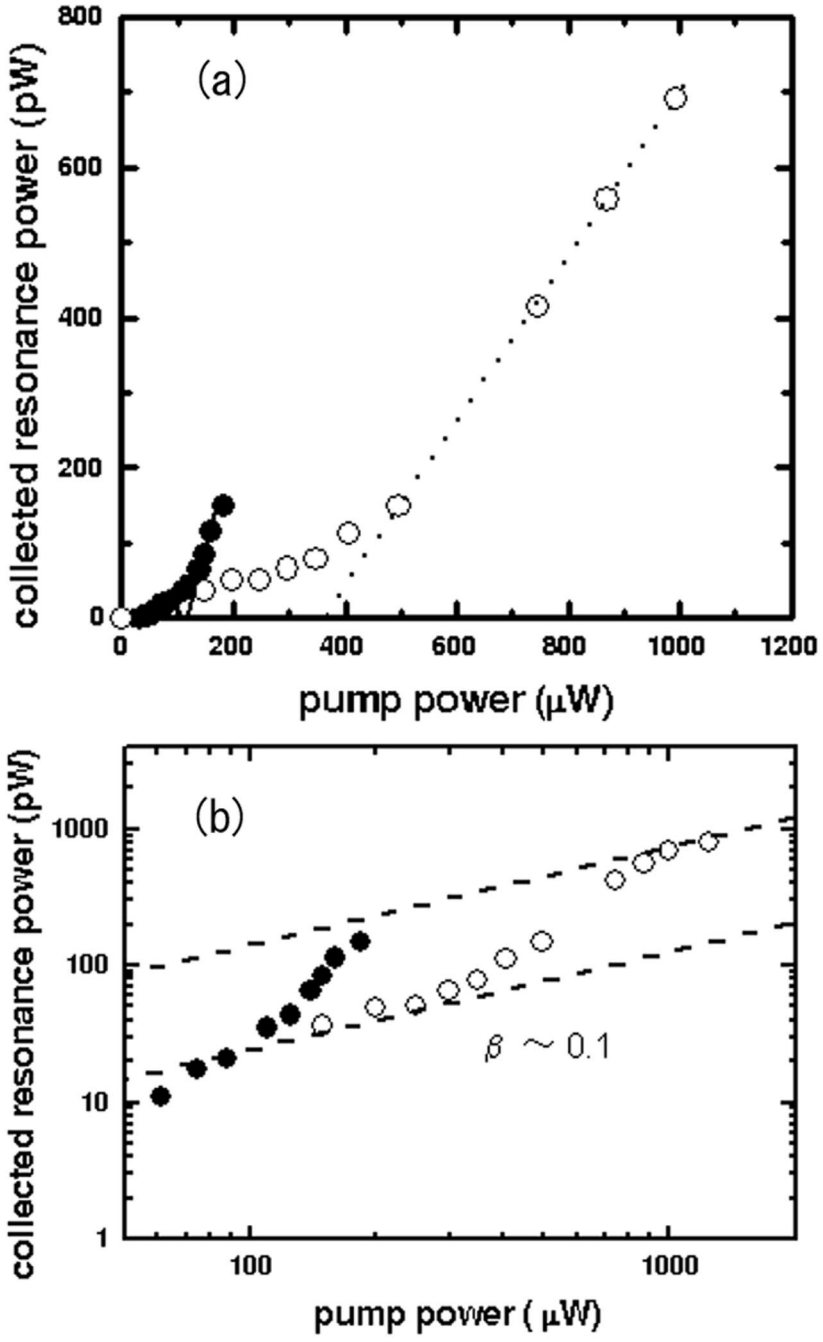

Figure 3.11: Collected peak output power of nanolasers as a function of input peak pump power. Black and white circles are take from two-defect and four-defect coupled cavities, respectively. Panel (a) is a linear-linear graph, and (b) is a log-log graph to show approximate β factors. The duty cycle is 3%, and the pulse width is 20 nanoseconds. The measurements were conducted at room temperature. The r/a s are 0.34 and 0.38, and as are 400 nm and 420 nm for two- and four-defect coupled cavities, respectively. d is 200 nm.

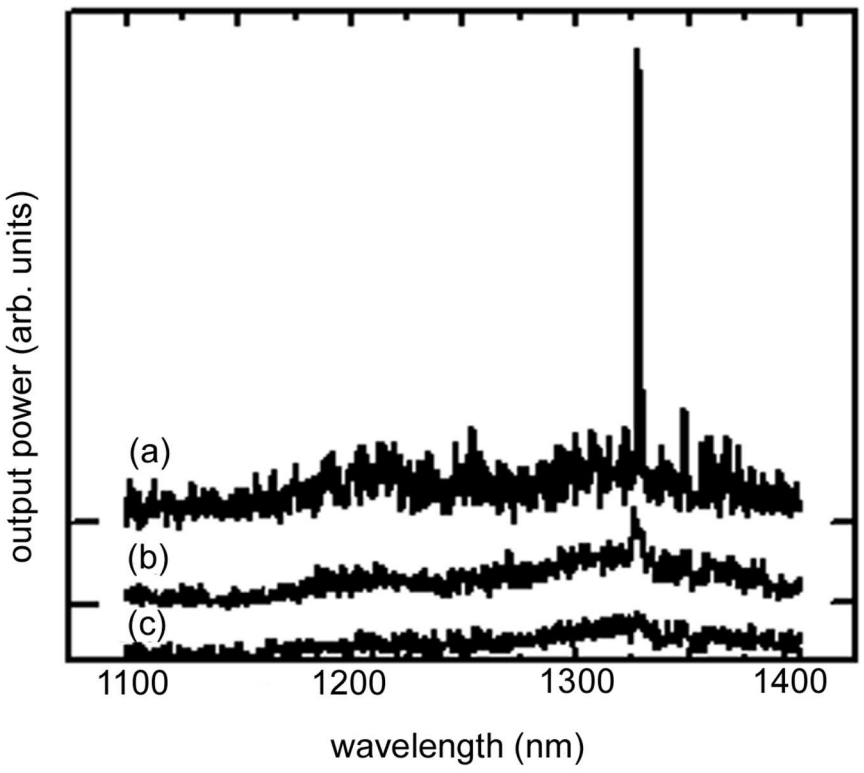

Figure 3.12: Spectra taken at three pump power levels for four-defect coupled cavity. The duty cycle is 3%, and the pulse width is 20nanoseconds. The measurements were conducted at room temperature. (a) 140 μW, (b) 250 μW, (c) 990 μW.

four-defect coupled cavities, respectively. Considering filling factors and transmission of pump light at the air/semiconductor interfaces, the pump light power in the membranes would be approximately only 15% of the incident pump power with perfect absorption by material. Fifteen percentages of threshold incident pump powers are 18 μW and 56 μW for two-defect and four-defect coupled cavities, respectively. Actual absorbed pump power would be smaller than this estimation due to imperfect absorption. 1 μm or thicker AlGaAs layer is necessary to absorb all pumping power. These facts allow us to believe that our nanolasers are operated at very small power and that sub-μW threshold lasers could be constructed by improvement of fabrication. In addition, it should be noted that our lasers show soft-threshold in Figure 3.11(a), and Figure 3.11(b) shows β factors $\sim$ 0.1, for four-defect coupled cavities, where β factor is a ratio of spontaneous emission rate into the single laser mode to total spontaneous emission rate. Two defect coupled cavities show softer threshold curve. The rough estimate of the β factor is $\sim$0.3, which means that the spontaneous emission is efficiently coupled with lasing modes.

Figure 3.12 shows luminescence spectra from a four-defect coupled cavity. Below threshold (Figure 3.12 (a)), the resonance cannot be clearly observed. Close to threshold, nonlinear amplification of emission (soft threshold) is seen (Figure 3.12 (b)). Above threshold (Figure 3.12 (c)), the resonance intensity increases significantly. The lasing wavelength of 1328nm matches the QDs ground state emission. The lasing frequency of a/λ=0.316 in this laser also matches the analyzed mode frequency of four-defect coupled cavities. Spectral line widths decreased from 1–2 nm (below threshold) to less than 0.2 nm (above threshold). With moderate CW pumping, the resonance showed $\lambda/\Delta\lambda = 2100$. The combination of distinct threshold in the L_{pump}-L_{out} curves and line width narrowing indicate that the cavities are definitely lasing. For two-defect coupled cavities, the resonance was measured at a/λ=0.3. The simulated mode volumes are $0.8(\lambda/n)^3$ and $1\times(\lambda/n)^3$, respectively, by using geometric parameters of lased PC samples. We also measured single defect cavity, and it showed much larger output power than non-lasing samples. However, due to the short lifetime, we could not confirm the narrowing of the mode as the pumping power increases.

3.6 Discussion

3.6.1 The number of QDs in lasing modes

The approximate number of QDs contributing to lasing is calculated in this section. The formula is derived by starting from the threshold condition shown in reference [100] with an assumption that material permittivity $\epsilon(r)$ is almost uniform. This assumption seems to contradict with photonic crystals, but it is a good approximation for obtaining an approximate point of threshold. In addition, the assumption is also valid in our structures, in which all gain material is located in the photonic crystal slab, *i.e.*, $\epsilon(r)$ = constant for all gain material. Then, we start from the threshold condition for the normal mode $E_l(\overrightarrow{r})$ as follows [100]:

$$\left(\omega_l^2 - \omega^2\right) + i\frac{\sigma\omega}{\epsilon} = \frac{\omega^2\epsilon_0 f}{\epsilon}\left(\chi^{'} - i\chi^{''}\right) \tag{3.5}$$

$$\int_V dr^3 E_l\left(\overrightarrow{r}\right) \cdot E_l\left(\overrightarrow{r}\right) = 1 \tag{3.6}$$

$$f = \int_{V_{active}} dr^3 E_l\left(\overrightarrow{r}\right) \cdot E_l\left(\overrightarrow{r}\right) \tag{3.7}$$

where $\omega = 2\pi\nu$, $\omega_l = 2\pi\nu_l$, $\sigma = \epsilon\omega/Q$, $\chi = \chi' - i\chi''$ are lasing angular frequency, resonance angular frequency, conductivity and complex susceptibility. V_{active} is the volume where gain or loss is generated in the mode of interest.

Equation 3.5 gives the threshold condition containing Q factor and the lasing wavelength at threshold, and the lasing wavelength condition. The imaginary part of susceptibility is given by

$$\chi^{''} = \frac{\mu^2}{2\epsilon_0\hbar}\Delta N \frac{\Delta\nu/2\pi}{\left(\nu - \nu_i\right)^2 + \left(\frac{\Delta\nu}{2}\right)^2} \tag{3.8}$$

where ϵ_0 and ΔN are permittivity in vacuum and the population inversion number per unit volume. Equation 3.8 shows Lorentzian-shaped homogenous broadening representing gain or loss from a single quantum dot.

After plugging Equation 3.8 into the imaginary part of Equation 3.5, the following threshold condition is derived for a single quantum dot

$$\frac{\omega_l}{Q} = \sum_{m=1}^{M} \frac{g\omega\mu_m^2\Delta\rho_m}{2\varepsilon V_o C_q} \frac{\hbar\Delta\omega_m}{(\hbar\omega - \hbar\omega_m)^2 + (\frac{\hbar\Delta\omega_{i,m}}{2})^2} \tag{3.9}$$

and for N quantum dots

$$\frac{\omega_l}{Q} = \sum_{i=1}^{N}\sum_{m=1}^{M} \frac{g_i \omega \mu_{i,m}^2 \Delta\rho_{i,m}}{2\varepsilon V_o C_q} \frac{\hbar\Delta\omega_{i,m}}{(\hbar\omega - \hbar\omega_{i,m})^2 + (\frac{\hbar\Delta\omega_{i,m}}{2})^2} \tag{3.10}$$

where

$$\frac{1}{C_q} = \frac{|E_l(\overrightarrow{r}) \cdot E_l(\overrightarrow{r})|}{\max\left[E_l(\overrightarrow{r}) \cdot E_l(\overrightarrow{r})\right]} \tag{3.11}$$

$$V_o = \frac{\int_V dr^3 E_l\left(\overrightarrow{r}\right) \cdot E_l\left(\overrightarrow{r}\right)}{\max[E_l\left(\overrightarrow{r}\right) \cdot E_l\left(\overrightarrow{r}\right)]} \tag{3.12}$$

g and $\Delta\rho$ are degeneracy of states and inversion factor of the transition. $\omega \simeq \omega_l$ was also assumed because of the following condition explaining the frequency pulling of lasers.

$$\omega = \frac{\omega_l}{\sqrt{1 + \frac{\epsilon_0 f}{\epsilon}\chi'}} \simeq \omega_l \left(1 - \frac{\epsilon_0 f}{2\epsilon}\chi'\right) \tag{3.13}$$

Equation 3.10 can treat gain and loss contributed from all the quantum dots, depending on the location. If we know information such as homogeneous broadening, center wavelength for gain spectra, and dipole moments, quality factors can be numerically obtained for reaching the threshold condition. For simplicity, some additional conditions are applied to QD systems. We define the effective number of QDs (N_{lasing}) to obtain lasing action as the number of QDs located at maximum electric field, i.e., $C_q = 1$. In order to obtain N_{lasing} for our lasers, we assumed conditions such as $\Delta\rho = 1$,$\epsilon = 3.4^2\epsilon_o$,$V_o = C(\lambda/n)^3$, and squared QD dipole moment $\mu^2 = 1 \times 10^{-56}[\mathrm{C}^2{\cdot}\mathrm{m}^2]$ [22]. Next, approximation was applied to the problem. We randomly selected the energy of each quantum dot in a Gaussian distribution by a computer, representing inhomogeneous broadening. In the calculations, inhomogeneous broadening of 40 meV is used. This way, we can simulate the number of quantum dots making a cavity transparent. Figure 3.13 is an example of this calculation, showing Q factors for threshold condition using Equation 3.13. The panels (a) and (b) of Figure 3.13 are graphs for two different homogeneous broadening. Homogeneous broadening is temperature-dependent, and 7 meV and 0.7 meV are typical values at room temperature and liquid nitrogen temperature for a self-assembled InAs quantum dot. At low temperature, it can be noticed that each quantum dot contribution to gain is visible in the plot. The zigzag curve for Nqd=100 in Figure 3.13 (b) is a result of randomly selecting a quantum

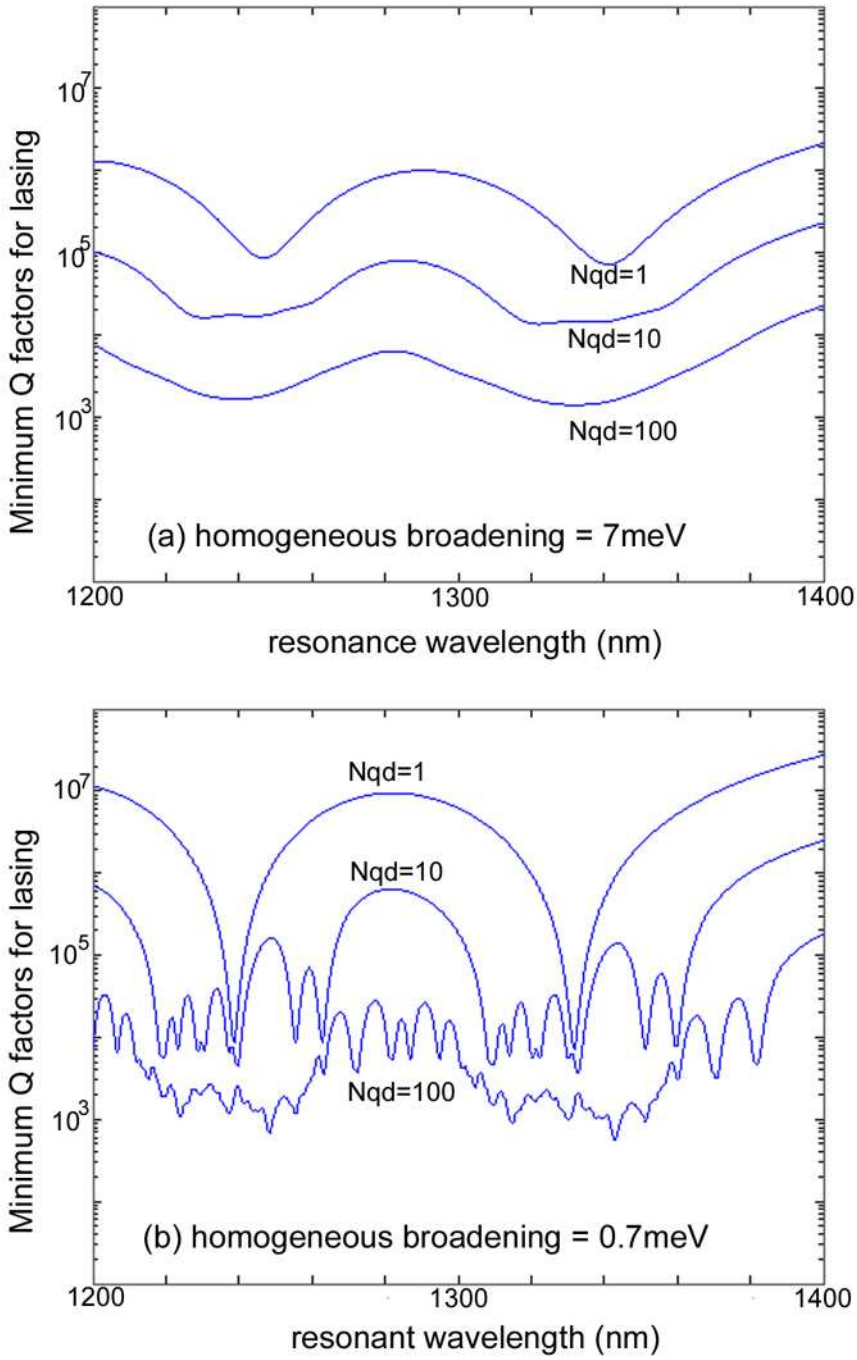

Figure 3.13: Panels (a) and (b) show minimum Q-factors as a function of resonant wavelength to obtain lasing for 7 meV and 0.7 meV of homogeneous broadening. Quantum dots are assumed to be located at maximum electric field point. Calculations are made for three different quantum dot number: 1, 10, and 100. Due to random pick-up of QDs emission energy in Gaussian, the Q factors needed for lasing are fluctuated. $n = 3.4$, $C = 1$, and inhomogeneous broadening is 40 meV.

dot wavelength and narrow homogeneous broadening. The features are smeared out by temperature increase and/or the large number of quantum dots in a cavity.

Figure 3.14 shows a summarized figure of the minimum Q factors as a function of the number of QDs at the maximum E field points and homogeneous broadening of a single QD for obtaining lasing under the above assumptions. The obtained Q values are slightly different from the one in Figure 3.13 because calculations were made at different times. If we repeat the modeling many times, the average values statistically arrive at the most likely points. If $0 < \Delta\rho < 1$ (gain, not loss) or $0 < C_q < 1$, the minimum Q factor can be increased by a factor of $1/(\Delta\rho C_q)$. Assuming that our lasers have Q factors of 2000, $\Delta\rho = 0.7$, homogeneous broadening of 7meV and $C = 1.0$ for four-defect coupled cavities, the effective number of QDs is around 80. This is a reasonable value, considering that the lasing mode has more QDs and the positions of QDs are random. When homogenous broadening is small as shown in Figure 3.13 (b), small inhomogeneous broadening is desirable to have more efficient overlapping of gain between quantum dots. Therefore, in our calculation which uses 40 meV $>>$ 0.7 meV, a reduction of the minimum Q factors is not inversely proportional to the N_{qd} value.

3.6.2 Single QD lasers (Single artificial atom lasers)

A single QD laser [24], which is analogous to a one-atom maser (micromaser) [51, 8], is one of the ultimate laser sources. One-atom masers emit coherent electromagnetic waves in the microwave region, resulting from strong atom-cavity coupling. For example, a three-level system of a single Rubidium 85 is located in a high-Q cavity to create population inversion, and the $63P_{3/2}$-$61P_{5/2}$ transition emits coherent 21.45 GHz microwaves.

When located in a high-Q cavity, the single quantum dot functions as an optical gain source with a sharp linewidth similar to that of an atom. It is desirable to use a solid-state QD instead of an atom beam for photonic circuits and quantum information systems, requiring rich resources of the state of the art telecommunication technology. In addition, the oscillator of a single quantum dot is Lorentzian-shaped, and does not exhibit any inhomogeneous broadening effects. This is a true analog of an atom.

Using Equation 3.9 in the previous section, we can approximately derive the values of Q factors needed to obtain lasing action from a single QD in our PC cavities. The approximations which we used here are not only the ones applied in the previous sections

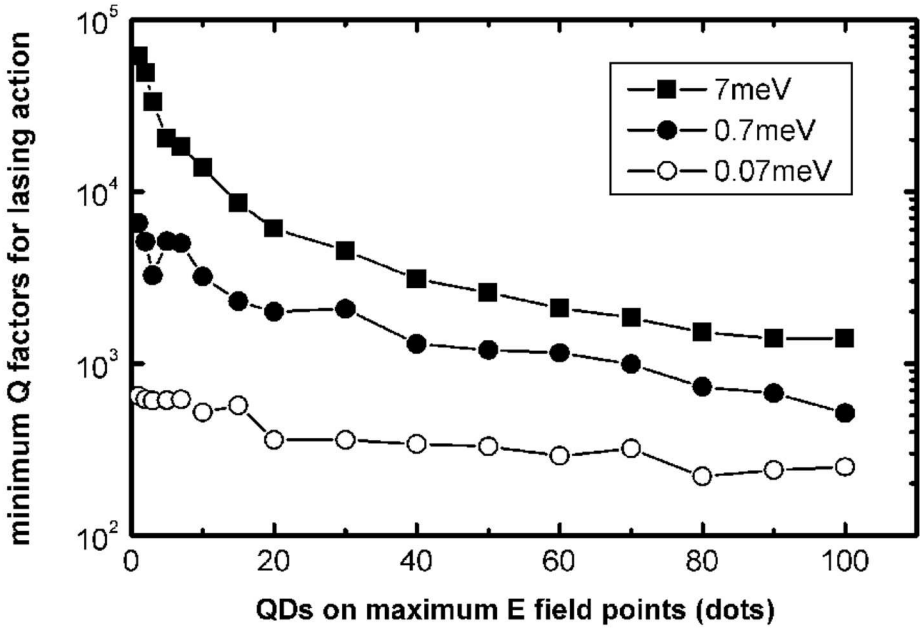

Figure 3.14: Minimum Q factors to obtain lasing as a function of the number of QDs locating on maximum optical field points. Calculations are made for three homogeneous broadening: 7 meV, 0.7 meV and 0.07 meV. Due to random pick-up of QDs emission energy in Gaussian, the Q factors needed for lasing are fluctuated. $n = 3.4$, $C = 1$, and inhomogeneous broadening is 40 meV.

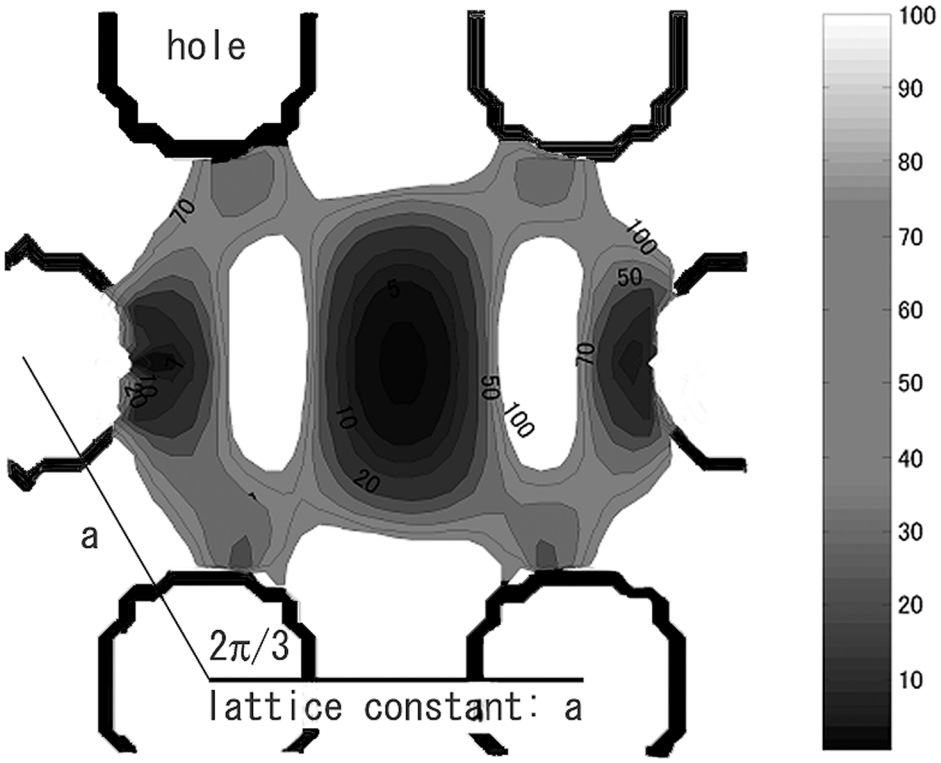

Figure 3.15: Mapping of C_q value dependence on location of QDs for dipole mode in triangular lattice, which has small Q factors. Six circles represent triangular lattice holes in dielectric slab. The figure center is a missing lattice point, which supports dipole modes. A distance between adjacent circles on horizontal axis is a lattice constant (a) of triangular lattice.

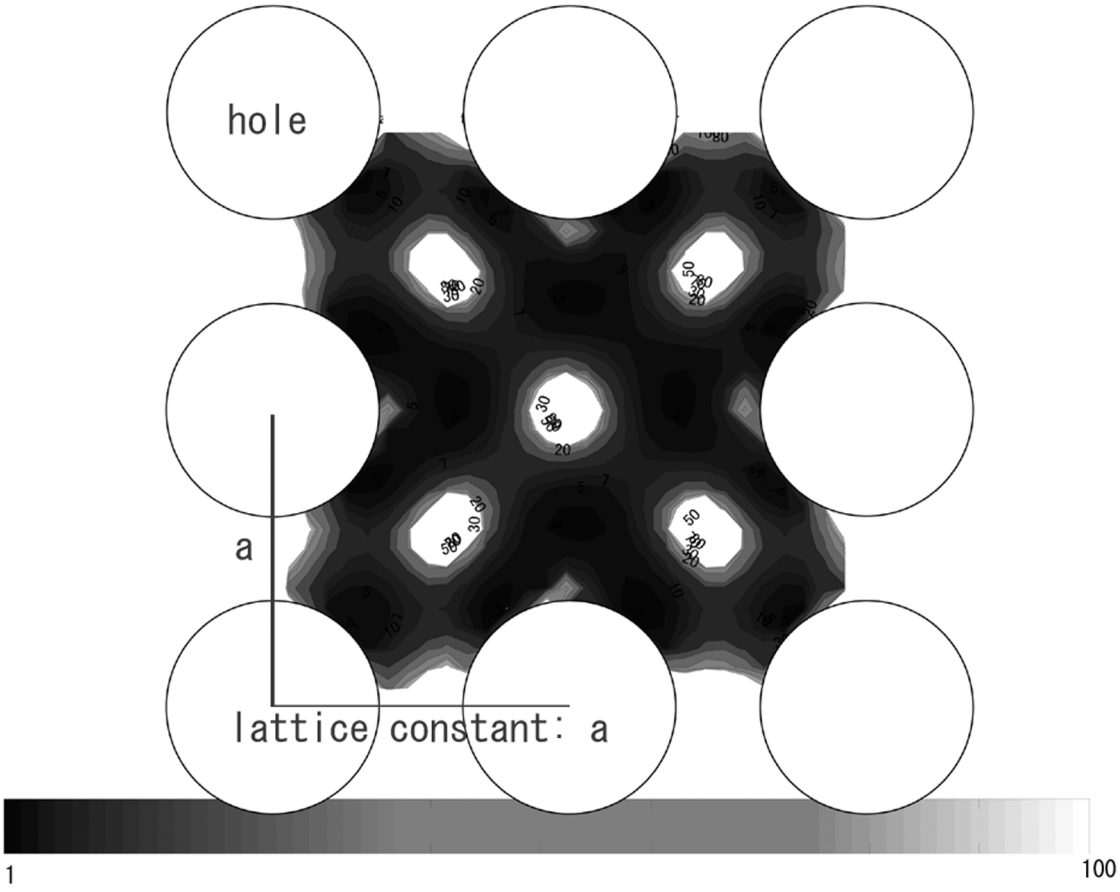

Figure 3.16: Mapping of C_q value dependence on location of QDs for whispering gallery mode in square lattice, which has high Q factors. Eight circles represent square lattice holes in dielectric slab, and the figure center is a missing lattice point, which supports whispering gallery modes. A distance between adjacent circles is a lattice constant (a) of square lattice.

but also radiation process. Figure 3.14 also include minimum Q factors to obtain single QD lasers. At room temperature homogeneous broadening is likely to be around 7meV, and the minimum Q factors for single QD lasing are at least 60,000, which is smaller than the predicted maximum Q factors of quadrapole modes generated in single defect square lattice holes. By decreasing sample temperature to 77K or lower, homogeneous broadening is easily narrowed to less than 1meV. Then lasing is more likely to occur since 6,600 is a minimum Q factor for single QD lasing for homogeneous broadening of 0.7meV.

Pursuing single QD lasing requires a decrease in QD density in the samples, and the decrease makes it unlikely that the single QD is located at the maximum E field points. In order to know the effects from the single QD position, C_q value mappings over PC structures are obtained by using two PC modes of dipole modes in a triangular lattice and quadrapole modes in a square lattice. The analyzed dipole modes have $Q_v = 300$ and $V_{mode} = 0.22(\lambda/n)^3$. Figure 3.15 shows C_q mapping over the middle slice of PC slabs. It can be noticed that the center is the best point to position a single QD for this mode. According to Equation 3.9, necessary Q-factors are 15,000$\times C_q$ and 1,600$\times C_q (\gg 300)$ for homogeneous broadening of 7 meV and 0.7 meV, respectively. Therefore, even though we succeed to locate a single QD at the maximum E field point, single QD lasing does not occur. If the QD position is deviated from the best point, the situation gets worse.

On the other hand, the analyzed quadrapole modes have $Q_v = 97,000$ and $V_{mode} = 0.58(\lambda/n)^3$. Figure 3.16 shows C_q mapping over the middle slice of PC slabs. It can be noticed that we obtain a more distributed area for positioning a single QD for this mode. Necessary Q factors, in this case, are 40,000$\times C_q$ and 4,200$\times C_q (< 97,000)$ for homogeneous broadening of 7meV and 0.7meV, respectively. If we succeed to manipulate the single QD position, single QD lasing is likely to occur. If the QD position is deviated slightly from the best point, single QD lasing may still occur due to more distributed E profile in the confined modes. Therefore, making such high-Q cavities with active QDs is challenging, but it is possible for single QD lasing to occur at room temperature in PC nanocavities.

3.7 Conclusion

Low-threshold two-dimensional photonic crystal quantum dot nanolasers have been demonstrated by using coupled cavity designs of quadrapole modes excited in square photonic

crystals. Our lasers showed as small an absorbed threshold power as 20 μW and 60 μW (or less) and as big a β factor as, approximately, 0.3 and 0.1 for the two-defect and four-defect coupled cavities, respectively. Based on threshold condition analysis, 80 is the effective number of QDs in order to make PC cavities transparent. Using the same analysis, we found that single quantum dot lasing is possible by proper alignment of the single quantum dot relative to geometric structures of the PC and by using high-Q localized modes.

Chapter 4

High-Speed Photonic Crystal Nanolasers

4.1 Introduction

Optical nanocavities offer the unique ability to enhance or inhibit spontaneous emission [65], to control the radiation lifetime [25, 101], and to generate high electric field. The purpose of this thesis is to explore the fundamental limits of miniaturization of such optical cavities for photon localization, and it was found that many of the functional building blocks for integrated optical systems, such as lasers, optical traps [54, 79] and logic gates greatly benefit from such miniaturization. Since photon localization [36, 96] has been predicted to occur when introducing disorder within microfabricated photonic crystals [6, 41], much attention has been focused on finding the smallest localized mode with the smallest energy damping [26, 68, 91] in microfabricated photonic bandgap structures. One of the first devices based on localization of light in optical nanocavities was the photonic crystal laser [59], described by several groups [29, 34, 42, 45, 46, 81, 105].

However, no experimental results have been reported on the observation of the dynamic effects induced in the photonic crystal lasers. High-speed direct modulation is one of the advantages of using semiconductor lasers. Diode lasers can operate with current modulation at a certain bias point. The modulation of current directly reflects the output power of laser light to generate optically modulated signals. A typical and good method to observe the speed of lasers is to find the frequency of relaxation oscillation if it exists. The relaxation phenomenon results from a mutual relation between photon and carrier in a cavity. As shown later, the relation is described in the form of coupled equations containing photon density and carrier density, and the behavior resembles an RLC circuit. The relaxation

oscillation frequency is typically given by

$$f_{RO} = \frac{1}{2\pi}\sqrt{\frac{SA}{\tau_p}} \tag{4.1}$$

where S, A and τ_p are photon density, differential gain rate and photon lifetime, and f_{RO} is an internal frequency defining the modulation speed of the laser. Carrier relaxation is assumed to be much faster than photon lifetime. Higher f_{RO} enables one to modulate optical signals at higher rate. For conventional laser diodes, the frequencies are measured up to 40 GHz. In order to obtain higher-rate signal generation, the lasers are sometimes operated above the relaxation oscillation frequency, but the intensity of modulated signal decreases as the operation frequency increases. For frequencies above relaxation oscillation frequency, the rate of falling off in a frequency response curve is 20 and 40 dB/decade for frequency and intensity modulation (FM and IM). Therefore, laser output power should be high to generate such a high modulation rate signals, and the lasers are operated with high current around 1W in order to achieve 50 GHz or above. The peak frequency f_p in frequency response is slightly different from f_{RO} for IM whereas f_p is identical with f_{RO} for FM. The relative intensity noise (RIN $=< \delta P(t)^2 > /P_o^2$) function has a pole at the relaxation oscillation frequency, and the RIN increases for $f < f_{RO}$ and decreases for $f > f_{RO}$. Therefore, it is desirable to use high-speed lasers below the relaxation oscillation frequency to obtain small RIN values as well as to obtain well-modulated signals (to generate high modulation index signals). In this chapter, modulated oscillations are shown in such lasers of up to 130 GHz from our frequency domain measurements, and the physical mechanism will be discussed.

4.2 Dynamic Effects of Microcavity Laser

4.2.1 Frequency response of microcavity lasers

Frequency response is one of the most important characteristics in describing dynamic effects of lasers. The response can be derived from rate equations of photon number and carrier number in a cavity, and the laser behavior such as modulation index is found to be dependent on operation frequency. The method of obtaining frequency response is similar with one reported by Yamamoto, Machida, and Björk [10, 11, 12, 98, 99]. A general form

of rate equations for photon number p and electron number n is given as

$$\frac{dp}{dt} = \left(\Gamma G(n,p) - \frac{1}{\tau_p}\right) p + \frac{\beta}{\tau_{sp}} n \tag{4.2}$$

$$\frac{dn}{dt} = \frac{I}{eV} - \frac{n}{\tau_{sp}} - G(n,p)p \tag{4.3}$$

where Γ, $G(n,p)$ β, τ_p, τ_{sp}, and I are filling factor, optical gain rate per photon, spontaneous emission coupling factor, photon lifetime, spontaneous emission lifetime, and pump rate. We assume that the gain parameter is in the form of $G(n,p) = A(n - n_{th})$, meaning no gain suppression. The Einstein's relation requires that the spontaneous emission rate into the lasing mode is equal to the stimulated emission rate, and one obtains

$$An\Gamma = \frac{n\beta}{\tau_{sp}} \tag{4.4}$$

$$A = \frac{\beta}{\Gamma\tau_{sp}} = \frac{F_p\beta}{\Gamma\tau_{sp,0}} \tag{4.5}$$

where F_p and $\tau_{sp,0}$ are Purcell's factor and spontaneous emission lifetime in free space. The differential gain constant A is proportional to β factor and Purcell's factor F_p. Therefore, increasing β and F_p is helpful to increase modulation bandwidth. The steady-state solution is obtained by setting d/dt to zero,

$$0 = \left(\Gamma G(n,p) - \frac{1}{\tau_p}\right) p + \frac{\beta}{\tau_{sp}} n = \left(\Gamma A(n - n_{th}) - \frac{1}{\tau_p}\right) p + \frac{\beta}{\tau_{sp}} n \tag{4.6}$$

$$\frac{I}{eV} = \frac{n}{\tau_{sp}} - G(n,p)p = \frac{n}{\tau_{sp}} - A(n - n_{th})p \tag{4.7}$$

At threshold, all the electrons recombine as spontaneous emission, assuming negligible non-radiative recombination, the steady-state conditions at threshold are

$$0 = \left(\Gamma G(n_{th}, p_{th}) - \frac{1}{\tau_p}\right) p_{th} + \frac{\beta}{\tau_{sp}} n_{th} = -\frac{p_{th}}{\tau_p} + \frac{\beta}{\tau_{sp}} n_{th} \tag{4.8}$$

$$\frac{I_{th}}{eV} = \frac{n_{th}}{\tau_{sp}} - G(n_{th}, p_{th})p_{th} = \frac{n_{th}}{\tau_{sp}} \tag{4.9}$$

The threshold pump rate is derived as

$$\frac{I_{th}}{eV} = \frac{p_{th}}{\tau_p\beta} = \frac{(\omega/Q)p_{th}}{\beta} \tag{4.10}$$

Therefore, high Q factors and high β factors are helpful for reduction of threshold I_{th} to obtain p_{th}.

The Ω dependence can be obtained by assuming sinusoidal modulation relations into two rate equations. The modulation can be described by $p = p_0 + p_1 e^{i\Omega t}$, $n = n_0 + n_1 e^{i\Omega t}$, and $I = i_0 + i_1 e^{i\Omega t}$. Using these sinusoidal modulation relations, one can obtain

$$\mathbf{B}\overrightarrow{x} = \begin{pmatrix} \frac{1}{\tau_{sp}} + Ap_0 + i\omega & A(n_0 - n_{th}) \\ A\Gamma p_0 + \frac{\beta}{\tau_{sp}} & A\Gamma(n_0 - n_{th}) - \frac{1}{\tau_p} - i\omega \end{pmatrix} \begin{pmatrix} n_1 \\ p_1 \end{pmatrix} = \begin{pmatrix} \frac{i_1}{eV} \\ 0 \end{pmatrix} \tag{4.11}$$

Solving Equation 4.11 for n_1 and p_1 yields

$$\begin{pmatrix} n_1 \\ p_1 \end{pmatrix} = \frac{1}{|\mathbf{B}|} \begin{pmatrix} A\Gamma(n_0 - n_{th}) - \frac{1}{\tau_p} - i\omega \\ -A\Gamma p_0 - \frac{\beta}{\tau_{sp}} \end{pmatrix} \frac{i_1}{eV} \tag{4.12}$$

$$|\mathbf{B}| = \Omega^2 + ib_1\Omega + b_0$$

where

$$b_1 = A\Gamma(n_0 - n_{th}) - Ap_0 - \frac{1}{\tau_{sp}} - \frac{1}{\tau_p}$$

$$b_0 = (\frac{1}{\tau_{sp}} + Ap_0)(A\Gamma(n_0 - n_{th}) - \frac{1}{\tau_p}) - A(n_0 - n_{th})(A\Gamma p_0 + \frac{\beta}{\tau_{sp}})$$

The spectrum of $S(\Omega) = |p_1|^2/|i_1/(eV)|^2$ of microcavity laser is then given by

$$S(\Omega) = \frac{(A\Gamma p_0 + \beta/\tau_{sp})^2}{\Omega^4 + \Omega^2 \left((Ap_0 + \frac{1}{\tau_p} + \frac{1}{\tau_{sp}} + \frac{\frac{\beta i_0}{eVp_0} - \frac{1}{\tau_p}}{1-\beta/\Gamma})^2 - \frac{2Ap_0}{\tau_p} - \frac{2\beta i_0}{eVp_0\tau_{sp}} \right) + \left(\frac{Ap_0}{\tau_p} + \frac{i_0\beta}{eVp_0\tau_{sp}} \right)^2} \tag{4.13}$$

The relaxation oscillation frequency Ω_R is given by

$$\Omega_R = \sqrt{A(n_0 - n_{th})\frac{\beta - \Gamma}{\tau_{sp}} + \frac{1}{\tau_p}(\frac{1}{\tau_{sp}} + Ap_0) - \frac{1}{2}\left[A\Gamma(n_0 - n_{th}) - \frac{1}{\tau_p} - \frac{1}{\tau_{sp}} - Ap_0 \right]^2} \tag{4.14}$$

For negligibly small β values, the spectrum of p_1 and the relaxation oscillation frequency

are deduced to

$$p_1 = \frac{-Ap_0\Gamma}{\Omega^2 - i\Omega(\frac{1}{\tau_{sp}} + Ap_0) - Ap_0/\tau_p}\frac{i_1}{eV} \tag{4.15}$$

$$\Omega_R = \sqrt{\frac{Ap_0}{\tau_p} - \frac{1}{2}\left(\frac{1}{\tau_{sp}} + Ap_0\right)^2} \tag{4.16}$$

Yamamoto *et al.* [99] derived the similar expression of $S(\Omega)$ given by

$$S(\Omega) = \frac{\left(\frac{1+r}{\tau_{sp}}\right)^2}{\Omega^4 + \left[\left(\frac{\gamma}{1+r}\right)^2 + \left(\frac{1+r}{\tau_{sp}}\right)^2 - \frac{2r\gamma}{\tau_{sp}}\right]\Omega^2 + \left(\frac{\gamma(1+r)}{\tau_{sp}}\right)^2} \tag{4.17}$$

where $r = i_0/i_{th}$ and $\gamma = \omega/Q$ are pumping level and damping rate.

The modulation frequency has an upper limit, which is the cutoff frequency of $f_c = \omega/(2\pi Q)$, even though one can reduce the oscillator lifetime considerably. The cutoff frequency for $Q = 1000$ and $\lambda = 1.5\mu$m is about 200 GHz. Figure 4.1 is an example of the frequency response calculated by Equation 4.17 based on a linear gain model, using a pumping level $r = 5$. Gain suppression should be included to predict precise frequency response of high-speed lasers.

4.2.2 Enhanced relaxation oscillation frequency in photonic crystal lasers

Photonic crystal nanocavity can significantly enhance spontaneous emission because of its high Q factor and small mode volume V_{mode}. In the weak light-matter coupling regime, the spontaneous emission rate is enhanced by the Purcell's factor $F_p = \frac{3Q(\lambda/n)^3}{4\pi^2 V_{mode}}$. Even in some portion of the intermediate coupling regime, the radiation rate is enhanced by a slightly higher rate than the rate expected from the Purcell's effects. When this condition is satisfied, the radiation rate is enhanced. Then, assuming perfect oscillator-field coupling ($d \cdot E = |d||E|$), the modified spontaneous emission lifetime τ_{sp} is given by:

$$\tau_{sp} = \frac{1}{F_p}\frac{|E|^2_{osc}}{|E|^2_{max}}\tau_o \tag{4.18}$$

where τ_o, E_{max}, and E_{osc} are spontaneous emission lifetime of oscillator in free space, maximum electric field of mode, and electric field at an oscillator location. For example, we showed $F_P = 500$ from a fractional dislocation cavity design, and the modified spontaneous

emission lifetime can be reduced by a factor of 500 when the oscillator is prepared on the maximum field point and at resonance. It is important to locate oscillators at maximum field point with high coupling with the field. For a quadrapole mode created by a single defect in a square lattice crystal, typical resonance wavelength (1.5 μm) divided by linewidth $\lambda/\Delta\lambda$ is around 2000, and the mode volume is $0.5 \times (\lambda/n)^3$. The Purcell's factor F_p is 300, and the cutoff frequency due to cavity damping is 100 GHz. Typical spontaneous emission lifetime for our quantum well radiation is one to a few nanoseconds, and the expected modified spontaneous emission lifetime is around 3 to 10 psec. The corresponding modulation bandwidth is 16 to 50 GHz for a microcavity LED. Further increase in modulation bandwidth is possible for a microcavity laser operating above the threshold.

4.2.3 Built-in saturable absorber effects

In the preceding subsections, one finds that high-speed lasers can be constructed by using a cavity with appropriate Q factor and mode volume. This speed is the internal speed of the lasers, and practical high-speed laser light is directly modulated by modulation of electrical signals. Careful electrical designs are essential to avoid big RC components, which result in zero transmission of modulated electrical signals, and electrically pumped lasers are necessary to conduct electrical modulation. However, electrically pumped photonic crystal lasers in this wavelength have not been fabricated [18], and it is not feasible to observe such high frequency oscillation by using the typical method at present.

However, it is possible to produce an appropriate setting where relaxation oscillations are excited. Our approach to excite the oscillation is to use automatic modulation of signals by incorporating a saturable absorber in a cavity system. Emission and absorption processes in the cavity often create relaxation oscillation. Saturable absorber has the following nonlinear relation of absorption (α) as a function of photon flux density (ϕ) in the absorber [74].

$$\alpha(\nu) = \frac{\alpha_o(\nu)}{1 + \frac{\phi_s}{\phi(\nu)}} \tag{4.19}$$

When ϕ is small, the absorption is proportional to ϕ. Increasing the photon flux in the gain material, the absorption start to deviate from the linear relation with the photon flux density, and finally saturates to a value of $\alpha_o(\nu)$. This nonlinear relation makes our lasers operate under non-linear behavior. It is possible to produce nonlinearities in laser diodes by

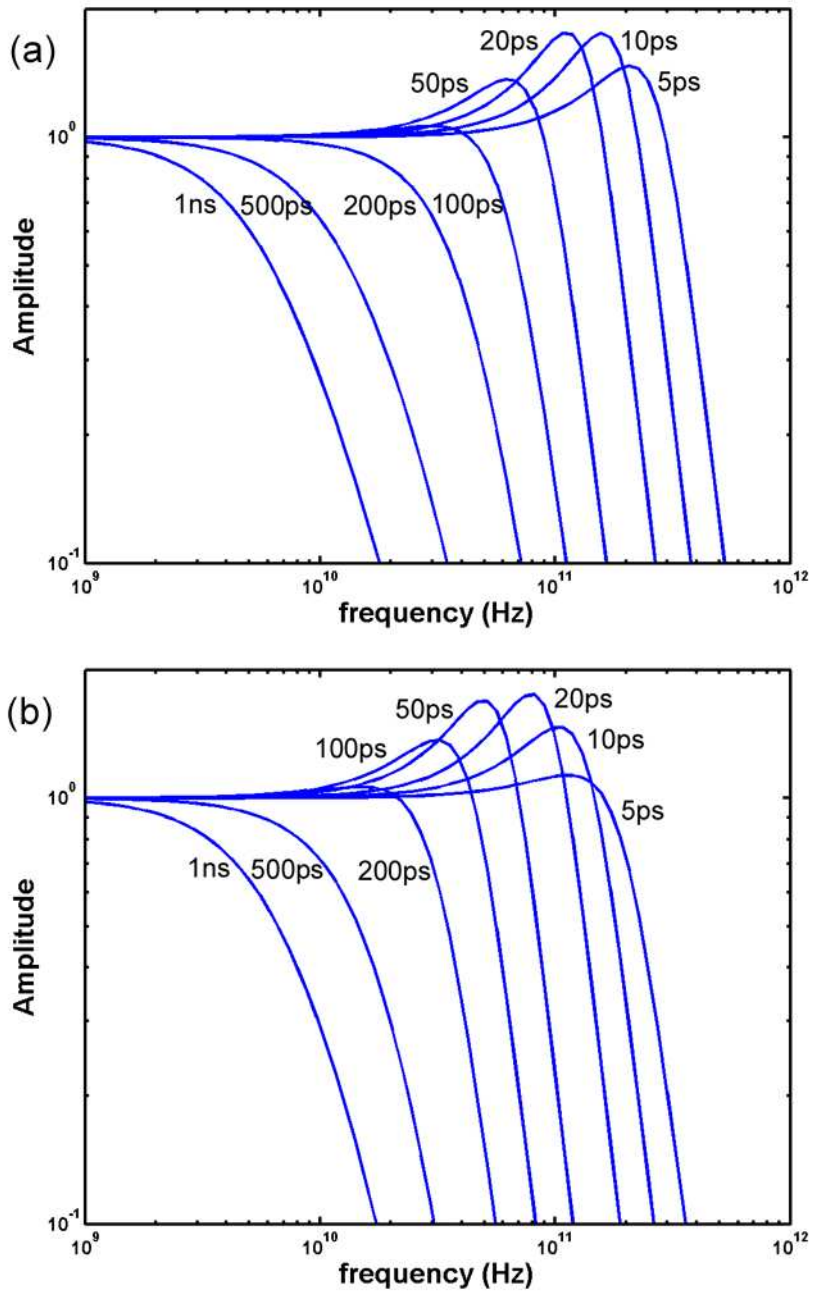

Figure 4.1: Frequency response of amplitude modulation in microcavity lasers as a function of modified spontaneous emission lifetime τ_{sp}. Panels (a) and (b) are the response curves for Q =500 and Q =1000. The used parameters are pumping level P/P_{th} =5 and $\lambda = 1.5$ μm. The cutoff frequencies resulting from a cavity damping are 400 GHz and 200 GHz for Q =500 and 1000, respectively, for these parameters. The modelling is based on linear gain, and it doesn't include a gain suppression effect.

changing parameters involved in the coupled rate equations. Examples are bistable lasers [38], self-pulsating lasers [94, 97], Q-switching lasers, and unstable lasers [75]. It should be noted that self-pulsating laser is one of unstable lasers.

For two-section laser diodes (regions a and b), it is easy to produce a situation where bifurcation occurs. Bifurcation is the mathematical reason to construct self-pulsating lasers and bistable lasers. The general form of an evolution equation in $\mathbf{R}^1$ to produce the bifurcation is:

$$\frac{du}{dt} = F(\mu, u) \tag{4.20}$$

Of course, two-section lasers can be described in the form of coupled equations in each section of lasers, and the form can be deduced into the form of Equation 4.20. The periodic solutions are self-pulsating lasers at steady state, and Equation 4.20 have two solutions, for bistable lasers, which simultaneously satisfy the bifurcation problem. The relative unsaturated absorption (β_{absp}), the ratios of carrier lifetime and gain (τ_a/τ_b and g_a/g_b), and volume fraction of the absorbing region in the cavity (h) are typically key parameters in determining the type of lasers. The bistable region (i) and the self-pulsating regions (ii) are defined [38] by,

$$\text{(i)}\ \frac{\tau_a g_a}{\tau_b g_b} < \frac{-\beta_{absp}}{1-\beta_{absp}} \tag{4.21}$$

$$\text{(ii)}\ \frac{\tau_a g_a}{\tau_b g_b} > \frac{-\beta_{absp}}{1-\beta_{absp}} \text{ and } \frac{\tau_a}{\tau_b} > \frac{1}{1-h}\frac{1-\beta_{absp}}{\beta_{absp}}\frac{g_a}{g_b} + 1 \tag{4.22}$$

The carrier lifetime τ is dependent on non-radiative recombination including surface recombination. Typical photonic crystal structures have many holes to define refractive index periodicity. The surface recombination is by nature easily-enhanced. By appropriate pumping, it is feasible to create the condition of self-pulsating lasers. Two-section lasers become bistable lasers when non-radiative lifetime is long. Therefore, it would be challenging to create bistable photonic crystal lasers by using the same method as typical two-section lasers.

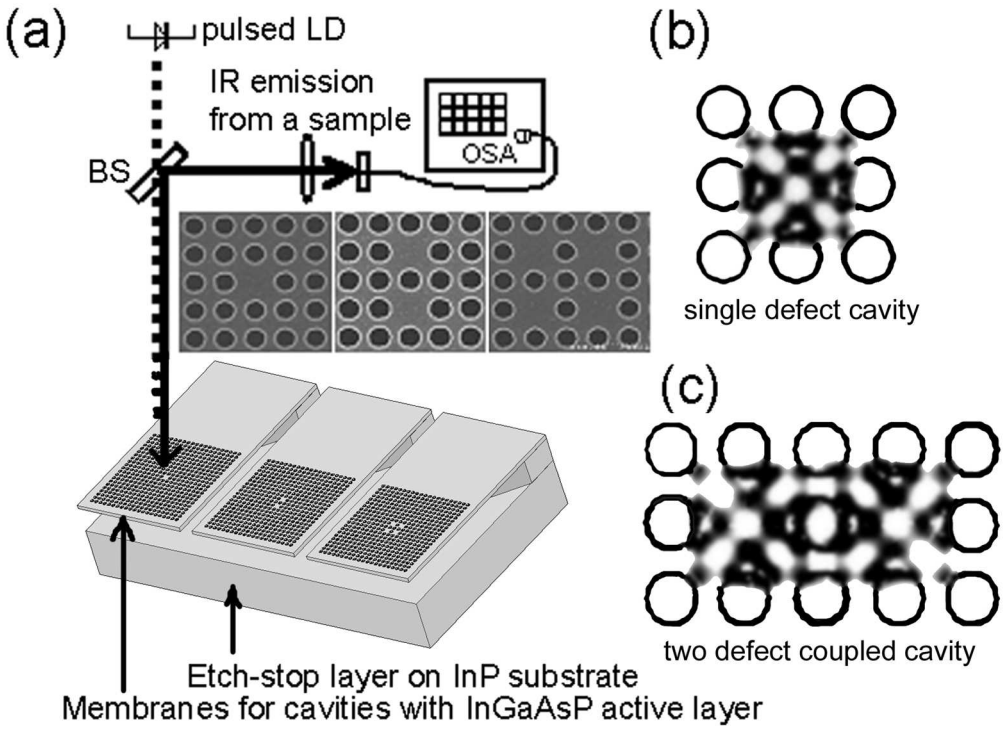

Figure 4.2: Two-dimensional photonic crystal slabs with square lattice used in the work. Panel (a) shows drawings of single defect, two-coupled defect, and four-coupled defect cavity membrane structures. The circles represent optically pumped regions, outsides of which are quantum well as saturable absorber. Panels (b) and (c) show electric field amplitude profiles in a middle of membrane for single defect and two-coupled defect cavity membrane structures, respectively. One of supermodes is shown for two-defect coupled cavities.

4.3 High-Speed Quantum Well Photonic Crystal Nanolasers

4.3.1 Sample preparation

Several designs of square and triangular lattice photonic crystals were evaluated. Here we focus on the high-quality factor (Q) whispering gallery modes (quadrapole modes) supported by square lattice photonic crystals [68, 105]. Geometries of single-, double-, and quadruple-defect coupled cavities are shown in Figure 4.2(a). The defect(s) were fabricated in the center of 21 by 21 square lattices of holes in order to ensure the effective confinement of in-plane light. We modelled the 2-D photonic crystal slab cavity by using three-dimensional finite difference time domain (3D-FDTD) simulation, and calculated mode volumes (V_{modes}) of $0.6\times$, $0.8\times$ and $1.1\times(\lambda/n)^3$ for cavities consisting of single-, two-, and four coupled defects.

Material	Function	Doping [cm^{-3}]	Thickness [nm]
p-InP	cap layer	1×10^{17}	50
i-InGaAsP	Barrier	1×10^{17}	100
i-InGaAsP QW	Active region	undoped	9
i-InGaAsP	Barrier	1×10^{17}	20
i-InGaAsP QW	Active region	undoped	9
i-InGaAsP	Barrier	1×10^{17}	20
i-InGaAsP QW	Active region	undoped	9
n-InGaAsP	Barrier	1×10^{17}	100
n-InP	Sacrificial layer		1500
n-InGaAs	Etch-stop layer		20
n-InP	substrate	1×10^{18}	

Table 4.1: Layer structure of InGaAsP quantum well sample used for photonic crystal nanolasers.

To construct our lasers, four InGaAsP quantum wells were grown to form a 330nm thick light-emitting slab on an InP substrate. Table 4.1 shows a layer structure of the wafer. On the wafer, 130 nm SiON film was deposited by plasma-enhanced vapor deposition (PCVD) as an etching mask during ICP-RIE etching. Electron beam lithography is used to define the square lattice designs in resists. The patterned resists are used as etching masks during RIE to transfer the patterns into the 130 nm SiON film. Following the RIE process, the samples were etched by using gas combinations of either Cl_2/Ar or HI/Cl_2/H_2/Ar in our ICP-RIE system. Both gas combinations in the ICP-RIE process are effective for etching InGaAsP materials in an anisotropic profile. The etched depth reaches beyond the n-InGaAsP/n-InP interface, but does not reach the interface of n-InP/n-InGaAs. The remaining SiON film, thinned by the ICP-RIE process, is removed by dipping the sample in buffered-HF, and the top p-InP layer is subsequently removed by diluted HCl solution. The long soaking in HCl allows the InP layer under the cavity slab to be etched gradually. As a result, suspended planar photonic crystal membranes are formed after careful drying.

In typical PC lasers, the lattice spacing (a) is 450 nm, and the slab thickness (d) is 330 nm. The porosity defined by r/a was varied between 0.34 and 0.36 and d/a was varied from 0.6 to 0.8. Calculated Q values have a range of 50,000 to 100,000 and λ, the resonance wavelength, was matched to the quantum well (QW) emission wavelength at 1550 nm. However, because of active structures and structure roughness, the $\lambda/\Delta\lambda$ values are limited from 1000 to 6000 at threshold. Figures 4.2 (b) and (c) show typical amplitude profiles of

the electric field within the center of the membranes obtained from a high-Q quadrapole mode. Figure 4.2 (c) shows one of two supermodes formed in a two-defect coupled cavity.

4.3.2 Experiments to observe relaxation oscillation

We tested all of our lasers by optically pumping using an 830 nm laser diode at room temperature. The schematic drawing of our setup is shown in Figure 4.2 (a). During measurement, the pump beam was focused to a 2μm diameter spot and carefully aligned onto the center of our photonic crystal cavities. Part of the emission from the PC nanolasers was directed through a 100$\times$ objective lens and coupled into an optical fiber to an optical spectrum analyzer. The wavelength resolution of the analyzer was 0.2 nm, whereas the 2 μm optical pump beam was larger than the mode volume defined by V_{mode}=$\int \epsilon(r)E^2(r)dV/max[\epsilon(r)E^2(r)]$, and rendered most of the photonic crystal within that lasing mode transparent. However, the tails of the electric field from the lasing mode extend beyond the optically pumped transparent photonic crystal, and interact with the un-pumped absorbing material. In fact, we find by careful 3D-FDTD modelling that the three layers of photonic crystal pumped by a 2 μm diameter pump beam reflect only approximately 99% of the light. Therefore, the unpumped material surrounding the laser cavities functions as a passive saturable absorber that can give rise to non-linear effects in photonic crystal nanolasers, such as bistability [27], self-pulsation and Q-switching. This partial pumping is key in producing nonuniform pumping level $g_{a,b}$ of the system, resulting in dynamic behaviors of our lasers.

We have measured luminescence spectra as a function of peak pump power, which are presented in Figure 4.3 (a) and (b) for 15 nsec and 50 nsec pulses separated by 50 μsec on a quadruple-defect coupled cavity. Two out of four whispering gallery supermodes were pumped beyond the lasing threshold. The duty cycles for the pump beam under these conditions are 0.03% and 0.1%, respectively, limited to avoid cavity heating. At duty cycles below 1%, the luminescence spectra from our lasers were observed to broaden with increasing pump pulse length, and several smaller peaks emerge in the lasing spectrum. These additional peaks are not artifacts from cavity heating, but a result of the time-resolved dynamics within nanolaser cavities that are surrounded by saturable absorbing QW material. Whereas clear symmetric peaks are apparent in measurements using 15 nsec pulses, additional equidistant peaks (labelled A2 and B2) as well as extending tails of peaks A1 and B1 appear in 50 nsec pulse measurements. Similar observations were made for all

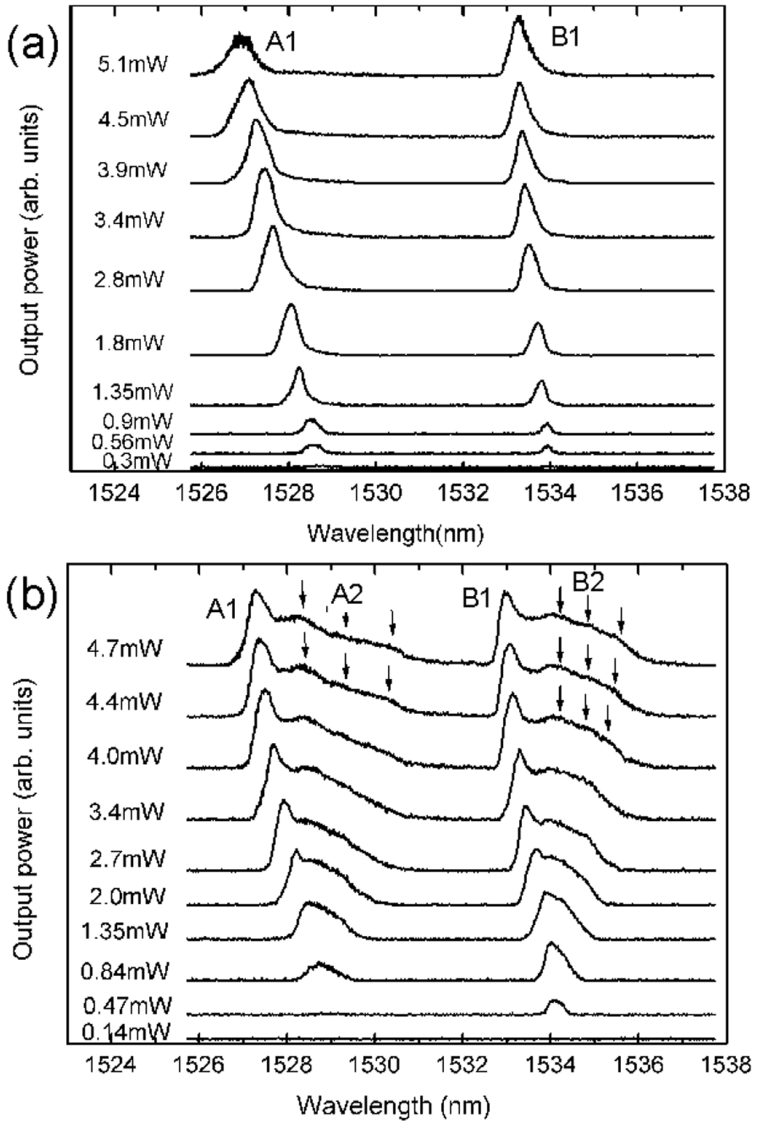

Figure 4.3: Laser characteristics. Panels (a) and (b) show luminescence spectra as a function of pumping peak power for 15 nsec and 50 nsec pulse operations, respectively, in four-defects coupled cavities. Peaks A2 and B2 are three symmetric equidistance peaks after subtracting A1 and B1 with tails. The threshold pump powers are 200 μW for A1 and B1 peaks for 15nsec pulses.

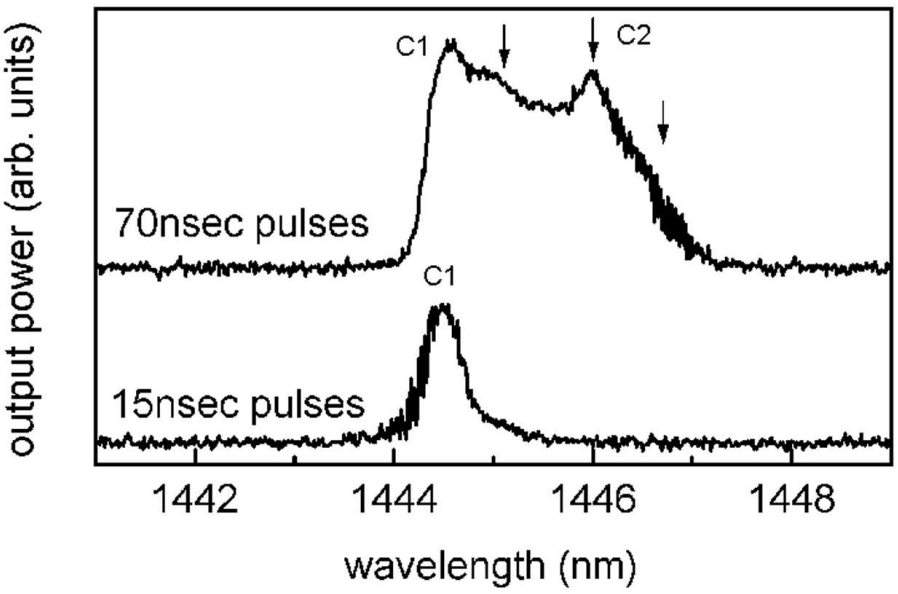

Figure 4.4: Luminescence spectra measured by 15 nsec and 70 nsec-pumping pulses with a 50 μsec repeat rate at 77 K from a single defect square lattice photonic crystal slab cavity (a = 450 nm, $r = 0.34a$). The PC cavity supported single mode lasing of quadrapole mode in this case. A center peak of C2 peaks are more pronounced than one in 50 nsec pulses.

of our laser cavities, including single-, two- and four-defect coupled cavity photonic crystal lasers, independent of the number of lasing modes. This pulse-length dependent spectral behavior occurs even in our triangular lattice photonic crystal lasers with fundamentally different cavity designs supporting dipole modes. Separations of equidistant peaks depend upon modes as can be seen from peaks A2 and B2. The blue shift of the sharp peaks (A1 and B1) seen in Figures 4.3 (a) and (b) can be explained by frequency pulling and/or denser electron-hole plasma.

4.3.3 Discussions

We have made the following observations in this experiment: (1) A state producing equidistance peaks below the sharp lines is delayed to occur and the sharp peaks A1 and B1 initiate the occurrences of A2 and B2 peaks, meaning switching from states 1 to states 2. (2) As the pump power is increased, three equidistance peaks are more pronounced and the spectral shifts are increased.

Experimentally, we observed that the three equidistance peaks vanish when the pumping diameter is widened to cover the entire lasing mode, which renders the photonic crystal

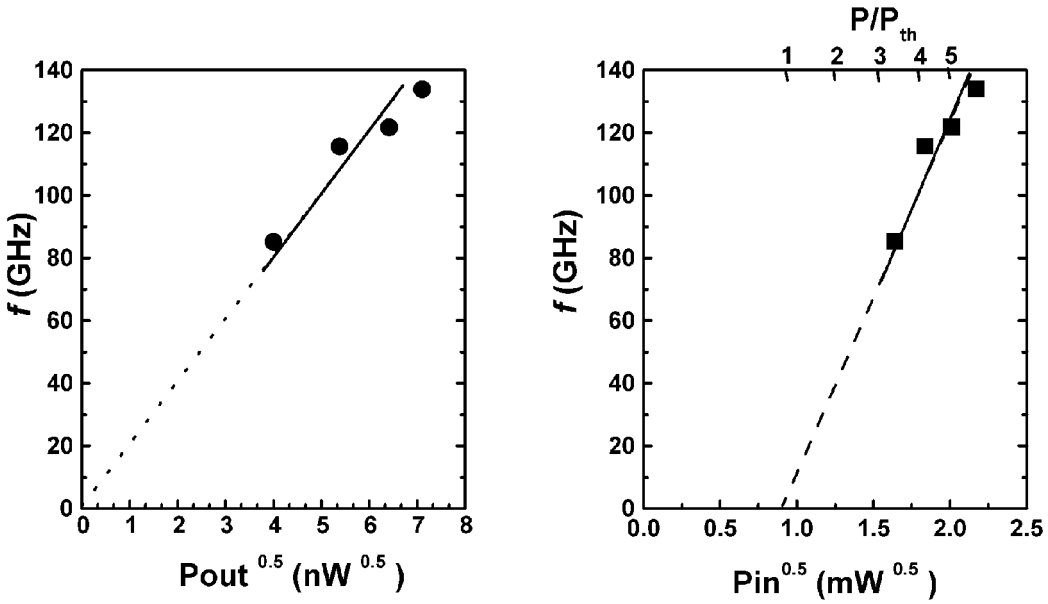

Figure 4.5: Frequency f as a function of square root of collected output peak power ($\sqrt{P_{out}}$). The sample was chosen such that the sample had the widest spacing between three equidistance peaks on pumping 50 nsec pulsed with a period of 50 μsec. The output power is normalized as a peak power.

transparent. Thus, we have confirmed that the QW saturable absorber surrounding the laser cavity provides the driving force, which gives rise to the additional spectral peaks.

Moreover, the equidistant peaks are still observed at 77 K, only for longer pulses as shown in Figure 4.4, which confirms that the additional peaks C2 do not result from sample heating, but from saturable absorption. This effect is not observed in quantum dot PC lasers [105], possibly, either because the self-assembled InAs quantum dots do not provide enough absorption for strong non-linear cavity behavior or the noise generated in the cavity is too small to observe the additional peaks.

The three equidistance peaks, which we observe in our 50nsec pulse spectra, cannot be explained by mode locking. In mode locking, the spectral separation should be independent of the pumping conditions and dependent on the round trip of the cavity. Instead, there are two possible physical mechanisms to explain these observed effects. They are (1) intensity modulation and (2) frequency chirping. Both physical reasons can cause relaxation oscillation giving three equidistant peaks with a spacing of the relaxation oscillation frequency.

4.3.3.1 Intensity modulation

Intensity-modulated oscillation, which depends on the pumping conditions of the laser cavity, explains our observation that these peaks remain at approximately the same relative spectral separation. Relaxation oscillation [87] or absorption-induced self-pulsation can be used to understand the modulated oscillations. The relaxation frequency is defined by Equation 4.1. It should be noted that the absorption-induced self-pulsation frequency would be smaller than the relaxation oscillation and that the frequency dependence on photon density is sometimes similar to the dependence of relaxation oscillation [52]. In order to extract the relation of frequencies and photon density from our spectral measurements, we de-convolved the spectrum into one sharp Lorentzian peak with a tail in longer wavelength and three equidistant sub-peaks. The sub-peak wavelengths and the integrated powers underneath each of these peaks were determined, and the sum of integrated power in all but the shortest wavelength peak was defined as $P_{out}(\propto S)$. Figure 4.5 shows a plot of frequency f, measured from the spacing between the equidistance peaks, as a function of $\sqrt{P_{out}}$. The laser used for Figure 4.5 was chosen to exhibit the maximum wavelength difference between the sub-peaks, and was a two-defect coupled cavity (a=460 nm, r=0.34a) with an optical mode volume of $0.8(\lambda/n)^3$. The measured peak frequency is found to be proportional to the square root of output power as predicted from Equation 4.1. The maximum measured frequency was 130($\pm$15) GHz, and could be tuned between 60($\pm$6) to 130($\pm$15) GHz by changing the precise cavity geometry and optical pumping condition. For low photon density in the cavity, the 3dB frequency f_{3dB} can be reached up to 200 GHz because of the relation: $f_{3dB} \simeq 1.55 f_{RO}$. Most of the nanolasers exhibit maximum frequencies of 80–100 GHz in our measurement range. The measured frequencies are consistent with microcavity laser theory [99]. Taking $Q = 1000$, modified spontaneous emission lifetime $\tau_{sp} = 5$ psec and pump rate relative to threshold pump power $P/P_{th} = 5$, the relaxation frequency is 130 GHz. The cutoff frequency is around 200 GHz.

4.3.3.2 Frequency chirping

Frequency chirping or frequency modulation of lasers [17] can also explain these measured results. The modulation of the carrier density in a cavity modulates the gain through population inversion, but it also modulates the refractive index of the gain region. Therefore,

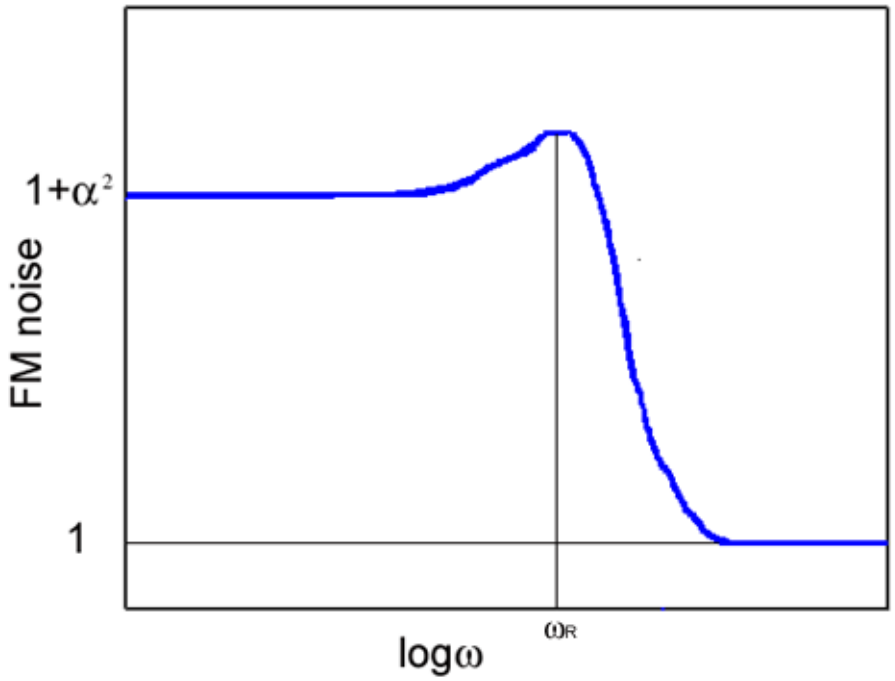

Figure 4.6: Typical frequency noise spectrum of lasers.

the resonant modes are modulated in frequency domain. The bandwidth of FM is generally broader than one for IM. The observed broad spectra may be the results of the frequency chirping. This effect is not desirable for using the lasers under intensity modulation, but it is not crucial here because our purpose in operating the lasers in this manner is to probe the internal frequencies of lasers.

Frequency noise spectral density [17] is given by

$$S_\nu(\omega) \quad = \quad \frac{1}{2\pi}(\Delta\nu)_{ST}\left(1+\alpha^2|H(\omega)|^2\right) \tag{4.23}$$

where $|H(\omega)|^2$ is modulation transfer function in intensity and α is the linewidth enhancement factor defined as

$$\alpha \quad = \quad -\frac{dn_r/dN}{dn_i/dN} \tag{4.24}$$

where the complex index is $n = n_r + n_i$, and N is carrier density. $(\Delta\nu)_{ST}$ is the modified Schawlow-Townes linewidth. Therefore, the frequency noise spectral density is drawn in

Figure 4.6. The FM noise curve is similar to the modulation intensity curve $|H(\omega)|^2$, but it deviates at high frequency above relaxation oscillation frequency from the shape of $|H(\omega)|^2$. The noise level at high frequency results from spontaneous emission noise, which is understood in quantum mechanics.

In a cavity containing saturable absorber, events of emission and absorption randomly occur. This random noise is enhanced at resonant frequency, and the noise components around relaxation oscillation is further enhanced than the other frequency components as shown in Figure 4.6. Therefore, in frequency domain, the sidebands corresponding to $\pm f_{RO}$ appear for frequency chirping. Figure 4.5 shows the frequency spacing is square root of photon density, supporting the hypothesis that the sideband is a result of relaxation oscillation. Frequency chirping is also a good explanation of physical mechanism for creating relaxation oscillation.

For quantum dot photonic crystal lasers, the broadened spectra have not been observed. The reason may be low noise or smaller damping rate. The fabrication roughness is smaller in QD-PC lasers than in InGaAsP QW photonic crystal lasers, and the Q factors are higher in QD-PC cavities. Therefore, there are no conflicts in explaining the observed results using frequency chirping. If frequency chirping is the reason for relaxation oscillation, the fact that broadened spectra have not been seen is a good signature since the broadened spectra are direct results of frequency modulation noise. Quantum dot photonic crystal lasers can be noiseless high-speed lasers. The spontaneous emission lifetime of QDs is around 1 nsec, and Q factors in cavities fabricated in quantum dot material are controllable for optimizing the balance between modified spontaneous emission lifetime and cavity damping time. Therefore, quantum dot photonic crystal lasers are likely to operate high-speed modulation up to 100 GHz with small power consumption and low noise because the speed may be limited by carrier relaxation time, typically 10 to 100 psec, from the 1st excited state to the ground state. However, one can expect quantum dot with short carrier relaxation time to be developed in the near future, and high-speed QD photonic crystal lasers will benefit from the efforts to make such QDs.

In order to find out additional explanation of relaxation oscillation, further study is necessary. Frequency fluctuation spectrum (autocorrelation) [88, 89] and temporal evolution measurements would be helpful in determining the origin of relaxation oscillation. Figure 4.6 shows typical shape of the frequency noise spectrum.

4.3.4 Performance comparisons with conventional lasers

A radical decrease in the mode volumes reducing photon lifetimes and increasing photon density and an increase in Purcell's factor result in an increase in modulation frequencies. Due to the smaller photon number and the larger spontaneous emission coupling factor (β), the linewidth becomes wider resultiing in a similar modulation frequency as for conventional lasers. Whereas conventional lasers require 100 mW input power for 30 GHz operation [53], the 130 GHz operation observed in PC lasers could be observed at surprisingly small absorption power (of less than 1 mW). It should be noted that the absorbed power is less than 20 % of pumping power. To construct practical high-speed lasers, we need electrically pumped lasers [18] and careful designs to avoid large RC components. By modification of the focused spot size of our optical pump beam, we can control the influence of the QWs surrounding the cavity. Although such tuning of the saturable absorber can be used to switch on the high frequency oscillations, we have not yet confirmed that our PC nanolasers are self-oscillating lasers or relaxation-oscillated lasers.

4.4 Conclusions

In summary, we have fabricated and tested high-Q planar quantum well photonic crystal cavities with mode volumes ranging between 0.5 and 1.2 cubic wavelengths and observed 130 GHz modulated oscillations. This is the first observation of dynamic behavior of photonic crystal nanolasers by probing the relaxation oscillations. This modulation arises from self-induced non-linear effects and is a direct result of re-absorption of light in the un-pumped mirrors surrounding the optical cavity. This increase in laser speed results from miniaturization of the cavities. The sidebands are direct results of relaxation oscillation, and the relaxation oscillation are possibly results from intensity modulation or frequency chirping. We could not probe relaxation oscillation on quantum dot photonic crystal lasers at the time of writing, but this may be a good signature as noiseless high-speed laser diodes.

Bibliography

[1] Y. Akahane, T. Asano, B. S. Song, and S. Noda, *High-Q photonic nanocavity in a two-dimensional photonic crystal*, Nature **425** (2003), no. 6961, 944–947.

[2] P. W. Anderson, *Absence of diffusion in certain random lattices*, Physical Review **109** (1958), no. 5, 1492–1505.

[3] L. C. Andreani, G. Panzarini, and J. M. Gerard, *Strong-coupling regime for quantum boxes in pillar microcavities: Theory*, Physical Review B **60** (1999), no. 19, 13276–13279.

[4] K. Aoki, H. T. Miyazaki, H. Hirayama, K. Inoshita, T. Baba, K. Sakoda, N. Shinya, and Y. Aoyagi, *Microassembly of semiconductor three-dimensional photonic crystals*, Nature Materials **2** (2003), no. 2, 117–121.

[5] Y. Arakawa and H. Sakaki, *Multidimensional quantum well laser and temperature dependence of its threshold current*, Applied Physics Letters **40** (1982), no. 11, 939.

[6] T. Baba, *Photonic crystals and microdisk cavities based on GaInAsP-InP system*, IEEE Journal of Selected Topics in Quantum Electronics **3** (1997), no. 3, 808–830.

[7] T. Baba, T. Hamano, F. Koyama, and K. Iga, *Spontaneous emission factor of a microcavity DBR surface-emitting laser*, IEEE Journal of Quantum Electronics **27** (1991), no. 6, 1347–1358.

[8] P. R. Berman (ed.), *Cavity quatnum electrodynamics*, Academic Press, San Diego, 1994.

[9] D. Bimberg, N. N. Ledentsov, and M. Grundmann, *Quantum dot heterostructures*, Wiley, New York, 1999.

[10] G. Bjork, H. Heitmann, and Y. Yamamoto, *Spontaneous-emission coupling factor and mode characteristics of planar dielectric microcavity lasers*, Physical Review A **47** (1993), no. 5, 4451–4463.

[11] G. Bjork, S. Machida, Y. Yamamoto, and K. Igeta, *Modification of spontaneous emission rate in planar dielectric microcavity structures*, Physical Review A **44** (1991), no. 1, 669–681.

[12] G. Bjork and Y. Yamamoto, *Analysis of semiconductor microcavity lasers using rate equations*, IEEE Journal of Quantum Electronics **27** (1991), no. 11, 2386–2396.

[13] H. J. Carmichael, R. J. Brecha, M. G. Raizen, H. J. Kimble, and P. R. Rice, *Subnatural linewidth averaging for coupled atomic and cavity mode oscillators*, Physical Review A **40** (1989), no. 10, 5516–5519.

[14] R. K. Chang and A. J. Campillo (eds.), *Optical processes in microcavities*, World Scientific, Singapore, 1998.

[15] C. C. Cheng and A. Scherer, *Fabrication of photonic band-gap crystals*, Journal of Vacuum Science & Technology B **13** (1995), no. 6, 2696–2700.

[16] C. Cohen-Tannoudji, J. Dupont-Roc, and G. Grynberg, *Atom-photon interactions*, Wiley, New York, 1998.

[17] L. A. Coldren and S. W. Corzine, *Diode lasers and photonic integrated circuits*, Wiley, New York, 1995.

[18] R. Colombelli, K. Srinivasan, M. Troccoli, O. Painter, C. F. Gmachl, D. M. Tennant, A. M. Sergent, D. L. Sivco, A. Y. Cho, and F. Capasso, *Quantum cascade surface-emitting photonic crystal laser*, Science **302** (2003), no. 5649, 1374–1377.

[19] D. G. Deppe, L. A. Graham, and D. L. Huffaker, *Enhanced spontaneous emission using quantum dots and an apertured microcavity*, IEEE Journal of Quantum Electronics **35** (1999), no. 10, 1502–1508.

[20] D. G. Deppe, D. L. Huffaker, S. Csutak, Z. Zou, G. Park, and O. B. Shchekin, *Spontaneous emission and threshold characteristics of 1.3-μm InGaAs-GaAs quantum-dot GaAs-based lasers*, IEEE Journal of Quantum Electronics **35** (1999), no. 8, 1238–1246.

[21] B. D'Urso, O. Painter, J. O'Brien, T. Tombrello, A. Yariv, and A. Scherer, *Modal reflectivity in finite-depth two-dimensional photonic crystal microcavities*, Journal of the Optical Society of America B-Optical Physics **15** (1998), no. 3, 1155–1159.

[22] P. G. Eliseev, H. Li, A. Stintz, G. T. Liu, T. C. Newell, K. J. Malloy, and L. F. Lester, *Transition dipole moment of InAs/InGaAs quantum dots from experiments on ultralow-threshold laser diodes*, Applied Physics Letters **77** (2000), no. 2, 262–264.

[23] B. Gayral, J. M. Gerard, B. Sermage, A. Lemaitre, and C. Dupuis, *Time-resolved probing of the purcell effect for InAs quantum boxes in GaAs microdisks*, Applied Physics Letters **78** (2001), no. 19, 2828–2830.

[24] J. M. Gerard, *Solid-state cavity-quantum electrodynamics with self-assembled quantum dots*, Single quantum dots (P. Michler, ed.), vol. 90, Springer, Berlin, 2003, p. 269.

[25] J. M. Gerard, B. Sermage, B. Gayral, B. Legrand, E. Costard, and V. Thierry-Mieg, *Enhanced spontaneous emission by quantum boxes in a monolithic optical microcavity*, Physical Review Letters **81** (1998), no. 5, 1110–1113.

[26] J. M. Geremia, J. Williams, and H. Mabuchi, *Inverse-problem approach to designing photonic crystals for cavity qed experiments*, Physical Review E **66** (2002), no. 6, art. no. 066606.

[27] H. M. Gibbs, *Optical bistability: controlling light with light*, Academic Press, Orlando, 1985.

[28] M. Grundmann and D. Bimberg, *Gain and threshold of quantum dot lasers: theory and comparison to experiments*, Japanese Journal of Applied Physics Part 1-Regular Papers Short Notes & Review Papers **30** (1997), no. 6B, 4181–4187.

[29] T. D. Happ, M. Kamp, A. Forchel, J. L. Gentner, and L. Goldstein, *Two-dimensional photonic crystal coupled-defect laser diode*, Applied Physics Letters **82** (2003), no. 1, 4–6.

[30] T. D. Happ, II Tartakovskii, V. D. Kulakovskii, J. P. Reithmaier, M. Kamp, and A. Forchel, *Enhanced light emission of $In_xGa_{1-x}As$ quantum dots in a two-dimensional photonic-crystal defect microcavity*, Physical Review B **66** (2002), no. 4, art. no.–041303.

[31] H. A. Haus, *Electromagnetic noise and quantum optical measurements*, Springer, Berlin, 1999.

[32] D. L. Huffaker, D. G. Deppe, K. Kumar, and T. J. Rogers, *Native-oxide defined ring contact for low-threshold vertical-cavity lasers*, Applied Physics Letters **65** (1994), no. 1, 97–99.

[33] D. L. Huffaker, G. Park, Z. Zou, O. B. Shchekin, and D. G. Deppe, *1.3 μm room-temperature GaAs-based quantum-dot laser*, Applied Physics Letters **73** (1998), no. 18, 2564–2566.

[34] J. K. Hwang, H. Y. Ryu, D. S. Song, I. Y. Han, H. W. Song, H. K. Park, Y. H. Lee, and D. H. Jang, *Room-temperature triangular-lattice two-dimensional photonic band gap lasers operating at 1.54 mum*, Applied Physics Letters **76** (2000), no. 21, 2982–2984.

[35] J. L. Jewell, A. Scherer, S. L. McCall, A. C. Gossard, and J. H. English, *GaAs-AlAs monolithic microresonator arrays*, Applied Physics Letters **51** (1987), no. 2, 94–96.

[36] S. John, *Strong localization of photons in certain disordered dielectric superlattices*, Physical Review Letters **58** (1987), no. 23, 2486–2489.

[37] S. G. Johnson, S. Fan, A. Mekis, and J. D. Joannopoulos, *Multipole-cancellation mechanism for high-Q cavities in the absence of a complete photonic band gap*, Applied Physics Letters **78** (2001), no. 22, 3388–3390.

[38] H. Kawaguchi, *Bistabilities and nonlinearities in laser diodes*, Artech House, Boston, 1994.

[39] G. Khitrova, H. M. Gibbs, F. Jahnke, M. Kira, and S. W. Koch, *Nolinear optics of normal-mode-coupling semiconductor microcavities*, Reviews of Modern Physics **71** (1999), no. 5, 1591–1639.

[40] N. Kirstaedter, N. N. Ledentsov, M. Grundmann, D. Bimberg, V. M. Ustinov, S. S. Ruvimov, M. V. Maximov, P. S. Kopev, Z. I. Alferov, U. Richter, P. Werner, U. Gosele, and J. Heydenreich, *Low-threshold, large T_o injection-laser emission from (InGa)As quantum dots*, Electronics Letters **30** (1994), no. 17, 1416–1417.

[41] T. F. Krauss, R. M. DeLaRue, and S. Brand, *Two-dimensional photonic-bandgap structures operating at near infrared wavelengths*, Nature **383** (1996), no. 6602, 699–702.

[42] R. K. Lee, O. J. Painter, B. Kitzke, A. Scherer, and A. Yariv, *Photonic bandgap disk laser*, Electronics Letters **35** (1999), no. 7, 569–570.

[43] D. Leonard, M. Krishnamurthy, C. M. Reaves, S. P. Denbaars, and P. M. Petroff, *Direct formation of quantum-sized dots from uniform coherent islands of InGaAs on GaAs-surfaces*, Applied Physics Letters **63** (1993), no. 23, 3203–3205.

[44] A. F. J. Levi, R. E. Slusher, S. L. McCall, T. Tanbunek, D. L. Coblentz, and S. J. Pearton, *Room-temperature operation of microdisk lasers with submilliamp threshold current*, Electronics Letters **28** (1992), no. 11, 1010–1012.

[45] M. Loncar, A. Scherer, and Y. M. Qiu, *Photonic crystal laser sources for chemical detection*, Applied Physics Letters **82** (2003), no. 26, 4648–4650.

[46] M. Loncar, T. Yoshie, A. Scherer, P. Gogna, and Y. M. Qiu, *Low-threshold photonic crystal laser*, Applied Physics Letters **81** (2002), no. 15, 2680–2682.

[47] H. Mabuchi and A. C. Doherty, *Cavity quantum electrodynamics: Coherence in context*, Science **298** (2002), no. 5597, 1372–1377.

[48] R. D. Meade, K. D. Brommer, A. M. Rappe, and J. D. Joannopoulos, *Photonic bound-states in periodic dielectric materials*, Physical Review B **44** (1991), no. 24, 13772–13774.

[49] R. D. Meade, A. Devenyi, J. D. Joannopoulos, O. L. Alerhand, D. A. Smith, and K. Kash, *Novel applications of photonic band-gap materials: Low-loss bends and high-Q cavities*, Journal of Applied Physics **75** (1994), no. 9, 4753–4755.

[50] E. Merzbacher, *Quantum mechanics*, third ed., Wiley, 1998.

[51] D. Meschede, H. Walther, and G. Muller, *One-atom maser*, Physical Review Letters **54** (1985), no. 6, 551–554.

[52] C. R. Mirasso, G. H. M. van Tartwijk, E. Hernandez-Garcia, D. Lenstra, S. Lynch, P. Landais, P. Phelan, J. O'Gorman, M. San Miguel, and W. Elsasser, *Self-pulsating semiconductor lasers: Theory and experiment*, IEEE Journal of Quantum Electronics **35** (1999), no. 5, 764–770.

[53] P. A. Morton, T. Tanbunek, R. A. Logan, N. Chand, K. W. Wecht, A. M. Sergent, and P. F. Sciortino, *Packaged 1.55 μm DFB laser with 25 GHz modulation bandwidth*, Electronics Letters **30** (1994), no. 24, 2044–2046.

[54] S. Noda, A. Chutinan, and M. Imada, *Trapping and emission of photons by a single defect in a photonic bandgap structure*, Nature **407** (2000), no. 6804, 608–610.

[55] S. Noda, K. Tomoda, N. Yamamoto, and A. Chutinan, *Full three-dimensional photonic bandgap crystals at near-infrared wavelengths*, Science **289** (2000), no. 5479, 604–606.

[56] M. Ohtsu (ed.), *Near-field nano/atom optics and technology*, Springer, Berlin, 1998.

[57] K. Okamoto, M. Loncar, T. Yoshie, A. Scherer, Y. M. Qiu, and P. Gogna, *Near-field scanning optical microscopy of photonic crystal nanocavities*, Applied Physics Letters **82** (2003), no. 11, 1676–1678.

[58] O. Painter, A. Husain, A. Scherer, P. T. Lee, I. Kim, J. D. O'Brien, and P. D. Dapkus, *Lithographic tuning of a two-dimensional photonic crystal laser array*, IEEE Photonics Technology Letters **12** (2000), no. 9, 1126–1128.

[59] O. Painter, R. K. Lee, A. Scherer, A. Yariv, J. D. O'Brien, P. D. Dapkus, and I. Kim, *Two-dimensional photonic band-gap defect mode laser*, Science **284** (1999), no. 5421, 1819–1821.

[60] O. Painter, K. Srinivasan, J. D. O'Brien, A. Scherer, and P. D. Dapkus, *Tailoring of the resonant mode properties of optical nanocavities in two-dimensional photonic crystal slab waveguides*, Journal of Optics A-Pure and Applied Optics **3** (2001), no. 6, S161–S170.

[61] O. Painter, J. Vuckovic, and A. Scherer, *Defect modes of a two-dimensional photonic crystal in an optically thin dielectric slab*, Journal of the Optical Society of America B-Optical Physics **16** (1999), no. 2, 275–285.

[62] G. Park, O. B. Shchekin, D. L. Huffaker, and D. G. Deppe, *Ingaas quantum dot lasers with submilliamp thresholds and ultra-low threshold current density below room temperature*, Electronics Letters **36** (2000), no. 15, 1283–1284.

[63] H. G. Park, J. K. Hwang, J. Huh, H. Y. Ryu, Y. H. Lee, and J. S. Kim, *Nondegenerate monopole-mode two-dimensional photonic band gap laser*, Applied Physics Letters **79** (2001), no. 19, 3032–3034.

[64] M. Plihal and A. A. Maradudin, *Photonic band structure of two-dimensional systems: The triangular lattice*, Physical Review B **44** (1991), no. 16, 8565.

[65] E. M. Purcell, *Spontaneous emission probabilities at radio frequencies*, Physical Review **69** (1946), no. 11-1, 681–681.

[66] C. Reese, C. Becher, A. Imamoglu, E. Hu, B. D. Gerardot, and P. M. Petroff, *Photonic crystal microcavities with self-assembled InAs quantum dots as active emitters*, Applied Physics Letters **78** (2001), no. 16, 2279–2281.

[67] A. J. Roosmalen, J. A. G. Baggerman, and S. J. H. Brader, *Dry etching for VLSI*, Plenum, New York, 1991.

[68] H. Y. Ryu, S. H. Kim, H. G. Park, J. K. Hwang, Y. H. Lee, and J. S. Kim, *Square-lattice photonic band-gap single-cell laser operating in the lowest-order whispering gallery mode*, Applied Physics Letters **80** (2002), no. 21, 3883–3885.

[69] H. Y. Ryu, Y. H. Lee, R. L. Sellin, and D. Bimberg, *Over 30-fold enhancement of light extraction from free-standing photonic crystal slabs with ingaas quantum dots at low temperature*, Applied Physics Letters **79** (2001), no. 22, 3573–3575.

[70] H. Y. Ryu, M. Notomi, and Y. H. Lee, *High-quality-factor and small-mode-volume hexapole modes in photonic-crystal-slab nanocavities*, Applied Physics Letters **83** (2003), no. 21, 4294–4296.

[71] K. Sakoda, *Symmetry, degeneracy, and uncoupled modes in two-dimensional photonic lattices*, Physical Review B **52** (1995), no. 11, 7982–7986.

[72] ———, *Group-theoretical classification of eigenmodes in three-dimensional photonic lattices*, Physical Review B **55** (1997), no. 23, 15345–15348.

[73] ———, *Optical properties of photonic crystals*, Springer series in optical sciences, Springer, Berlin, 2001.

[74] B. E. A. Saleh and M. C. Teich, *Fundamentals of photonics*, Wiley, New York, 1991.

[75] M. III Sargent, M. O. Scully, and W. E. Jr. Lamb, *Laser physics*, Addison-Wesley, Reading, MA, 1987.

[76] A. Scherer, J. L. Jewell, Y. H. Lee, J. P. Harbison, and L. T. Florez, *Fabrication of microlasers and microresonator optical switches*, Applied Physics Letters **55** (1989), no. 26, 2724–2726.

[77] O. B. Shchekin and D. G. Deppe, *1.3 μm InAs quantum dot laser with T_o=161 K from 0 to 80 degrees C*, Applied Physics Letters **80** (2002), no. 18, 3277–3279.

[78] O. B. Shchekin, G. Park, D. L. Huffaker, and D. G. Deppe, *Discrete energy level separation and the threshold temperature dependence of quantum dot lasers*, Applied Physics Letters **77** (2000), no. 4, 466–468.

[79] B. S. Song, S. Noda, and T. Asano, *Photonic devices based on in-plane hetero photonic crystals*, Science **300** (2003), no. 5625, 1537–1537.

[80] S. M. Spillane, T. J. Kippenberg, and K. J. Vahala, *Ultralow-threshold raman laser using a spherical dielectric microcavity*, Nature **415** (2002), no. 6872, 621–623.

[81] K. Srinivasan, P. E. Barclay, O. Painter, J. X. Chen, A. Y. Cho, and C. Gmachl, *Experimental demonstration of a high quality factor photonic crystal microcavity*, Applied Physics Letters **83** (2003), no. 10, 1915–1917.

[82] K. Srinivasan and O. Painter, *Fourier space design of high-Q cavities in standard and compressed hexagonal lattice photonic crystals*, Optics Express **11** (2003), no. 6, 579–593.

[83] O. Stier, M. Grundmann, and D. Bimberg, *Electronic and optical properties of strained quantum dots modeled by 8-band k·p theory*, Physical Review B **59** (1999), no. 8, 5688–5701.

[84] M. Sugawara (ed.), *Self-assembled InGaAs/GaAs quantum dots*, Academic Press, San Diego, 1999.

[85] A. Taflove and S. C. Hagness, *Computational electrodynamics*, second ed., Artech House, Boston, 2000.

[86] J. Tatebayashi, S. Iwamoto, S. Kako, S. Ishida, and Y. Arakawa, *Optical characteristics of two-dimensional photonic crystal slab nanocavities with self-assembled inas quantum dots for 1.3 μm light emission*, Japanese Journal of Applied Physics Part 1-Regular Papers Short Notes & Review Papers **42** (2003), no. 4B, 2391–2394.

[87] K. Vahala, C. Harder, and A. Yariv, *Observation of relaxation resonance effects in the field spectrum of semiconductor lasers*, Applied Physics Letters **42** (1983), no. 3, 211–213.

[88] K. Vahala and A. Yariv, *Semiclassical theory of noise in semiconductor lasers .1*, IEEE Journal of Quantum Electronics **19** (1983), no. 6, 1096–1101.

[89] ———, *Semiclassical theory of noise in semiconductor lasers .2*, IEEE Journal of Quantum Electronics **19** (1983), no. 6, 1102–1109.

[90] K. J. Vahala, *Optical microcavities*, Nature **424** (2003), no. 6950, 839–846.

[91] J. Vuckovic, M. Loncar, H. Mabuchi, and A. Scherer, *Design of photonic crystal microcavities for cavity QED*, Physical Review E **6501** (2002), no. 1, art. no.–016608.

[92] ———, *Optimization of the Q factor in photonic crystal microcavities*, IEEE Journal of Quantum Electronics **38** (2002), no. 7, 850–856.

[93] J. Vuckovic, O. Painter, Y. Xu, A. Yariv, and A. Scherer, *Finite-difference time-domain calculation of the spontaneous emission coupling factor in optical microcavities*, IEEE Journal of Quantum Electronics **35** (1999), no. 8, 1168–1175.

[94] M. B. Willemsen, A. S. van de Nes, M. P. van Exter, J. P. Woerdman, M. Brunner, and R. Hovel, *Self-pulsations in vertical-cavity semiconductor lasers*, Applied Physics Letters **77** (2000), no. 22, 3514–3516.

[95] J. Witzens, M. Loncar, and A. Scherer, *Self-collimation in planar photonic crystals*, IEEE Journal of Selected Topics in Quantum Electronics **8** (2002), no. 6, 1246–1257.

[96] E. Yablonovitch, *Inhibited spontaneous emission in solid-state physics and electronics*, Physical Review Letters **58** (1987), no. 20, 2059–2062.

[97] M. Yamada, *A theoretical analysis of self-sustained pulsation phenomena in narrow-stripe semiconductor lasers*, IEEE Journal of Quantum Electronics **29** (1993), no. 5, 1330–1336.

[98] Y. Yamamoto (ed.), *Coherence, amplification, and quantum effects in semiconductor lasers*, Wiley, New York, 1991.

[99] Y. Yamamoto, S. Machida, and G. Bjork, *Microcavity semiconductor-laser with enhanced spontaneous emission*, Physical Review A **44** (1991), no. 1, 657–668.

[100] A. Yariv, *Quantum electronics*, 3rd ed., Wiley, 1989.

[101] H. Yokoyama, *Physics and device applications of optical microcavities*, Science **256** (1992), no. 5053, 66–70.

[102] H. Yokoyama and S. D. Brorson, *Rate-equation analysis of microcavity lasers*, Journal of Applied Physics **66** (1989), no. 10, 4801–4805.

[103] T. Yoshie, C. C. Cheng, and A. Scherer, *Two-dimensional photonic crystals for GaN-based blue light emitters*, IEEE 16th International Semiconductor Laser Conference (Nara, Japan), 1998, p. 189.

[104] T. Yoshie, A. Scherer, H. Chen, D. Huffaker, and D. Deppe, *Optical characterization of two-dimensional photonic crystal cavities with indium arsenide quantum dot emitters*, Applied Physics Letters **79** (2001), no. 1, 114–116.

[105] T. Yoshie, O. B. Shchekin, H. Chen, D. G. Deppe, and A. Scherer, *Quantum dot photonic crystal lasers*, Electronics Letters **38** (2002), no. 17, 967–968.

[106] ———, *Planar photonic crystal nanolasers (ii): Low-threshold quantum dot lasers*, IEICE Transactions on Electronics **E87C** (2004), no. 3, 300–307.

[107] T. Yoshie, J. Vuckovic, A. Scherer, H. Chen, and D. Deppe, *High-quality two-dimensional photonic crystal slab cavities*, Applied Physics Letters **79** (2001), no. 26, 4289–4291.

[108] M. E. Zoorob, M. D. B. Charlton, G. J. Parker, J. J. Baumberg, and M. C. Netti, *Complete photonic bandgaps in 12-fold symmetric quasicrystals*, Nature **404** (2000), no. 6779, 740–743.